Synthetic Gauge Field and Spin-Orbit Coupling Studies with Ytterbium Atoms

Universität Hamburg
and
Università degli Studi di Firenze

26. Mai 2017

Marcel Diem

Gutachter: Prof. Dr. Klaus Sengstock
Zweitgutachter: Prof. Dr. Leonardo Fallani

Abstract

This thesis reports, on the one hand, on a novel technique for the implementation of spin-orbit coupling in ultracold atomic gases which exploits a single-photon optical clock transition in ^{173}Yb atoms between the ground state and a long-lived excited state, and on the other hand, on groundwork conducted for the investigation of interaction effects in spin-orbit coupled systems. By treating the internal electronic state of the atoms as a "synthetic" dimension a fermionic ladder system pierced by a tunable uniform synthetic magnetic flux is realized.

In comparison to other methods, the application of a clock transition avoids a possible undesired population of an unstable intermediate state. Furthermore, it features a drastic simplification in the tunability of the magnetic flux in a practical manner. The spin-orbit interactions are detected by the observation of characteristic double-peak spectra, which are connected to Van Hove singularities, and by a direct measurement of chiral edge currents as a function of the magnetic flux. Both detections are enabled by fiber-link-enhanced clock laser stability.

In a second series of measurements, two-photon Raman transitions are used for groundwork studies on the role of interactions varied by the depth of the underlying lattice potential. First indications of interaction effects in spin-orbit coupled systems are presented, insights on chiral current dependencies are provided and experimental limitations are revealed.

The results described in this thesis offer new possibilities for the investigation of topological states of matter with ultracold quantum gases, which could lead to the discovery of topological superconductivity and to applications in quantum information processing.

Zusammenfassung

Diese Masterarbeit berichtet auf der einen Seite von einer neuartigen Technik für das Implementieren von einer Spin-Bahn-Kopplung in ultrakalten atomaren Gasen, die einen optischen Einzelphotonen-Uhren-Übergang in ^{173}Yb Atomen zwischen dem Grundzustand und einem langlebigen angeregten Zustand ausnutzt. Auf der anderen Seite wird von fundamentalen Studien berichtet, die für die Untersuchung von Wechselwirkungseffekten in Systemen mit Spin-Bahn-Kopplung durchgeführt werden. Durch das Behandeln des internen elektronischen Zustands der Atome als eine „synthetische“ Dimension wird ein fermionisches Sprossenleiter-System realisiert, das von einem einstellbaren gleichförmigen magnetischen Fluss durchbohrt wird.

Im Vergleich zu anderen Methoden umgeht die Verwendung eines Uhren-Übergangs eine mögliche ungewollte Population eines instabilen Zwischenzustands. Darüber hinaus zeichnet es sich durch eine drastische Vereinfachung in der Einstellbarkeit des magnetischen Flusses auf eine praktische Art und Weise aus. Die Spin-Bahn-Wechselwirkungen werden durch die Beobachtung von charakteristischen Doppel-Peak-Spektren, die mit Van-Hove-Singularitäten zusammenhängen, und durch eine direkte Messung von chiralen Randströmen als Funktion des magnetischen Flusses, detektiert. Beide Detektionen werden durch eine verstärkte Uhren-Laser-Stabilität aufgrund einer Faser-Verbindung ermöglicht.

In einer zweiten Messungsserie werden Zwei-Photonen-Raman-Übergänge für fundamentale Studien zum Einfluss von Wechselwirkungen genutzt, die durch die Tiefe des zugrunde liegenden optischen Gitters variiert werden. Erste Hinweise auf Wechselwirkungseffekte in Systemen mit Spin-Bahn-Kopplung werden präsentiert, Einblicke in die Abhängigkeiten der chiralen Randströme gewährt und experimentelle Grenzen aufgezeigt.

Die Ergebnisse, die in dieser Arbeit beschrieben werden, bieten neue Möglichkeiten für die Untersuchung von topologischen Materiezuständen mit ultrakalten Quantengasen, die zu der Entdeckung von topologischer Supraleitung und zu Anwendungen in der Quanteninformationsverarbeitung führen könnten.

Riassunto

Questo lavoro di tesi presenta nella prima parte una nuova tecnica che permette la realizzazione di un accoppiamento spin-orbita in gas atomici ultrafreddi sfruttando una transizione ottica di orologio a singolo fotone tra lo stato fondamentale e uno stato eccitato metastabile in atomi di ^{173}Yb. La seconda parte del lavoro descrive invece alcune misure preliminari realizzate per caratterizzare gli effetti delle interazioni in sistemi accoppiati spin-orbita.

Trattando lo stato elettronico interno degli atomi come una dimensione "sintetica", è stato realizzato un sistema fermionico bidimensionale soggetto ad un campo magnetico sintetico con flusso regolabile. In confronto ad altri metodi, l'utilizzazione di una transizione di orologio evita che vengano popolati stati intermedi instabili e permette una drastica semplificazione dal punto di vista sperimentale della regolazione del flusso magnetico. L'interazione spin-orbita viene rilevata dall'osservazione di spettri caratteristici con un doppio picco in connessione delle singolarità di Van Hove e da una misura diretta della corrente chirale di bordo in funzione del flusso magnetico. Entrambe le misure sono rese possibili dalla stabilizzazione in frequenza del laser di orologio su un riferimento ottico ultrastabile disseminato per mezzo di un link in fibra.

In una seconda serie di misure, una transizione Raman a due fotoni è stata utilizzata per caratterizzare gli effetti delle interazioni al variare dell'altezza del potenziale reticolare. Vengono presentati alcuni risultati preliminari sullo studio degli effetti delle interazioni in sistemi accoppiati spin-orbita, viene analizzata la dipendenza delle correnti chirali di bordo in funzione di vari parametri del sistema e presentati i limiti sperimentali della misura.

I risultati descritti in questa tesi offrono nuove possibilità per la ricerca nell'ambito degli stati topologici della materia con gas quantistici ultrafreddi. Tale ricerca potrebbe portare alla scoperta della superconduttività topologica e ad applicazioni nel campo dell'informazione quantistica.

Contents

Introduction

The development of methods to cool and trap atoms with laser light by Steven Chu, Claude Cohen-Tannoudji and William Daniel Phillips (awarded with the Nobel Prize in Physics in 1997) led to the realization of Bose-Einstein condensates (BECs) [3, 32] and degenerate Fermi gases [33]. These achievements gave rise to the field of quantum simulation after the idea of Richard Feynman [37], who envisioned the possibility to engineer real quantum systems in a controllable manner to simulate quantum effects in order to overcome the limitations of analytical calculations and computational power. Cold atomic gases are ideally suited for such quantum simulation, as they allow an extraordinary tunability of the physical parameters characterizing the system, such as: confining potentials, particle density, effective dimensionality [49] and even interactions using Feshbach resonances [26]. To the most outstanding achievements with quantum gases belong the bosonic superfluid to Mott insulator transition [38, 51, 67], the Bardeen-Cooper-Schrieffer (BCS)-BEC crossover with degenerate Fermi gases [9, 16, 52, 73, 146] and even Higgs modes have been discovered [11, 36].

Despite these outstanding achievements, the possibilities for the simulation of solid states with quantum gases seem to be limited as many interesting phenomena occurring in solid state materials are based on electrons moving through electromagnetic fields, whereas atoms in quantum gases are charge neutral. However, laser-atom coupling effects can induce synthetic gauge fields in atomic gases and among them synthetic Abelian gauge fields with U(1) symmetry like the gauge fields of electromagnetism (the well-known vector potential $\vec{A}$ and scalar potential Φ) can be created in a way to generate synthetic magnetic or electric fields for neutral atoms [86–88], i.e. atoms behave like charged particles in electromagnetic fields. Furthermore, the successful implementation of synthetic spin-orbit coupling in one dimension of quantum gases [25, 41, 82, 89, 114, 138, 143, 144] gives hope to even achieve non-Abelian gauge fields [139] with different symmetries like SU(2) or SU(3) as it would be the case for Rashba-type spin-orbit coupling in more than one dimension. Since the weak and strong force possess SU(2) and SU(3) symmetry, respectively, advances in this research direction could further establish quantum gases as emulators for high-energy physics.

Another great and exciting motivation for further studies in these fields is the potential of using synthetic magnetic fields and especially synthetic spin-orbit coupling to form topological states of matter [59, 113]. These materials can feature remarkable characteristics with exceptional

possible applications [99] and their importance for science has been acknowledged with the most recent Nobel Prize in Physics to David J. Thouless, F. Duncan M. Haldane and J. Michael Kosterlitz "for theoretical discoveries of topological phase transitions and topological phases of matter" [1]. One of the most interesting features of topological matter is its robustness against imperfections, such as finite temperature and disorder, which makes it a promising candidate for application fields under unprotected environments and may not be limited to environmental conditions only reachable in laboratories. Moreover, topological matter is expected to be inhabited by non-Abelian anyons, exotic particles, which, if connected in a network, could be used for error-free quantum computing [99] and, thus, could revolutionize modern technology. For this introduction to the research fields Ref. [31, 42, 45, 48, 141, 142] were used for orientation.

In this thesis, important steps are taken towards further advances in the research field of quantum emulators for spin-orbit coupling, gauge theories and topological matter. The first accomplishment described in this thesis is the successful implementation of spin-orbit coupling with a single-photon clock transition, which not only adds another technique for the generation of spin-orbit coupling in ultracold atomic gases but also shows major advantages in comparison to other schemes: avoidance of spontaneous emission from an intermediate state and a reduced complexity in the experimental implementation. The latter point leads to the possibility of tuning the induced magnetic flux in a practical manner, whereas in other approaches this tunability is only theoretically proposed but lacks experimental demonstration and feasibility on reasonable time scales. The significance of the latter improvement is emphasized by the fact that the big advantage of using cold atomic gases for quantum simulation is their outstanding tunability in the underlying physical properties.

The second accomplishment are groundwork studies for the investigation of interaction effects in fermionic spin-orbit coupled systems. The many-body behavior in topological states of matter may enhance and further stabilize their extraordinary characteristic of topologically-protected edge currents. Furthermore, a novel topological superfluid state with Majorana zero modes could be realized [115] and the synthetic dimensions approach used in this thesis could be particularly well suited for fractional quantum Hall emulations [30]. Moreover, a combination of the tunability of the magnetic flux and interactions may lead to the observation of an exotic BCS-BEC crossover since interactions are predicted to allow two-body bound-states on the BCS side for spin-orbit coupled atoms [120, 135, 136]. The studies conducted within the framework of this thesis show first indications of interaction effects, provide insights on chiral current dependencies and reveal experimental limitations.

The content of this thesis is structured as follows:

- In **chapter 1** the basic physical concepts underlying ultracold atomic gases are described and fundamental effects are derived and explained. Within this framework, the specific consequences for and properties of ytterbium atoms are pointed out.
- **Chapter 2** is about the more specific theoretical models of spin-orbit coupling, synthetic gauge fields and topological matter. Main characteristics are mentioned and in particular the implementation in quantum gases is discussed.
- The specifications of the experimental apparatus like the vacuum system and the laser setups are presented in **chapter 3**. Furthermore, the prime experimental procedure for the preparation of degenerate gases as well as main detection and imaging methods are illustrated.
- The experiments conducted in this thesis are described in the chapters 4 and 5. In **chapter** 4 the successful implementation of spin-orbit coupling with an optical clock transition is reported, the tunability of the magnetic flux demonstrated and several evidences for the correct interpretation of the observed physics discussed. In **chapter** 5 two-photon Raman transitions are used for groundwork studies on the role of interactions, insights on chiral currents dependencies are provided and experimental limitations are revealed.
- A final conclusion and outlook will complete this thesis.

Publication

In the context of this thesis the following paper has been published:

Synthetic Dimensions and Spin-Orbit Coupling with an Optical Clock Transition
L. F. Livi, G. Cappellini, M. Diem, L. Franchi, C. Clivati, M. Frittelli, F. Levi, D. Calonico, J. Catani, M. Inguscio, L. Fallani
Phys. Rev. Lett. **117**, 220401 (2016)

1 Fundamental Physics of Ultracold Atomic Gases

In this chapter the basic physical concepts underlying ultracold atomic gases are described and fundamental effects are derived and explained. Within this framework, the specific consequences for and properties of ytterbium atoms are pointed out.

1.1 Laser Cooling and Trapping

This section gives an introduction to the physics of laser cooling and trapping, which is the basis of all experiments with ultracold atomic gases. The description given here has the purpose of demonstrating the most important phenomena in a rather qualitative way. For rigorous derivations and for precise quantitative calculations see suitable literature as books on atomic physics, for example [122].

There are two different forces, which light applies on atoms, the dissipative and non-conservative *radiation pressure* (see section 1.1.1) due to photon scattering processes and the conservative *dipole force* (see section 1.1.2) based on the potential energy of an induced dipole moment in the light's electric field.

1.1.1 Radiation Pressure

When a photon is absorbed by an atom, its momentum of $\hbar\vec{k}_{\mathrm{ph}}$ is transferred to the atom. Therefore, the scattering of photons from a laser beam applies a force an atoms proportional to the scattering rate R_{sc}:

$$\vec{F}_{\mathrm{rad}} = \hbar\vec{k}_{\mathrm{ph}} R_{\mathrm{sc}}. \tag{1.1}$$

An atom also gains a momentum with modulus of $\hbar k_{\mathrm{ph}}$ in a spontaneous emission process, but since this momentum points in a random direction, the total gained momentum averaged over many emission processes is zero. Whereas, the absorbed momenta always point in the same

direction and thus a net force is applied. If the laser frequency is close to a single resonance, the photon scattering rate and correspondingly the radiation pressure become [122]

$$R_{\mathrm{sc}} = \frac{(\Gamma_\omega/2)^3}{\Delta^2 + (\Gamma_\omega/2)^2} \cdot \frac{I}{I_{\mathrm{sat}}}, \quad \vec{F}_{\mathrm{rad}} = \frac{\hbar \vec{k}_{\mathrm{ph}} (\Gamma_\omega/2)^3}{\Delta^2 + (\Gamma_\omega/2)^2} \cdot \frac{I}{I_{\mathrm{sat}}}, \tag{1.2}$$

where Γ_ω is the classical damping rate due to radiative energy loss, Δ is the detuning from the single resonance, I is the laser intensity and I_{sat} is the saturation intensity.

The radiation pressure is a dissipative force and not conservative. It is one of the fundamental forces exploited in quantum gases and used for cooling and trapping mechanisms such as a *Zeeman slower* (see section 3.3.1) or a *magneto-optical trap* (see section 3.3.2).

1.1.2 Dipole Force

The description and explanation of the dipole force given here is done in a classical picture [122]. An external electric field $\vec{E}$ induces a dipole moment $\vec{d}$ in an atom according to

$$\vec{d} = \alpha \vec{E}, \tag{1.3}$$

where α is the complex scalar polarizability[1] of the atom. The potential energy of the induced dipole moment $\vec{d}$ in the electric field $\vec{E}$ is

$$V_{\mathrm{dipole}} = -\frac{\vec{d}\vec{E}}{2} = -\frac{dE}{2}, \tag{1.4}$$

which is half of the potential energy of a steady dipole moment. If the expression $\vec{E} = \vec{E}_0^{(+)} \mathrm{e}^{-i\omega t} + \vec{E}_0^{(-)} \mathrm{e}^{i\omega t}$ is used, where $\vec{E}_0^{(+)}$ is the complex conjugate of $\vec{E}_0^{(-)}$, and fast rotating terms ($\propto \mathrm{e}^{\pm i2\omega t}$) are neglected since they are too fast for responses of the atomic motion, the following expression is obtained:

$$V_{\mathrm{dipole}} = -\frac{1}{2}\left[\alpha(\omega)\vec{E}_0^{(+)}\right] \cdot \vec{E}_0^{(-)} - \frac{1}{2}\left[\alpha(\omega)\vec{E}_0^{(-)}\right] \cdot \vec{E}_0^{(+)} = -\frac{1}{2\varepsilon_0 c}\mathrm{Re}[\alpha(\omega)] I(\vec{r}), \tag{1.5}$$

where ε_0 is the vacuum permittivity, c is the speed of light and $I = 2\varepsilon_0 c |\vec{E}_0^{(+)}|^2$ was used. The corresponding conservative force felt by the atoms is then the negative gradient of the potential

$$\vec{F}_{\mathrm{dipole}} = -\vec{\nabla} V_{\mathrm{dipole}} = -\frac{1}{2\varepsilon_0 c}\mathrm{Re}[\alpha(\omega)] \vec{\nabla} I(\vec{r}). \tag{1.6}$$

[1] The assumption of a scalar polarizability made here is only valid for atoms without "orientation". In general an atom's polarizability can also contain vector or even tensor components, which can lead to additional forces experienced by the atom in an electric field (see Ref. [101])

Using the electron mass m_e, the elementary charge e, the resonance frequency ω_0 and the laser frequency ω an explicit form for the polarizability can be obtained

$$\alpha(\omega) = \frac{e^2}{m_e(\omega_0^2 - \omega^2 - i\Gamma_\omega\omega)} = \frac{e^2(\omega_0^2 - \omega^2 + i\Gamma_\omega\omega)}{(\omega_0^2 - \omega^2)^2 + (\Gamma_\omega\omega)^2}. \tag{1.7}$$

If this expression is inserted into the dipole potential and the detuning $\Delta := \omega - \omega_0$ from a single resonance is defined, the dipole potential can be written as

$$V_{\text{dipole}} = \frac{e^2}{2m_e\varepsilon_0 c} \cdot \frac{(\omega_0 + \omega)\Delta}{[(\omega_0 + \omega)\Delta]^2 + \Gamma_\omega^2\omega^2} I(\vec{r}). \tag{1.8}$$

This form of the dipole potential has the advantage that it shows that its sign only depends on the detuning. For a blue-detuned laser (i.e. $\omega > \omega_0$) the potential is positive, whereas for a red-detuned laser ($\omega < \omega_0$) it is negative. This means that a laser beam with its transverse intensity gradient will repel atoms, if it is blue-detuned, while it will attract atoms, if it is red-detuned.

In order to be able to actually trap atoms in a dipole potential on relevant time scales and not lose them because of the radiation pressure described above (see section 1.1.1), the laser needs to be far-detuned from any resonance. This becomes clear in the dependence of the two forces on the detuning in the case of a far-off single dominant resonance:

$$\vec{F}_{\text{rad}} \propto \frac{I}{\Delta^2}, \quad V_{\text{dipole}} \propto \frac{I}{\Delta}. \tag{1.9}$$

The loss of trapping depth for the dipole force can be compensated by an increased intensity.

Magic Wavelength

Moreover, using $e^2/m_e = 6\pi\varepsilon_0 c^3\Gamma_\omega/\omega^2$ and introducing the on-resonance damping rate $\Gamma \equiv \Gamma_{\omega_0} = (\omega_0/\omega)^2\Gamma_\omega$ the dipole potential (1.5) in the limit of far detuning for a two-level atom can be written as [53]

$$V_{\text{dipole}} = -\frac{3\pi c^2}{2\omega_0^3}\left(\frac{\Gamma}{\omega_0 - \omega} + \frac{\Gamma}{\omega_0 + \omega}\right) I(\vec{r}), \tag{1.10}$$

$$\vec{F}_{\text{rad}} = \frac{3\pi c^2}{2\hbar\omega_0^3}\left(\frac{\omega}{\omega_0}\right)^3 \left(\frac{\Gamma}{\omega_0 - \omega} + \frac{\Gamma}{\omega_0 + \omega}\right)^2 I(\vec{r}), \tag{1.11}$$

which can easily be generalized to a multi-level atom in a state $|n\rangle$:

$$V_{\text{dipole, n}} = -\sum_{m \neq n} \frac{3\pi c^2}{2\omega_{mn}^3}\left(\frac{\Gamma_{mn}}{\omega_{mn} - \omega} + \frac{\Gamma_{mn}}{\omega_{mn} + \omega}\right) I(\vec{r}), \tag{1.12}$$

$$\vec{F}_{\text{rad,n}} = \sum_{m \neq n} \frac{3\pi c^2}{2\hbar\omega_{mn}^3}\left(\frac{\omega}{\omega_{mn}}\right)^3 \left(\frac{\Gamma_{mn}}{\omega_{mn} - \omega} + \frac{\Gamma_{mn}}{\omega_{mn} + \omega}\right)^2 I(\vec{r}), \tag{1.13}$$

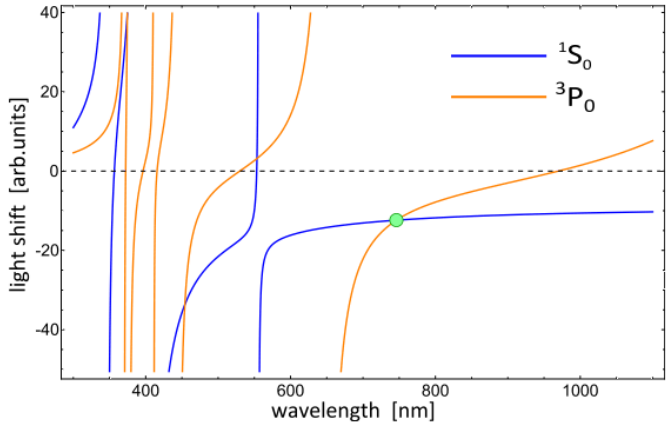

Figure 1.1 – Ytterbium's light shifts. The figure shows the light shifts for ytterbium's $^1S_0$ (blue) and $^3P_0$ state (green) in dependence of the light's wavelength. The green dot denotes the particular magic wavelength used for the optical lattices in this thesis. Figure courtesy of Marco Mancini.

where ω_{mn} is the transition frequency between the states $|m\rangle$ and $|n\rangle$ with the respective damping rate Γ_{mn}. With equation (1.12) the dipole potential for ytterbium's ground state $^1S_0$ and metastable state $^3P_0$ (see section 1.5) is calculated and shown in Figure 1.1. In particular, crossings of the green and blue lines are of interest as at these *magic wavelengths* the dipole potentials for the two states are equal and this fact is of high importance for the measurements conducted in chapter 4. The green dot in Figure 1.1 shows the particular magic wavelength used for the optical lattices (see section 1.1.4) in the experiments conducted in this thesis.

1.1.3 State-Dependent Dipole Potentials

In 1.1.2 the light shifts for the $^1S_0$ and $^3P_0$ states were calculated in the limit of far detuning from any resonances, whereas in this section optical dipole potentials are discussed in the case of detunings comparable or even smaller than the hyperfine splitting. The equations (1.12) and (1.13) are approximations from the full expressions [122]

$$V_{\text{dipole, n}} = -\sum_{m\neq n} \frac{3\pi c^2}{2\omega_{mn}^3} |\mathscr{C}_{nm}(q)|^2 \left(\frac{\alpha_{JJ'}\Gamma_{mn}}{\omega_{mn}-\omega} + \frac{\alpha_{JJ'}\Gamma_{mn}}{\omega_{mn}+\omega} \right) I(\vec{r}), \tag{1.14}$$

$$F_{\text{rad, n}} = \sum_{m\neq n} \frac{3\pi c^2}{2\hbar\omega_{mn}^3} \left(\frac{\omega}{\omega_{mn}} \right)^3 |\mathscr{C}_{nm}(q)|^2 \left(\frac{\alpha_{JJ'}\Gamma_{mn}}{\omega_{mn}-\omega} + \frac{\alpha_{JJ'}\Gamma_{mn}}{\omega_{mn}+\omega} \right)^2 I(\vec{r}), \tag{1.15}$$

containing the multiplicity factor $\alpha_{JJ'} = (2J'+1)/(2J+1)$ and the square of the absolute value of the Clebsch-Gordan coefficients $|\mathscr{C}_{nm}(q)|^2$, which depend on the light polarization state $q = (1,0,-1)$ in the spherical basis.

The Clebsch-Gordan coefficients for a transition between two states, $|n\rangle = |J,F,m_F\rangle \rightarrow |m\rangle = |J',F',m_F+q\rangle$ with well-defined electronic, hyperfine and spin-projection quantum numbers are

$$\mathscr{C}_{nm}(q) = (-1)^{2F'+J+I+m_F}\sqrt{(2J+1)(2F+1)(2F'+1)} \times \begin{Bmatrix} J & J' & 1 \\ F' & F & I \end{Bmatrix} \begin{pmatrix} F' & 1 & F \\ (m_F+q) & q & -m_F \end{pmatrix}, \tag{1.16}$$

where the matrix in curly (round) brackets denotes the 6j(3j)-symbol [122]. The Clebsch-Gordan coefficients make the expressions in (1.14) depend on the considered hyperfine state m_F and the polarization q of the dipole radiation. This is relevant, when Raman transitions are considered in chapter 5 to couple different hyperfine states of the ground state manifold and for the concept of the *optical Stern-Gerlach* (OSG) technique (see section 3.4.1), since in both cases the detuning is on the same order as the hyperfine splitting in the excited state.

1.1.4 Optical Lattices

Optical lattices are a very useful tool to implement a crystalline structure into systems of ultracold atoms and therefore to emulate the periodic potential seen by electrons in solid-state materials. The common way to create an optical lattice in experiments is to superimpose two counter-propagating and phase-locked gaussian laser beams of the same polarization with wavevectors $\pm k_L$, waist w_0 and Rayleigh length z_R. In practice the second counter-propagating beam is usually the retro-reflection of the first beam from a mirror. The stationary interference pattern along the propagation direction z of such two beams generates the following dipole potential

$$V_{\text{lattice}} = V_0 \mathrm{e}^{-\frac{2r^2}{w^2(z)}} \cos^2(k_L z) \approx \frac{sE_r}{2}\left(1+\cos(2k_L z)\right) + \frac{1}{2}m\omega_r^2 r^2 + \frac{1}{2}m\omega_z^2 z^2, \tag{1.17}$$

where m is the atomic mass, $w = w_0\sqrt{1+(z/z_R)^2}$ is the laser's spot size and the potential depth $V_0 = sE_r$ is expressed in units of the recoil energy $E_r = \hbar^2 k_L^2/2m$ and a dimensionless parameter s. The potential is approximated by an expansion around $r = 0$ and $z = 0$ to second order. The first term in equation (1.17) describes a periodic potential along the propagation direction z whereas the other two summands describe two harmonic confinement potentials, which are a direct result of the gaussian form of the laser beams. Their harmonic frequencies are

$$\omega_r = \sqrt{\frac{4E_r}{mw_0^2}}\sqrt{s} \quad \text{and} \quad \omega_z = \sqrt{\frac{2E_r}{mz_R^2}}\sqrt{s}. \tag{1.18}$$

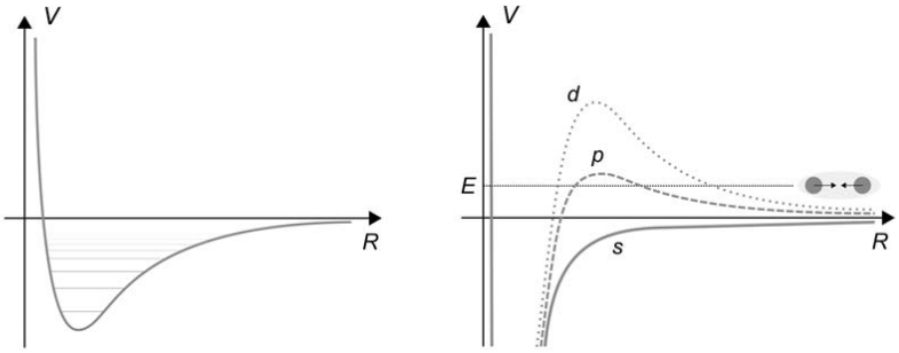

(a) **Typical interaction potential.**

(b) **Two-body collisions.** Typical two-body collisions are shown for partial waves with different angular momentum $l = \{0,1,2\}$ (denoted as s, p, d, respectively). The p- and d-waves feature a centrifugal barrier.

Figure 1.2 – Scattering potentials. The figures show the short-range molecular potentials V as a function of the interatomic distance R. Taken from Ref. [66] with permission of the authors.

However, in the case of collimated beams these confinements can be neglected in first approximation and the equation (1.17) reduces to the periodic term, whose harmonic frequency associated to each lattice site can be obtained by another expansion around $z = 0$ resulting in

$$\omega = \sqrt{\frac{2k_L^2 V_0}{m}} = \frac{2E_r}{\hbar}\sqrt{s}. \tag{1.19}$$

In addition to the possibility of constructing a crystalline structure for quantum gases with three orthogonal pairs of counter-propagating laser beams, optical lattices at sufficiently high potentials can be used to effectively reduce the dimensionality of the system by suppressing any tunneling processes between lattice sites: two-dimensional "pancakes" (using one lattice) [27] over one-dimensional tubes (two orthogonal lattices) [106] to "zero-dimensional" traps (three orthogonal lattices) [21]. Moreover, if the lattice beams intersect at specific angles, exotic patterns such as triangular lattices [127] or graphene-like structures [131] can be created. In this thesis optical lattices are extensively used in order to create one-dimensional tubes for the measurements in chapters 4 and 5 and to tune the ratio of interaction energy over tunneling energy U_{int}/t (see section 5.5.1).

1.2 Interactions in Ultracold Atomic Gases

This section shortly discusses the type of interactions which can be expected in ultracold atomic gases and, therefore, characterizes the interactions which are mentioned throughout chapter 5.

Due to the absence of Coulomb interactions and the possibility to neglect dipole-dipole interactions, the interaction potential in neutral atomic gases is reduced to a hard-core repulsion at zero interatomic distance R and an attractive van-der-Waals potential $\propto -1/R^6$, which becomes dominant at larger distances as illustrated in Figure 1.2(a). Even for a dense Bose-Einstein condensate with $n = 10^{14}\,\mathrm{atoms/cm^3}$, the interparticle distance is $d = n^{-1/3} \approx 0.1\mu\mathrm{m}$, which is much larger than typical ranges of the van-der-Waals potential in the order of a few angstroms. Therefore, interactions can be effectively described as collisions. Furthermore, due to the low density, only two-body collisions are relevant, which cannot form molecules because of the conservation of energy and momentum, and due to the low temperatures the collisions can be treated as purely elastic, which is the case for two atoms in the absolute ground state.

The quantum-mechanical theory of scattering states that for elastic two-body collisions in the center-of-mass coordinate system the wavefunction can be expanded into partial waves distinguished by their angular momentum l. Partial waves with $l \neq 0$ feature a centrifugal barrier in their collisional behavior (see Figure 1.2(b)) because of an additional rotational kinetic energy term $\hbar^2 l(l+1)/2\mu R^2$, where μ is the reduced mass of the two atoms. As a consequence, in the low energy scattering regime only s-wave ($l = 0$) collisions need to be considered and these collisions have the formidable property of being completely describable by a scalar quantity, the *scattering length* a. The absolute value of the scattering length specifies the strength of the interaction by the scattering cross section $\sigma = 4\pi a^2$ and the sign of the scattering length determines whether the interaction is attractive ($a < 0$) or repulsive ($a > 0$). How the interactions in this thesis can be calculated is described in section 1.3.1.

1.3 Physics in Lattices

The description of particles in a periodic potential has been extensively studied in solid state physics in the last century. The solutions of the Schrödinger equation for a homogeneous periodic potential are the well-known *Bloch waves* declared by the *Bloch theorem* [6]. In one dimension the Bloch waves are

$$\psi_{n,k}(z) = \mathrm{e}^{ikz} u_{n,k}(z), \tag{1.20}$$

where $u_{n,k}(z)$ has the same translation invariance as the potential. Bloch waves are characterized by their band index n and their quasimomentum k, which is reduced to the first Brillouin zone:

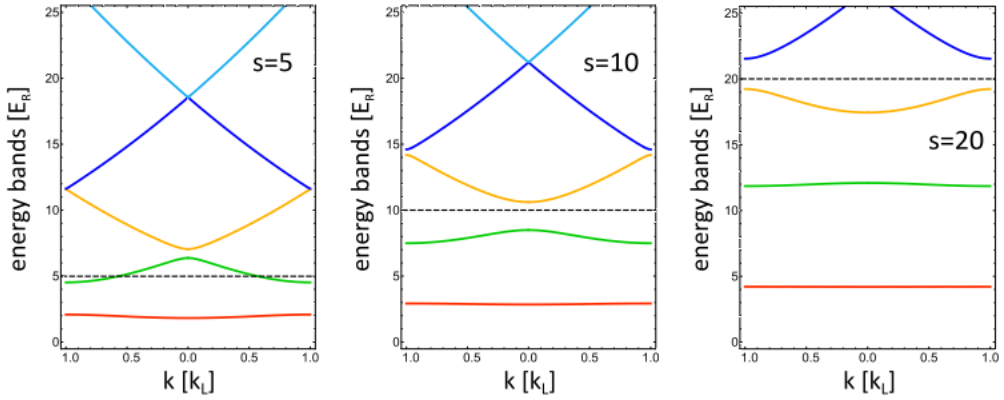

Figure 1.3 – Energy bands. The three plots show the energy bands in units of the recoil energy E_r as a function of the quasimomentum k in units of the lattice momentum k_L for three different lattice depths s. With increasing s the energy bands become flatter and the energy gaps between the bands become larger. Figure courtesy of Marco Mancini.

$-k_L < k < k_L$ (k_L being the lattice momentum). For the specific case of atoms in an optical lattice (see section 1.1.4), the stationary Schrödinger equation has the form

$$\hat{H}\Psi = \left[\frac{p^2}{2m} + \frac{sE_r}{2}\left(1+\cos(2k_L z)\right)\right]\Psi = E\Psi \tag{1.21}$$

which is a second-order differential equation that can be described by the Mathieu equation

$$\left[\frac{\mathrm{d}^2}{\mathrm{d}x^2} + a - 2q\cos(2x)\right]\Psi = 0 \tag{1.22}$$

with the substitutions: $a = E/E_r - s/2$, $q = s/4$ and $x = k_L z$. The solutions to that equation are the Mathieu functions, which form a complete orthogonal set and are modulated according to the lattice potential. Therefore, the Bloch waves can be described by a linear combination of the even $\mathscr{C}$ and odd $\mathscr{S}$ Mathieu functions:

$$\psi_{n,k}(z) = \mathscr{C}\left(E_n(k) - \frac{s}{2}, -\frac{s}{4}, z\right) + i\,\mathrm{sign}(k)\,\mathscr{S}\left(E_n(k) - \frac{s}{2}, -\frac{s}{4}, z\right), \tag{1.23}$$

where z is expressed in units of the lattice spacing $d_L = \lambda_L/2$. Using the Mathieu characteristic values $\mathscr{A}[k, -s/4]$, the energy levels in the system in units of the recoil energy E_r can be calculated by

$$E_n = \mathscr{A}\left[k \pm 2\,\mathrm{sign}(k)\left(\frac{n+1}{2} - 1\right), -\frac{s}{4}\right] + \frac{s}{2}, \tag{1.24}$$

where "+" refers to n being odd and "-" to n being even. The quasimomentum k is expressed in units of the lattice momentum k_L. For three different values of s the energy bands are determined

as a function of the quasimomentum k and are shown in Figure 1.3. With increasing s the energy gaps between the bands become larger and the energy bands become flatter until they are almost completely flat like the energy bands for a harmonic oscillator. This parameter regime of flat energy bands allows spectroscopic measurements to be performed in the *Lamb-Dicke regime* and is of particular importance for the experimental observation of the characteristic double-peak spectra in section 4.2.

1.3.1 Tight-Binding Approximation

When the lattice depth s is increased, the wavefunctions of the atoms are rather localized at the lattice sites. In this case the wavefunctions can be more convieniently expressed in terms of the *Wannier states*, which are the Fourier transformations of the Bloch waves, i.e. for one dimension:

$$\mathfrak{w}_n(z - l d_L) = A \int_{-k_L}^{k_L} \mathrm{e}^{-i(k l d_L + \theta_{n,k})} \psi_{n,k}(z) \mathrm{d}k, \tag{1.25}$$

where A is a constant, $l \in \mathbb{Z}$ and the phase $\theta_{n,k}$ is included since the Bloch functions are only defined up to an overall phase. As a result the Wannier functions are not unique and for simplicity it is common to choose the phase of the Bloch functions in a way that the Wannier functions are maximally localized, i.e. with the smallest possible variance Δz^2 [95]. Wannier functions form a complete set of localized states but are not eigenstates of the Hamiltonian in equation (1.21).

One of the biggest advantages of the Wannier functions is that in the tight-binding approximation, where particles are localized at a single lattice site and hopping processes are only relevant to nearest-neighbor lattice sites, the fermionic operators in second quantization can be expressed in terms of Wannier functions:

$$\hat{\psi}_m^\dagger(\vec{r}) = \sum_j \mathfrak{w}(\vec{r} - \vec{r}_j) \hat{c}_{j,m}^\dagger, \tag{1.26}$$

where m denotes the spin, $\hat{c}_{j,m}^\dagger$ creates a particle with spin m at site $\vec{r}_j$ and the single band approximation was applied, i.e. $\mathfrak{w}_n = \mathfrak{w}_1 =: \mathfrak{w}(\vec{r} - \vec{r}_j)$. In second-quantization the Hamiltonian for a system of interacting particles in a periodic lattice potential is

$$\begin{aligned} \hat{H} = &\sum_m \int \mathrm{d}\vec{r} \hat{\psi}_m^\dagger(\vec{r}) \left[-\frac{\hbar^2}{2m} \vec{\nabla}^2 + V_{\text{lattice}}(\vec{r}) \right] \hat{\psi}_m(\vec{r}) \\ &+ \frac{1}{2} \sum_{m,m'} \int \mathrm{d}\vec{r} \mathrm{d}\vec{r}' \, \hat{\psi}_{m'}^\dagger(\vec{r}') \hat{\psi}_m^\dagger(\vec{r}) U_{\text{int}}(\vec{r}, \vec{r}') \hat{\psi}_m(\vec{r}) \hat{\psi}_{m'}(\vec{r}'), \end{aligned} \tag{1.27}$$

where V_{lattice} and U_{int} are the lattice and interaction potential respectively. If fermions are considered and equation (1.26) is inserted, the Hamiltonian becomes the *Fermi-Hubbard Hamiltonian*

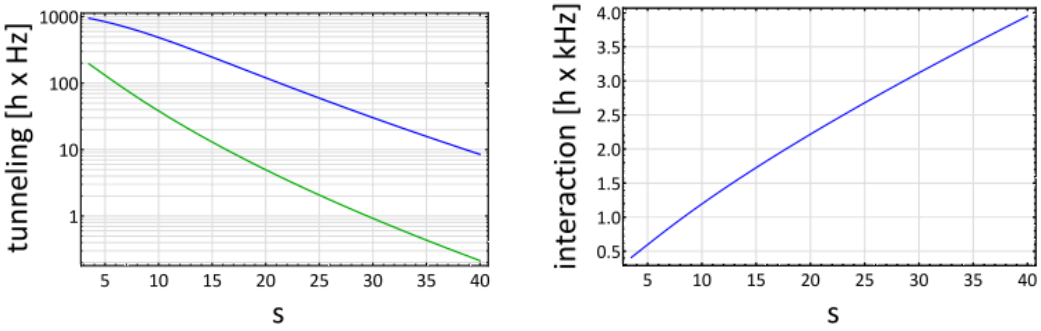

(a) **Tunneling energy.** The plot shows the nearest-neighbor tunneling energy for the lowest energy band (green) and the first excited band (blue) as a function of the lattice depth s according to equation (1.29).

(b) **Interaction energy.** The interaction energy for ^{173}Yb fermions with different spins and a s-wave scattering length of $a = 200\,a_0$ is shown as a function of the lattice depth s according to equation (1.30).

Figure 1.4 – Tunneling and interaction energies. Figure courtesy of Marco Mancini.

[65]

$$\hat{H}_{\text{Fermi-Hubbard}} = -t \sum_{<i,j>,m} (\hat{c}^{\dagger}_{im}\hat{c}_{jm} + \hat{c}^{\dagger}_{jm}\hat{c}_{im}) + U_{\text{int}} \sum_{j,m\neq m'} \hat{n}_{jm}\hat{n}_{jm'}, \tag{1.28}$$

where $< i, j >$ denotes that the sum goes only over nearest-neighbor lattice sites and $\hat{n}_{jm} := \hat{c}^{\dagger}_{jm}\hat{c}_{jm}$ is the number operator. In the tight-binding approximation only nearest-neighbor hopping is considered, i.e. $\vec{r}_j \to \vec{r}_j \pm \vec{u} \cdot d_L$, where $\vec{u}$ is a unit vector, the tunneling energy t is then

$$t = \int \mathrm{d}\vec{r}\, \mathfrak{w}^*(\vec{r}) \left[-\frac{\hbar^2}{2m}\vec{\nabla}^2 + V_{\text{lattice}}(\vec{r}) \right] \mathfrak{w}(\vec{r} + \vec{u} \cdot d_L). \tag{1.29}$$

For the on-site interaction energy U_{int} a two-body contact interaction with the s-wave scattering length a can be assumed for ultracold fermions with different spins (see section 1.2) leading to

$$U_{\text{int}} = \frac{4\pi\hbar^2 a}{m} \int \mathrm{d}\vec{r}\, |\mathfrak{w}(\vec{r})|^4. \tag{1.30}$$

In Figure 1.4 the tunneling energy and the interaction energy for the case of ^{173}Yb fermions with scattering length $a = 200 a_0$ are plotted as a function of the lattice depth s.

1.4 Raman Transitions

In this section the basic concept of Raman transitions in a Λ-configuration (as shown in Figure 1.5) is described. This description is based on [122]. A semi-classical approach is used in

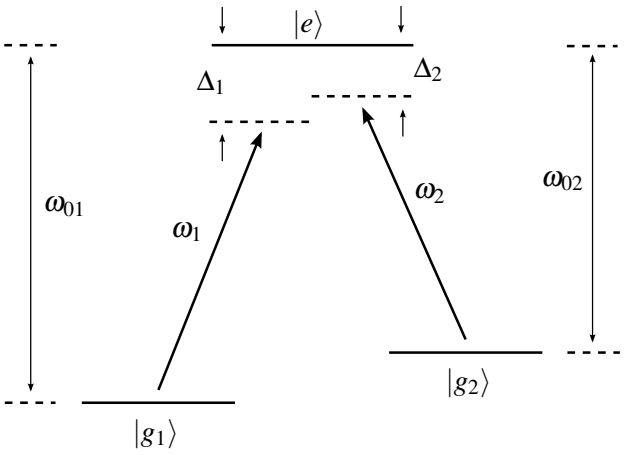

Figure 1.5 – Raman transitions. The figure illustrates the Raman transition scheme in a Λ-configuration.

which the atom's internal states are quantized whereas the light is a treated classically as an electromagnetic wave. The optical field of the two lasers can be described as

$$\vec{E}(\vec{r},t) = \vec{\varepsilon}_1 E_{01} \cos\left(\vec{k_1}\cdot\vec{r} - \omega_1 t\right) + \vec{\varepsilon}_2 E_{02} \cos\left(\vec{k}_2\cdot\vec{r} - \omega_2 t\right). \tag{1.31}$$

If the energy of the excited state is set to be zero, the free atomic Hamiltonian is

$$H_{\text{atom}} = \frac{p^2}{2m} - \hbar\omega_{01}\left|g_1\right\rangle\left\langle g_1\right| - \hbar\omega_{02}\left|g_2\right\rangle\left\langle g_2\right|. \tag{1.32}$$

In the dipole approximation, where the spatial extension of the atom is assumed to be small in comparison to the wavelength of the light, and when the rotating wave approximation is applied, the atom-field interaction Hamiltonian can be written as

$$H_{\text{I}} = \frac{\hbar\Omega_1}{2}\left(\sigma_1 \mathrm{e}^{-i\vec{k}_1\cdot\vec{r}}\mathrm{e}^{i\omega_1 t} + \sigma_1^\dagger \mathrm{e}^{i\vec{k}_1\cdot\vec{r}}\mathrm{e}^{-i\omega_1 t}\right) + \frac{\hbar\Omega_2}{2}\left(\sigma_2 \mathrm{e}^{-i\vec{k}_2\cdot\vec{r}}\mathrm{e}^{i\omega_2 t} + \sigma_2^\dagger \mathrm{e}^{i\vec{k}_2\cdot\vec{r}}\mathrm{e}^{-i\omega_2 t}\right), \tag{1.33}$$

where $\sigma_\alpha \coloneqq \left|g_\alpha\right\rangle\left\langle e\right|$ is an annihilation operator and the Rabi frequencies Ω_α are introduced

$$\Omega_\alpha \coloneqq \frac{-\left\langle g_\alpha\right|\vec{\varepsilon}_\alpha\cdot\vec{d}\left|e\right\rangle E_{0\alpha}}{\hbar}. \tag{1.34}$$

The state vector of the Λ-configuration

$$\left|\psi\right\rangle = c_1\left|g_1\right\rangle + c_2\left|g_2\right\rangle + c_e\left|e\right\rangle \tag{1.35}$$

can be transformed into the rotating frame of the two laser fields:

$$|\tilde{\psi}\rangle = c_1 e^{-i\omega_1 t}|g_1\rangle + c_2 e^{-i\omega_2 t}|g_2\rangle + c_e|e\rangle . \tag{1.36}$$

The two Hamiltonians in this rotating frame are then

$$\tilde{H}_{\text{atom}} = \frac{p^2}{2m} - \hbar\Delta_1 |g_1\rangle\langle g_1| - \hbar\Delta_2 |g_2\rangle\langle g_2| , \tag{1.37}$$

$$\tilde{H}_{\text{I}} = \frac{\hbar\Omega_1}{2}\left(\sigma_1 e^{-i\vec{k}_1\cdot\vec{r}} + \sigma_1^\dagger e^{i\vec{k}_1\cdot\vec{r}}\right) + \frac{\hbar\Omega_2}{2}\left(\sigma_2 e^{-i\vec{k}_2\cdot\vec{r}} + \sigma_2^\dagger e^{i\vec{k}_2\cdot\vec{r}}\right). \tag{1.38}$$

In order to derive the dynamics of the system the Schrödinger equation

$$i\hbar\partial_t |\psi\rangle = (\tilde{H}_{\text{atom}} + \tilde{H}_{\text{I}})|\psi\rangle \tag{1.39}$$

is used, where the spontaneous emission from the excited state is neglected since it is assumed that $\Delta_\alpha \gg \Gamma$, Γ being the decay rate of $|e\rangle$. The state vector can be factorized into external and internal components

$$|\psi\rangle = |\psi_{g_1}\rangle|g_1\rangle + |\psi_{g_2}\rangle|g_2\rangle + |\psi_e\rangle|e\rangle \tag{1.40}$$

and additionally it is assumed that the excited state is effectively never populated: $\partial_t \psi_e(\vec{r},t) = 0$, where $\psi_\alpha(\vec{r},t) := \langle\vec{r}|\psi_\alpha\rangle$. Then, the Schrödinger equation factorizes into the two contributions

$$i\hbar\partial_t \psi_{g_1} = \frac{p^2}{2m}\psi_{g_1} + (\hbar\Delta_1 + \hbar\omega_{ac,1})\psi_{g_1} + \frac{\hbar\Omega_R}{2}e^{i(\vec{k}_2-\vec{k}_1)\cdot\vec{r}}\psi_{g_2}, \tag{1.41}$$

$$i\hbar\partial_t \psi_{g_2} = \frac{p^2}{2m}\psi_{g_2} + (\hbar\Delta_2 + \hbar\omega_{ac,2})\psi_{g_2} + \frac{\hbar\Omega_R}{2}e^{i(\vec{k}_1-\vec{k}_2)\cdot\vec{r}}\psi_{g_1}, \tag{1.42}$$

with the Raman Rabi frequency and the ac Stark shifts

$$\Omega_{\text{R}} := \frac{\Omega_1\Omega_2}{2\Delta}, \qquad \omega_{ac,\alpha} := \frac{\Omega_\alpha^2}{4\Delta}, \tag{1.43}$$

where $\Delta := (\Delta_1 + \Delta_2)/2$ and it is assumed that $|\Delta_2 - \Delta_1| \ll |\Delta|$.

The two equations of motion 1.41 and 1.42 can be generated by applying the following effective Raman Hamiltonian on a general state vector $|\psi\rangle$

$$\begin{aligned} H_{\text{R}} = \frac{p^2}{2m} &+ \hbar(\Delta_1 + \omega_{ac,1})|g_1\rangle\langle g_1| + \hbar(\Delta_2 + \omega_{ac,2})|g_2\rangle\langle g_2| \\ &+ \frac{\hbar\Omega_{\text{R}}}{2}\left(\sigma_{\text{R}} e^{i(\vec{k}_2-\vec{k}_1)\cdot\vec{r}} + \sigma_{\text{R}}^\dagger e^{i(\vec{k}_1-\vec{k}_2)\cdot\vec{r}}\right), \end{aligned} \tag{1.44}$$

where $\sigma_{\text{R}} := |g_1\rangle\langle g_2|$. This means that the initial three level system is effectively reduced to a two level system. It is equivalent to a single-photon transition with momentum $\vec{k}_{\text{s.ph.}} = \vec{k}_1 - \vec{k}_2$ (apart from possible light shifts caused by the Raman beams).

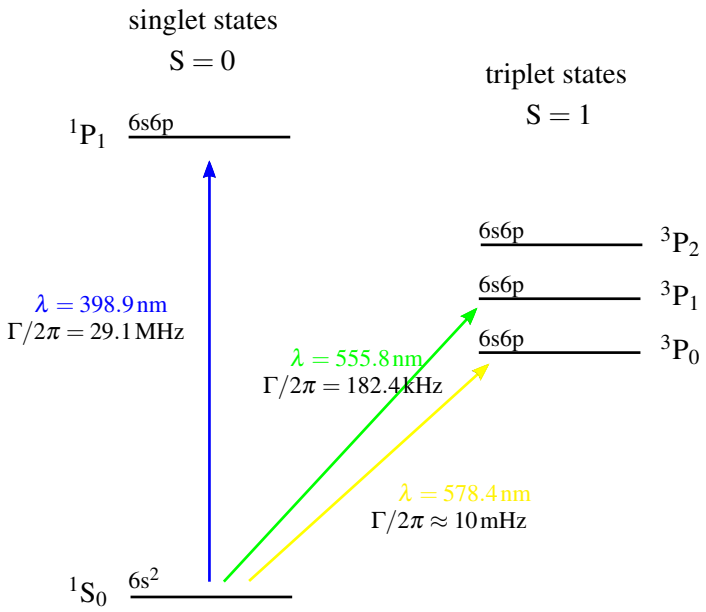

Figure 1.6 – Ytterbium energy level scheme. Ytterbium's fundamental energy levels are shown together with the optical transitions relevant for this thesis.

1.4.1 Multiple Excited States

The approach above can easily be generalized to multiple excited states $|e_n\rangle$ with the respective detunings δ_n. The single Rabi frequencies are then

$$\Omega_{\alpha n} := \frac{-\langle g_\alpha | \vec{\varepsilon}_\alpha \cdot \vec{d} | e_n \rangle E_{0\alpha}}{\hbar} \tag{1.45}$$

leading to the generalized Raman Rabi frequency and Stark shifts

$$\Omega_R = \sum_n \frac{\Omega_{1n}\Omega_{2n}}{2(\Delta - \delta_n)}, \tag{1.46}$$

$$\omega_{ac,\alpha} = \sum_n \frac{\Omega_{\alpha n}^2}{4(\Delta - \delta_n)}. \tag{1.47}$$

1.5 Basic Properties of Ytterbium

Ytterbium is a strongly diamagnetic rare earth metal and possesses seven stable isotopes (see Table 1.1) because of its rather high atomic number $Z = 70$. The averaged atomic mass consid-

Table 1.1 – Ytterbium isotopes. The table lists ytterbium's isotopes with their natural abundance and their nuclear spin.

Isotope	Relative abundance (%)	Nuclear spin	Statistical behavior
^{168}Yb	0.1	0	bosonic
^{170}Yb	3.1	0	bosonic
^{171}Yb	14.3	1/2	fermionic
^{172}Yb	21.9	0	bosonic
^{173}Yb	16.1	5/2	fermionic
^{174}Yb	31.8	0	bosonic
^{176}Yb	12.7	0	bosonic

Table 1.2 – Properties of ytterbium's fundamental transitions [140].

	Blue light	Green light	Yellow light
Wavelength (nm)	399	556	578
Linewidth $\Gamma/2\pi$	29.1 MHz	182.4 kHz	$\approx$ 10 mHz
Life time τ	5.5 ns	850 ns	20 s
Saturation intensity (1/cm^2)	60 mW	140 μW	260 pW
Experimental application	Zeeman slower and imaging	Magneto-optical trap, nuclear spin manipulation and detection and Raman coupling	Spin-orbit coupling

ering the natural abundance of the different isotopes is 173.04 u, its melting and boiling points are 824 °C and 1196 °C and the electronic configuration in its fundamental state is [Xe]4f^{14}6s^2. Ytterbium behaves similar to alkaline earth metals because of the two valence electrons in its 6s orbital. Depending on the combination of the two electronic $1/2$ spins, ytterbium can possess a total spin of either $S = 0$ or $S = 1$ forming either singlet or triplet states, respectively. The resulting energy level scheme together with the fundamental transition lines exploited in the experiments of this thesis are shown in Figure 1.6.

Ytterbium's fundamental transitions are the $^1S_0 \rightarrow {}^1P_1$ transition at 399 nm (blue), the $^1S_0 \rightarrow {}^3P_1$ transition at 556 nm (green) and the $^1S_0 \rightarrow {}^3P_0$ transition at 578 nm (yellow). Their characteristics are summarized in Table 1.2 and a detailed description of all the transitions discussed here can be found in Ref. [140], which was used as the main reference for this section. The blue transition is dipole-allowed and the broadest transition with a linewidth of $\Gamma = 2\pi \times 29.1$ MHz

Table 1.3 – Ytterbium scattering lengths. The table lists all scattering lengths among ytterbium isotopes in units of a_0. Adapted from Ref. [74].

	^{168}Yb	^{170}Yb	^{171}Yb	^{172}Yb	^{173}Yb	^{174}Yb	^{176}Yb
^{168}Yb	**252**	117	89	65	39	2	-359
^{170}Yb		**64**	36	-2	-81	-518	209
^{171}Yb			**-3**	-84	-578	429	142
^{172}Yb				**-600**	418	200	106
^{173}Yb					**200**	139	80
^{174}Yb						**105**	54
^{176}Yb							**-24**

and a corresponding lifetime of 5.5 ns. Blue laser light is used in the experimental setup for the Zeeman slower (see section 3.3.1) and the imaging. The green and the yellow transition are both *intercombination transitions*, which means that they are transitions between singlet and triplet states, i.e. $\Delta S \neq 0$. These transitions are not allowed, if only pure $\vec{L}\cdot\vec{S}$-coupling is considered in the atom, however, strong spin-orbit interactions can occur for elements with high atomic number Z and couple the ^{1}P$_1$ and ^{3}P$_1$ states in ytterbium. Furthermore, hyperfine interactions for the fermionic isotopes cause the ^{3}P$_0$, ^{3}P$_1$ and ^{3}P$_2$ states to mix, thus, enabling even the yellow transition which is not only an intercombination but also a $J = 0 \rightarrow J' = 0$ transition and therefore violates angular momentum conservation. As a consequence of the weak couplings the linewidth of the green transition is much smaller than the blue transition with $\Gamma = 2\pi \times 182.4\,\mathrm{kHz}$ corresponding to a lifetime of 850 ns and the yellow transition is again much smaller than the green transition with $\Gamma \approx 2\pi \times 10\,\mathrm{mHz}$ corresponding to a lifetime of about 20 s which makes the ^{3}P$_0$ state metastable. In the experiment green light is used in the magneto-optical trap (see section 3.3.2), for nuclear spin manipulation and detection (see section 3.4) and for Raman transitions (see chapter 5), whereas yellow light is used for the implementation of single-photon spin-orbit coupling (see chapter 4). Because of its very narrow linewidth and therefore precisely defined frequency the ^{1}S$_0 \rightarrow$ ^{3}P$_0$ transition is exploited in atomic clocks [62, 64] and is called a *clock transition*.

In Table 1.3 the different s-wave scattering lengths among ytterbium's different isotopes are listed, which demonstrate ytterbium's suitability for studies of many-body physics in ultracold mixtures.

2 Spin-Orbit Coupling, Synthetic Gauge Potentials and Topological Matter

This chapter is about the more specific theoretical models of spin-orbit coupling, synthetic gauge fields and topological matter. Main characteristics of these topics are mentioned in general, connections between them are emphasized and in particular the implementation in quantum gases is discussed.

2.1 Spin-Orbit Coupling

Spin-orbit coupling (SOC) is a relativistic quantum mechanical effect and, for example, responsible for the fine structure splitting well-known in atomic physics. In solid-state materials SOC often occurs intrinsically, which is demonstrated by the following example. An electron moves in a two-dimensional plane through a solid-state material, which possesses an electric field $\vec{E} = E_0\vec{e}_z$ normal to that plane due to asymmetries in the confining potential (see Figure 2.1(a) and Figure 2.1(b)). In the comoving momentum frame, where the electron with mass m is at rest, there exists a magnetic field $\vec{B} = (E_0\hbar/mc^2) \times (k_x\vec{e}_y - k_y\vec{e}_x)$, where $\hbar$ is the reduced Planck constant, c is the speed of light in the vacuum and k_x (k_y) is the electron's momentum vector in the x-(y-)direction (see Figure 2.1(c)). The magnetic field leads to a momentum-dependent Zeeman interaction of the form

$$-\mu B \approx \sigma_x k_y - \sigma_y k_x \tag{2.1}$$

which is known as *Rashba SOC* [18]. As a result, the particle's spin $\vec{s}$ (with its magnetic moment $\vec{\mu}_s$) is directly coupled to its momentum $\vec{k}$. The effect of this Zeeman shift on the dispersion relation can be seen in Figure 4.5(a).

2.1.1 Synthetic Spin-Orbit Coupling in Quantum Gases

The intrinsic SOC of solid-state materials is so strong that it would require external electric fields in the order of trillions of volts per meter in order to generate comparable, non-negligible SOCs in laboratories. Since such high electric fields are not available in a laboratory, in order

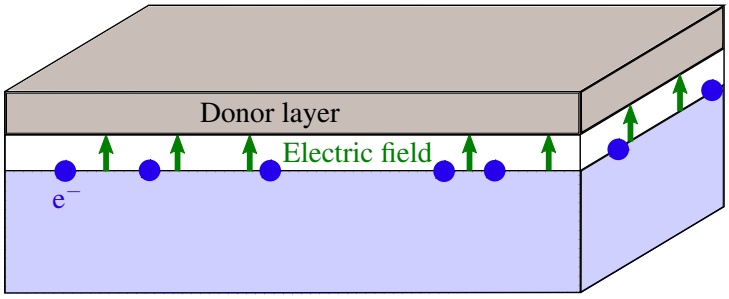

(a) **Solid with broken spatial symmetry.** The donor layer breaks the spatial symmetry in a solid-state material and, thus, induces an electric field along the z direction.

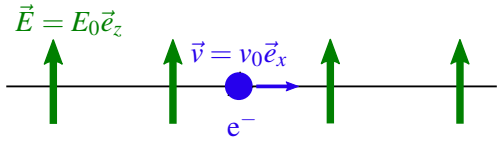

(b) **Laboratory frame.** In the laboratory frame the electron moves through a pure electric field.

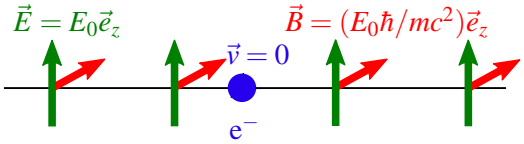

(c) **Comoving frame.** In the comoving momentum frame the electric field converts partially into a magnetic field along y.

Figure 2.1 – **Intrinsic spin-orbit coupling**. The Figures illustrate the occurrence of intrinsic spin-orbit coupling in a solid. Figures adapted from Ref. [42].

to be able to create SOC in a controlled matter, other ways need to be found. A workaround for this problem is to coherently couple different (pseudo)spin states with laser transitions, which transfer momentum to the atoms. On the one hand, in order to achieve a significant SOC, the transferred momentum needs to be large (in the order of $0.1k_L$, where k_L is the lattice momentum) and, on the other hand, the coupling needs to be coherent, i.e. the coupled states must be stable. These two conditions seem contradictory since in a usual photon absorption process the transferred momentum δk correlates with the energy difference between the two coupled states $\Delta E = \delta k \cdot hc/(2\pi)$ and the energy difference is connected to the spontaneous emission rate for dipole radiation as $\Gamma_{\text{sp.em.}} \propto \Delta E^3 \propto \delta k^3$ [122]. Hence, a large momentum transfer usually destroys the coherence between states.

Therefore solutions need to be found to ensure that both requirements of a large momentum transfer and stable coupled states are met. One solution is to use two-photon Raman transitions to couple two different spin states of a ground state manifold. This approach, early proposed in Ref. [61] and then refined in Ref. [90], led to the first observation of SOC in an atomic quantum gas [89]. In such a system the coupled states are stable since they belong to the ground state manifold and the large momentum transfer can be reached by choosing the Raman beams to be in the optical regime. However, as two-photon Raman transitions are applied, in addition, spontaneous emissions from an intermediate state need to be strongly suppressed which can be accomplished to a great extend for sufficiently large detunings from all possible excited states as described in detail in section 1.4. Another solution is to couple two states with a single-photon transition with a large δk, where the excited state has a much longer lifetime than the time scales of the experiment. This can be the case for optical clock transitions and, as described in section 1.5, ytterbium possesses such a clock transition with a lifetime of about 20 s [110]. The implementation of SOC by exploiting ytterbium's clock transition was first proposed in Ref. [43] and realized for the first time in the experiments described in this thesis.

In order to demonstrate that the solutions described above can lead to SOC and to draw a connection to gauge potentials, the following analytical calculation is performed. For a one dimensional system ($\vec{e}_x$) the Hamiltonian of a laser-coupled two-level atom, in which spontaneous emission can be neglected and with a non-negligible momentum transfer $\delta k_x = |\delta\vec{k}| \cdot \cos\theta$, where θ is the angle between the transferred momentum $\delta\vec{k}$ and $\vec{e}_x$, is

$$H = \begin{pmatrix} \frac{k_x^2}{2m} + \frac{\Delta}{2} & \frac{\Omega}{2} e^{i\delta k_x x} \\ \frac{\Omega}{2} e^{-i\delta k_x x} & \frac{k_x^2}{2m} - \frac{\Delta}{2} \end{pmatrix}, \tag{2.2}$$

where Δ is the energy difference between the two coupled states and Ω is the Rabi frequency. It is of particular interest that this Hamiltonian can describe the in section 1.4 discussed two-photon Raman processes ($\delta\vec{k} = \vec{k}_{R1} - \vec{k}_{R2}$, where $\vec{k}_{R1}$ ($\vec{k}_{R2}$) is the momentum vector of the first (second) Raman beam; see also equation (1.44)) or single-photon clock transitions ($\delta\vec{k} = \vec{k}_C$, where $\vec{k}_C$ is

the momentum vector of the clock laser). For a better illustration, that this Hamiltonian actually describes a spin-orbit coupled system, the unitary gauge transformation

$$U = \begin{pmatrix} e^{-i\delta k_x x} & 0 \\ 0 & e^{i\delta k_x x} \end{pmatrix} \tag{2.3}$$

can be applied. The transformed Hamiltonian is then

$$H' = UHU^\dagger = \begin{pmatrix} \frac{(k_x+\delta k_x/2)^2}{2m} + \frac{\Delta}{2} & \frac{\Omega}{2} \\ \frac{\Omega}{2} & \frac{(k_x-\delta k_x/2)^2}{2m} - \frac{\Delta}{2} \end{pmatrix}. \tag{2.4}$$

This Hamiltonian can be expressed using the Pauli matrices:

$$H' = \frac{(k_x + \delta k_x/2 \cdot \sigma_z)^2}{2m} + \frac{\Delta}{2}\sigma_z + \frac{\Omega}{2}\sigma_x \tag{2.5}$$

and after a $\pi/2$ spin rotation around y (transforming the Pauli matrices: $\sigma_x \to \sigma_z$, $\sigma_z \to -\sigma_x$)

$$H' = \frac{(k_x - \delta k_x/2 \cdot \sigma_x)^2}{2m} - \frac{\Delta}{2}\sigma_x + \frac{\Omega}{2}\sigma_z. \tag{2.6}$$

In this form it becomes obvious that this Hamiltonian describes a spin-orbit coupled system with equal contributions of Rashba ($k_x\sigma_x + k_y\sigma_y$) and Dresselhaus ($k_x\sigma_x - k_y\sigma_y$) SOC. Moreover, this Hamiltonian can be compared to a Hamiltonian of a particle with charge q exposed to the gauge fields of electromagnetism, i.e. a vector potential $\vec{A}$ and a scalar potential Φ

$$H_{\text{em}} = \frac{(k_x - q\vec{A})^2}{2m} + \Phi. \tag{2.7}$$

The comparison shows that the Hamiltonian H' in equation (2.6) is equivalent to a Hamiltonian of a spin-1/2 particle with a vector potential $A = \delta k_x/(2q) \cdot \sigma_x$ and a scalar potential $\Phi = \Omega/2 \cdot \sigma_z - \Delta/2 \cdot \sigma_x$. Hence, the production of spin-orbit coupling automatically generates a synthetic vector potential. Theoretically this vector potential has a non-Abelian nature, which means that the single components of the vector potential do not commute with each other, i.e. $[A_i, A_j] \neq 0$ for $i \neq j$.[1] However, since this vector potential only possesses a single non-zero component, it trivially shows Abelian commutation relations[2], but for SOC in more than one dimension non-Abelian physics would appear, as it would be the case for pure Rashba or Dresselhaus SOC [48].

[1] The exact definition of non-Abelian varies slightly in literature. For example in Ref. [48] it is explicitly used for vector potentials, which actually show non-Abelian physical phenomenons.

[2] This statement is based on Ref. [48], whereas in Ref. [141] it is claimed that SOC as described in this section already shows non-Abelian characteristics since the vector potential does not commute with the scalar potential: $[\delta k/(2q) \cdot \sigma_x, \Omega/2\sigma_z - \Delta/2\sigma_x] \neq 0$.

In the next section, gauge potentials and their implementation in ultracold atomic gases are further discussed and in particular it is shown, that the spin-orbit coupled system described here not only features a synthetic gauge field but also a non-zero synthetic magnetic field leading to the realization of the Harper-Hofstadter Hamiltonian.

2.2 Synthetic Gauge Potentials in Lattices

In order to expand the range of systems, which can be emulated with quantum gases, the generation and manipulation of artificial gauge fields in ultracold atomic gases has gained a lot of interest in the last 15 years [13, 31, 48, 84]. Synthetic gauge fields grant the investigation of electromagnetism with neutrally charged particles. In particular, schemes in optical lattices have been shown to offer the study of magnetic fluxes per lattice unit cell in the order of $\phi = \pi$ [43, 68, 98, 102, 116], whereas external magnetic field strengths, which can be routinely reached with current technology, are about 50 T, which corresponds to $\phi \approx 10^{-4}\pi$, if a typical lattice spacing of 10^{-10} m in materials is considered [48]. The quantum Hall effect, which led to the characterization of states of matter in terms of topological phases (see section 2.3), requires large magnetic fields not reachable in quantum gases with external fields (in contrast to condensed matter experiments). Hence, the generation of large synthetic magnetic fluxes leads to the possibility of exploring this extraordinary physical phenomenon. In general, gauge potentials and topological states of matter are strongly connected. In this section the basics for the generation of synthetic gauge potentials in optical lattices with ultracold atoms are described.

2.2.1 Peierls Phase

When the tight-binding approximation is justified, fermions in a lattice can be described by the Fermi-Hubbard Hamiltonian in equation (1.28). In the case of an additional vector potential $\vec{A}$ generating an external magnetic field $\vec{B} = \vec{\nabla} \times \vec{A}$, the Hamiltonian gets modified according to the *Peierls substitution* [107]: the tunneling matrix elements become complex, thus, when particles hop from one lattice site to another they acquire the *Peierls phase* $\phi^i_{j,m} = -qA^i_{j,m}/\hbar$, where $i = \{x, y\}$ and q is the charge of the particle. Hence, if interactions are neglected the Hamiltonian takes the form

$$H = -t \sum_{\mathrm{j,m}} \left(\mathrm{e}^{i\phi^x_{j,m}} c^\dagger_{j+1,m} c_{j,m} + \mathrm{e}^{i\phi^y_{j,m}} c^\dagger_{j,m+1} c_{j,m} + \mathrm{h.c.} \right). \tag{2.8}$$

The Peierls phase in a lattice is equivalent to the *Aharonov-Bohm phase* Φ_{AB} in free space, which is acquired by a particle with charge $q \neq 0$ moving in a vector potential. For a closed trajectory

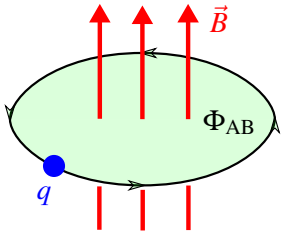

Figure 2.2 – Aharonov-Bohm effect. When a particle with charge $q \neq 0$ moves on a closed trajectory through a vector potential (illustrated by the magnetic field as $\vec{B} = \vec{\nabla} \times \vec{A}$), it acquires the Aharonov-Bohm phase Φ_{AB}.

as illustrated in Figure 2.2, the gained phase is

$$\Phi_{\mathrm{AB}} = -\frac{q}{\hbar} \oint \vec{A} \cdot \mathrm{d}\vec{\mathrm{r}} = \frac{q\Phi_{\mathrm{B}}}{\hbar} \tag{2.9}$$

where Φ_B is the magnetic flux through the area enclosed by the trajectory. Analogously, the magnetic flux per lattice unit cell (also called plaquette) caused by the single Peierls phases can be defined as

$$\phi = \left(\phi^x_{j,m} + \phi^y_{j+1,m} - \phi^x_{j,m+1} - \phi^y_{j,m} \right). \tag{2.10}$$

The theoretical description depends on the gauge, whereas the physical observables, for example the chiral currents in the chapters 4 and 5, do not. Therefore, the Landau gauge, $\phi^x_{\mathrm{j,m}} = -m\phi$, $\phi^y_{\mathrm{j,m}} = 0$, can be chosen, for which the theoretical calculations are particularly easy to compute. This gauge leads to the Harper-Hofstadter Hamiltonian:

$$H_{\text{Harper-Hofstadter}} = -t \sum_{\mathrm{j,m}} \left(\mathrm{e}^{-im\phi}\, c^\dagger_{j+1,m} c_{j,m} + c^\dagger_{j,m+1} c_{j,m} + \mathrm{h.c.} \right). \tag{2.11}$$

The direct connection between a magnetic field and the Peierls phases means that it is sufficient to verify that a system features non-trivial ($\phi \neq \{0, \pi\} \bmod 2\pi$) Peierls phases, in order to prove that a synthetic magnetic field is generated. In the next sections different schemes to engineer such Peierls phases are presented, with special emphasis on the synthetic dimensions approach, which is exploited in this thesis.

2.2.2 Synthetic Dimensions

In this section it will be shown that the synthetic dimensions approach described in Ref. [23] leads to the Harper-Hofstadter model, which features in general non-trivial Peierls phases and, thus, an artificial magnetic field.

Usually, lattice sites are distinguished and characterized by their position in space (optical lattices for example) but this does not need to be the case. In Ref. [14] the atom's internal states, (pseudo-)spin states, are shown to be treatable as lattice sites in a *synthetic dimension*. Therefore, coupling of internal states, for example, by a clock transition or Raman transitions, corresponds to tunneling processes in this additional dimension. Since an absorbed photon imposes its phase on the absorbing atom, tunneling processes in the synthetic dimension are automatically connected to a complex phase factor, whereas tunneling in real dimensions is not complex. For a single spatial dimension an effective two-dimensional system describable by the Harper-Hofstadter Hamiltonian in equation (2.11) is realized and non-trivial Peierls phases and a synthetic magnetic flux are created. An example of such a two-dimensional system, consisting of one spatial and one synthetic dimension pierced by a homogeneous magnetic flux, can be seen in Figure 4.4 for the specific case of this thesis.

The synthetic dimensions approach distinguishes it from other schemes for creating synthetic magnetic fields, firstly, by the sharp boundaries in the synthetic dimension, which make the observation of chiral edge currents particularly simple (see chapters 4 and 5). Secondly, by the unusual feature of strongly localized interactions in the real dimension, on the one hand, and the infinitely long-range interactions in the synthetic dimension on the other hand.

If the lattice sites in the synthetic dimension are considered back as pseudo-spin states and hopping along the synthetic dimension is connected to large momentum transfer, spin-orbit coupling (see section 2.1) is realized.

2.2.3 Other Approaches

Several other approaches for the generation of Peierls phases in two-dimensional lattices exist, which are not used in this thesis but are shortly discussed in this section in order to give an overview of the possibilities of synthetic gauge field generation with ultracold atoms.

The first difference with respect to the synthetic dimensions scheme is, that the natural hopping along one lattice direction must first be inhibited before it is reestablished in a way that non-trivial Peierls phases are generated. This is not needed in the case of the synthetic dimensions approach as the internal atomic states are not naturally coupled.[3] Tunneling processes can be prevented by tilting the lattice [96] or by creating a superlattice with an energy offset between neighboring sites [2]. For a tilted lattice *laser-assisted tunneling* can provide the coupling again as for the synthetic dimension but in this case in a spatial dimension. When a superlattice is used either laser-assisted tunneling or *lattice shaking* [5, 34, 35, 60, 78, 125, 127, 128] can be exploited to overcome the energy barrier and create the necessary Peierls phases. In the lattice

[3] The synthetic dimensions approach requires stable states (at least on the time scales of interest).

shaking techniques the optical lattices are periodically modulated ("shaked") and the application of the Floquet theory [46, 75] leads to an effective time-independent Hamiltonian with complex hopping phases. These methods are the most commonly used mechanisms, however, there are more exotic schemes, which are not further discussed here.

2.2.4 Basic Lattice Models

Beside the Hofstadter model for a uniform magnetic flux, there are other basic lattice models for different flux configurations, which are not realized in this thesis but are shortly mentioned in this section for a clear definition of the boundaries of the work in this thesis and in order to give an overview of the research field.

The *Haldane model* [56] shows a honeycomb lattice geometry with nearest-neighbor (NN) and next-nearest-neighbor (NNN) hopping. While the NN hopping is positive and real, the NNN hopping is complex and shows non-trivial Peierls phases, which lead to local non-zero magnetic fluxes in triangular subplaquettes. Nonetheless, the total flux per honeycomb unit cell is zero [48]. The complex hopping phases break time-reversal (TR) symmetry and open an energy gap in the dispersion relation leading to a non-trivial topological phase that features an anomalous quantum Hall effect (see section 2.3). The development of the Haldane model was an important step for the discovery of the quantum spin Hall effect (see section 2.3.1). Quite recently, the Haldane model was experimentally realized in Ref. [69].

The *Kane-Mele model* can be derived from the Haldane model when the NNN hopping is modified to be opposite for two possible spin configurations, spin-up and spin-down. In this particular case, each spin component sees a local magnetic flux, but since the hopping is inversed the two fluxes are exactly opposed leading to the preservation of TR symmetry [48]. This model was developed in order to investigate the effects of spin-orbit coupling in graphene [70, 71] and it was used to predict the quantum spin Hall effect (see section 2.3.1).

Furthermore, lattice models with non-Abelian gauge potentials exist [10, 44, 47, 94, 102, 117, 134], which can feature anyons with interesting possible applications, in particular for quantum information processing [17].

2.3 Topological States of Matter

The strong connections to the research field of topological states of matter is one of the main motivations for the work conducted in this thesis. Therefore, in this section the concept of topological states of matter is introduced.

One of the greatest achievements in condensed matter physics in the last century was the classification of quantum states in means of spontaneous symmetry breaking [4]. The breaking of the symmetry can be described by the *order parameter*, which is exclusively non-zero in the ordered phase and on which an effective field theory, the *Landau-Ginzburg theory* [80], can be formulated. With the discovery of the *quantum Hall* (QH) state in 1980 [76], which cannot be characterized by spontaneous symmetry breaking, a new kind of classifcation for quantum states arose: *topology*. Topological states of matter are of high interest for basic research in condensed matter physics but also promise exceptional possible applications [99] and their importance was recently acknowledged by the latest Nobel Prize in Physics to David J. Thouless, F. Duncan M. Haldane and J. Michael Kosterlitz "for theoretical discoveries of topological phase transitions and topological phases of matter" [1].

In mathematics, geometrical objects can be classified by their topology: Geometries that can be "smoothly" deformed into one another belong to the same topological class. For example, two dimensional surfaces are distinguished by the number of holes, called genus, in them and a deformation is called smooth, when the genus of the surface is not changed. A famous example of such a topologically invariant deformation is the one of a donut into a coffee cup: Both objects possess the genus 1. Analogously in physics, deformations can be defined to be smooth for systems with a band gap when changes in the Hamiltonian do not close the bulk gap. On the other hand, this means that for the case that the Hamiltonian becomes gapless a quantum phase transition occurs and the topological class is altered. The concepts of order parameters and field theories established for spontaneous symmetry breaking can be adopted for topological phases leading to topological order parameters [132, 133], such as the *Chern number*, and topological field theories (TFTs) [145].

2.3.1 Quantum Hall Effect and Topological Insulators

The integer quantum Hall effect, discovered in 1980 by von Klitzing [76], results in the quantization of the Hall conductance σ in two-dimensional electron systems of a semiconductor at low temperature and high magnetic fields (normal to the system's two-dimensional plane):

$$\sigma = n \cdot \frac{e^2}{h}, \tag{2.12}$$

where e is the elementary charge and n is a positive integer, which can be considered a topological invariant [81, 132]. The quantum Hall state (in its bulk) and the vacuum are both insulating with a gap between valence band and conductance band but do not possess the same topology, thus, following the definition described above, the Hamiltonian of the two gapped phases of different topological classes must be gapless at the boundary between the states. Therefore, at the edge of the quantum Hall state (boundary to the vacuum) there must exist a gapless state,

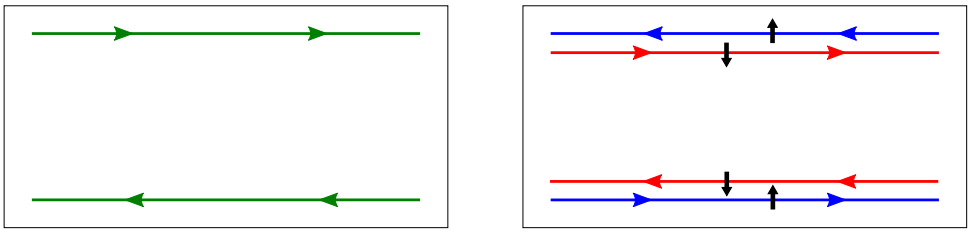

(a) **Quantum Hall state.** Electrons in a quantum Hall state can only move along the edges in a chiral way.

(b) **Quantum spin Hall state.** The quantum spin Hall state can be thought of as two copies of a quantum Hall state, where one copy is only populated by spin-up electrons and the other one only by spin-down electrons. Electrons of different spin states move in the exact opposite direction, thus, the total current is zero.

Figure 2.3 – Chiral edge currents. Figures adapted from Ref. [113].

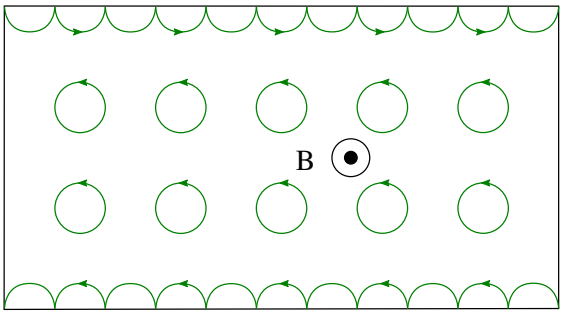

Figure 2.4 – Skipping orbits. Chiral currents of electrons in a quantum Hall state can be described in terms of their skipping cyclotron orbits. Electrons perform cyclotron orbits because of the presence of a magnetic field. However, on the edges the orbits are truncated, i.e. the electrons bounce off the edge and perform skipping orbits. Thus, electrons travel along the edges in a direction determined by the orientation of the magnetic field.

an *edge state*, which carries the Hall conductance. The edge state is protected by the topology of the quantum Hall state and robust against impurities as long as the topology is not changed. On a microscopic level electrons only travel along the edges of the two-dimensional layer in a chiral way meaning that on opposite edges the electrons travel in opposite directions (see Figure 2.3(a)). On a single edge only one propagation direction is allowed demonstrating the robustness against impurities for well-separated edges as no backscattering channels are available. This behavior of the electrons along the edges is also often described in terms of their skipping cyclotron orbits: electrons in a quantum Hall state perform cyclotron orbits because of the magnetic field present, however, on the edges the orbits are truncated, i.e. the electrons bounce off the edge and perform skipping orbits as seen in Figure 2.4, thus, the electrons travel along the edges in a direction determined by the orientation of the magnetic field.

The robustness of the currents makes the quantum Hall state very interesting for applications in electronics. However, it requires high magnetic fields which limits possible applications. As discovered by Haldane [56] the main requirement for the characteristic behavior is not the magnetic field but the broken time-reversal (TR) symmetry associated with the magnetic field. As a consequence, a different type of topological class was theoretically predicted and experimentally observed [59, 79, 97, 112], which does not need a magnetic field. Instead of the broken TR symmetry a *quantum spin Hall* (QSH) state (an example of a two-dimensional *topological insulator*) is based on spin-orbit coupling (see section 2.1). The QSH state can be thought of as two copies of a QH state, where one copy is only populated by spin-up electrons and the other one only by spin-down electrons. The different spins travel in opposite directions leading to a net current equal to zero (see Figure 2.3(b)). *Science Magazine* ranked the first discovery of the QSH topological insulator as one of the top ten breakthroughs among all sciences in 2007 [100].

While the integer QH effect is observed in the regime of non-interacting or only weakly interacting electrons, in the strong interaction regime the *fractional* quantum Hall (FQH) effect takes over. In the FQH effect the Hall conductance is quantized at fractional values of e^2/h instead of at exact multiples. Since the FQH effect is not fully understood theoretically and is expected to feature, for example, non-Abelian anyonic excitations, it is a very promising research topic. The scientific impact of the FQH state was acknowledged in 1998, when Robert B. Laughlin, Horst L. Störmer and Daniel C. Tsui were awarded the Nobel Prize in Physics “for their discovery of a new form of quantum fluid with fractionally charged excitations” [1]. There are several proposals [7, 30, 54, 109, 124, 129] for the possibility to use ultracold atomic gases as quantum emulators for FQH states. The synthetic dimensions approach exploited in this thesis (see section 2.2.2) seems to be particularly well suited because of the featured long range interactions in the synthetic dimension [30]. In chapter 5 groundwork studies are conducted for the experimental investigation of interactions in a spin-orbit coupled system, whose results are also a step towards possible studies of the FQH state.

In this thesis chiral currents, as present in a quantum Hall state, fractional quantum Hall state or in a topological insulator, are observed and analyzed in their behavior in dependence on the synthetic magnetic flux ϕ (see chapter 4) and in dependence on interactions and other system-characterizing quantities (see chapter 5), demonstrating the connection of this thesis to the progresses in the investigation of topological phases.

3 Experimental Setup and Procedures

The specifications of the experimental apparatus are presented in this chapter. The vacuum system and the laser setups are described and the prime experimental procedure for the preparation of degenerate gases as well as main detection and imaging methods are illustrated.

3.1 Vacuum System

The vacuum apparatus is shown in Figure 3.1 and the description given here mostly relies on [22, 93, 105] with some updates. Since Ytterbium has a high melting point (824 °C), it is impossible to obtain a sufficient flow of atoms to the trap with a vapor pressure at room temperature, thus, 7 g of ytterbium chunks (99.9% purity) in natural isotope composition are placed in an oven (**1**), where they are heated up to a mean temperature of 460 °C achieving a vapor pressure of about 10^{-2} Torr and an atom velocity of about 300 m/s. The random atomic motions are channeled by a square array of 100 small tubes (length: 1 cm, inner diameter: 0.2 mm), which are located directly at the oven exit. These small tubes lead to a collimated atomic beam and allow the implementation of a first differential pumping stage using the first ion pump (**3**) of the two Varian Starcell (20 L/s). The front of the oven with the micro-tube array is at a temperature of about 485 °C, whereas the back of the oven only has a temperature of about 435 °C in order to avoid clogging of the micro-tubes. The second ion pump (**3**) performs a second pumping stage between two small tubes (**6**) with lengths of 8 cm and 10 cm and inner diameter of 5 mm right after the first pumping stage. A compressed-air shutter is located in the middle of the second pumping stage. The atoms move further through a VAT-48124 UHV gate valve (**7**), which separates the ultra-high vacuum (UHV) region (10^{-11} Torr), reached by the 55 L/s Varian Starcell (**14**), from the oven region ($10^{-7} - 10^{-10}$ Torr). When the atoms reach the Zeeman slower (**8**), they are slowed down from approximately 300 m/s to a few tens of m/s (see section 3.3.1). The input window (**17**) of the Zeeman slower beam (**18**) on the right side of the setup is made of sapphire and is kept at a temperature of about 250 °C to prevent atom accumulation, which could lower the window's transmission. The velocity reached by the Zeeman slower is low enough in order to capture the atoms in a magneto-optical trap (MOT, see section 3.3.2). A compensation coil (**10**) is implemented in the setup in order to annihilate any residual magnetic field of the Zeeman slower leaking into the MOT chamber (**9**).

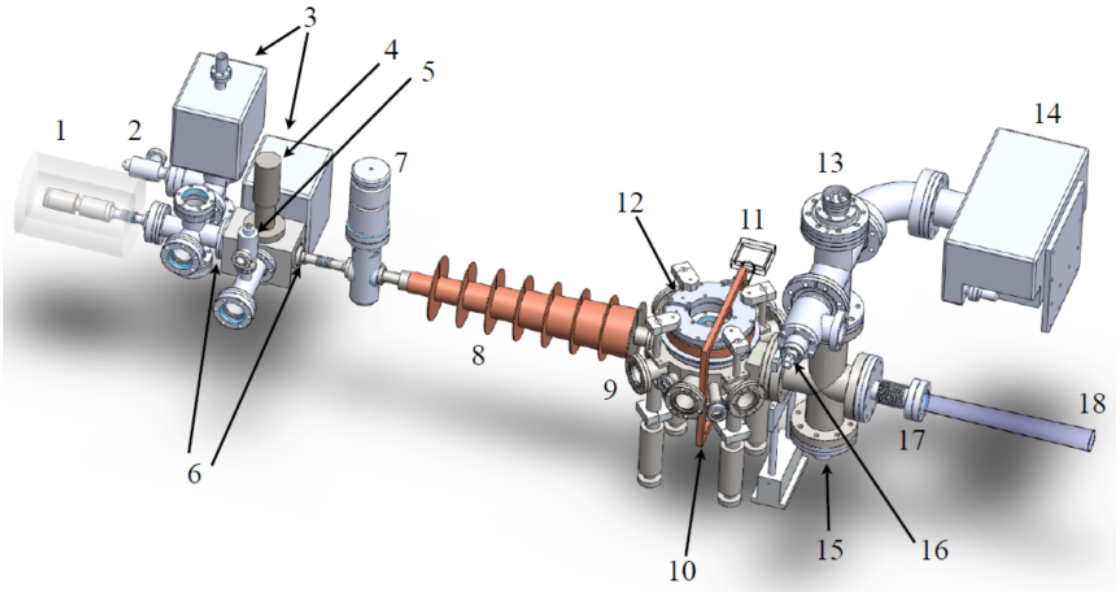

Figure 3.1 – **Vacuum system setup** 1) Oven 2) UHV valve 3) Ion pumps for differential pumping (20 L/s each) 4) Compressed air shutter for atomic beam 5) UHV valve 6) Differential pumping tubes (not shown) 7) VAT UHV gate-valve 8) Zeeman Slower 9) MOT chamber 10) Compensation coil 11) Glass cell 12) MOT coils 13) Titanium sublimation pump 14) Ion pump for MOT chamber (55 L/s) 15) UHV Gauge, mod. Bayard-Alpert, Varian UHV-24p 16) UHV Valve 17) Sapphire window with bellow 18) Slowing beam at 399 nm. Taken from Ref. [105].

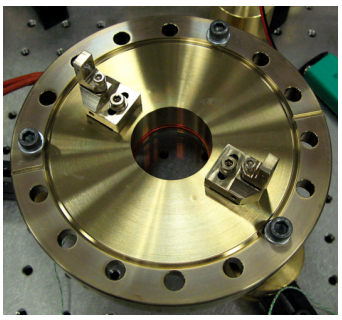

Figure 3.2 – In-vacuum optical cavity mounted on a CF100 flange. Taken from Ref. [105].

An AISI L316 stainless steel octagonal chamber (**9**) is used for a MOT stage employing two water-cooled anti-Helmholtz coils (**12**) [105]. The chamber has seven CF40 flanges in the horizontal plane: one flange is used to attach the MOT chamber to the Zeeman slower, the four flanges at 45 degrees with respect to the atomic beam axis are used for the horizontal MOT beams and the two flanges orthogonal to the atomic beam axis are used for an input window for the optical transport beam and for a connection to a high-optical-access glass cell (**11**, see subsection 3.1.2). In addition, there is a larger CF63 flange directly on the atomic beam axis used for a cross connection to the 55 L/s Varian Starcell ion pump (**14**). In the vertical plane the MOT chamber features two CF100 flanges, each holding a CF40 window, where on the upper flange, in addition to the window, two metallic supports are mounted for an in-vacuum optical cavity (see subsection 3.1.1 and Figure 3.2). A titanium sublimation pump (**13**) is included in the setup for further vacuum improvement and the pressure at this end of the vacuum system is measured by a Bayard-Alpert ion gauge UHV-24P (**15**).

3.1.1 In-Vacuum Optical Cavity

On the upper CF100 flange of the MOT chamber a Fabry-Perot cavity is mounted (see Figure 3.2) in order to trap and pre-cool the atoms before they are transported to the science glass cell (see subsection 3.1.2 and Figure 3.3). The cavity's metallic supports seen in Figure 3.2 hold two spherical mirrors with a radius of curvature of 2 m, a diameter of 6.35 mm and a thickness of 2.3 mm. The theoretical finesse of the cavity is about $\mathscr{F} \approx 1600$ given by the mirror's reflectivity of 99.98 %, whereas a finesse measurement resulted in a value of $\mathscr{F} \approx 1850$, which corresponds to a power enhancement factor of $4\mathscr{F}/\pi \approx 2350$ (losses neglected). The cavity has a fixed length of 9 cm, which leads to a free spectral range of FSR $= 1.67$ GHz. Assuming an incident power of 1.8 W and considering the chosen waist $w_0 = 300\,\mu$m, the cavity's parameters lead to a trap depth of $V_0/k_B \approx 800\,\mu\text{K} \approx 8T_{\text{MOT}}$, where T_{MOT} is the temperature reached in the magneto-optical trap (see section 3.3.2).

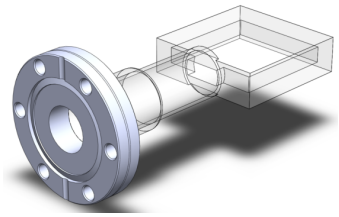

Figure 3.3 – Science glass cell. Number **11** in Figure 3.1. Taken from Ref. [105].

3.1.2 Science Glass Cell

The atoms are transported (see section 3.3.4) to a high-optical-access glass cell (see Figure 3.3 and for its position in the vacuum system see number **11** in Figure 3.1) manufactured by Hellma Analytics, where the main part of any experiments is conducted. This concept of transporting ultracold atoms to a separated science cell after the MOT phase becomes more and more common [55, 119]. The advantages of a science glass cell are, firstly, the high optical access and, secondly, the avoidance of influences from residual magnetization of the vacuum apparatus' metallic components. The glass cell's outer dimensions are $(60 \times 60 \times 18)$ mm and since each face is 5 mm thick, the inner dimensions are $(50 \times 50 \times 8)$ mm. The glass cell is designed for a possible implementation of a high-numerical-aperture objective with a small working distance [24, 57, 108, 121] in the future. Hence, in the vertical direction the distance from the center of the glass cell to its outer surface is only 9 mm.

3.2 Laser Setups

3.2.1 399 nm and 556 nm Laser Systems

In the experimental system of this thesis the blue laser radiation at 399 nm addresses the $^1S_0 \rightarrow {}^1P_1$ transition (see Figure 1.6) and serves two purposes, firstly, slowing down the atomic beam in the Zeeman slower and, secondly, performing absorption imaging. The laser setup can be seen in Figure 3.4. 1.1 W of 798 nm radiation reached by a fiber-coupled tapered amplifier laser-diode system, TOPTICA TA PRO, is used to inject a 15 mm long Lithium-Triborate (LBO) non-linear crystal, which is optimized for type-I phase matching and stabilized at a temperature of 55 °C. The second-harmonic generation inside the LBO is enhanced by a bow-tie cavity using two plane mirrors, M1 and M2, and two curved mirrors, M3 and M4, with radii of curvature 60 mm and 100 mm, respectively. The cavity's free spectral range is FSR = 749 MHz, its finesse is $\mathscr{F} = 100$ and its length is stabilized by the Hänsch-Couillaud locking technique [58], which acts

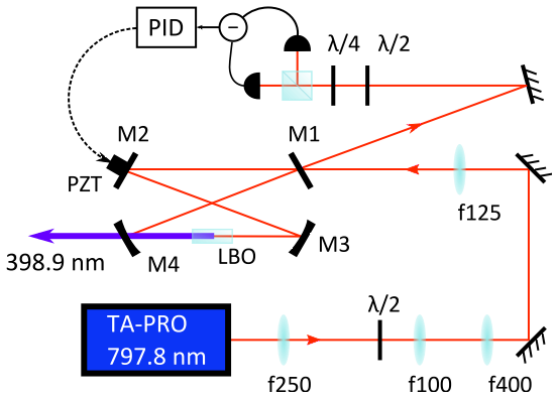

Figure 3.4 – Laser setup for 399 nm. See text for details. Figure courtesy of Marco Mancini.

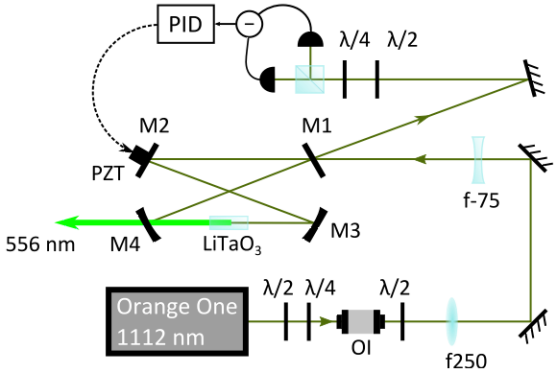

Figure 3.5 – Laser setup for 556 nm. See text for details. Figure courtesy of Marco Mancini.

on a piezoelectric stack (PZT) mounted on the cavity mirror M2. With a conversion efficiency of about 50 % a stable output power of 550 mW of 399 nm laser light is reached.

Green 556 nm laser light, which addresses the $^1S_0 \rightarrow {}^3P_1$ transition (see Figure 1.6), has several applications in the system described in this thesis: magneto-optical trapping (see section 3.3.2), optical spin state pumping (see sections 3.4.2 and 3.4.3), optical Stern-Gerlach (see section 3.4.1) and Raman coupling (see section 5.1). The setup for the production of this laser light is very similar to the scheme for the 399 nm laser and can be seen in Figure 3.5. A fiber laser at 1112 nm, Menlo Systems model ORANGE ONE, is frequency doubled in a bow-tie cavity with a 10 mm long Lithium Tantalate (LiTaO3) crystal, which possesses an anti-reflective coating for 1112 nm light. In order to ensure quasi phase-matching, the crystal is periodically poled with a period of 9.12 μm. The cavity's free spectral range is FSR = 567 MHz, its finesse is $\mathscr{F} = 67$ and it is also stabilized with the Hänsch-Couillaud locking technique [58]. The conversion efficiency of about 50 % leads to an output power of 1.05 W of 556 nm radiation.

For the purpose of a higher lock stability, the thermal and acoustic isolation is improved by sealing the two bow-tie cavities for the second-harmonic generation inside aluminum boxes under vacuum. Moreover, the two lasers are directly locked on the atomic transitions, $^1S_0 \rightarrow {}^1P_1$ for the 399 nm and $^1S_0 \rightarrow {}^3P_1$ for the 556 nm, by performing standard fluorescence spectroscopy on an atomic Ytterbium beam, which is provided by a second oven (average temperature of 425 °C) and, thus, independent from the Ytterbium source used for experiments. The spectroscopy produces an electronic feedback signal, which is sent to the lasers and causes frequency corrections. The spectroscopy interrogation is performed with the laser beams transverse to the propagation direction of the atomic beam. The $^1S_0 \rightarrow {}^1P_1$ transition has a linewidth of $\Gamma_{399} = 2\pi \times 29$ MHz, which is broader than the transverse Doppler profile of the collimated[1] atomic beam. Therefore, the transverse spectroscopy signal is sufficient for a stable lock of the 399 nm laser, whereas the $^1S_0 \rightarrow {}^3P_1$ intercombination transition only has a linewidth of $\Gamma_{556} = 2\pi \times 182$ kHz and needs a Doppler-free saturation spectroscopy. A detailed description of the two spectroscopy setups and locking procedures can be found in Ref. [92, 104], however, with respect to the references a few changes have been made on the locking scheme of the fermionic isotope ^{173}Yb, which are considered below.

A scheme for the locking procedure of the green 556 nm light is shown in Figure 3.6. With the experimental setup described here, only the fermionic isotope ^{173}Yb and the bosonic isotope ^{174}Yb are used. The Doppler-free spectroscopy performed with π-polarized light on the $^1S_0 \rightarrow {}^3P_1$ transition differs for those two isotopes significantly, since ^{173}Yb has a nuclear spin $I_{173} = 5/2$ (see Table 1.1), which leads to six magnetic-field-sensitive π-transitions ($F = 5/2 \rightarrow F' = 7/2$), whereas ^{174}Yb has a nuclear spin $I_{174} = 0$ (see Table 1.1), which leads to a single

[1] The atomic beam is collimated in the second oven by the same kind of micro-tubes described in section 3.1.

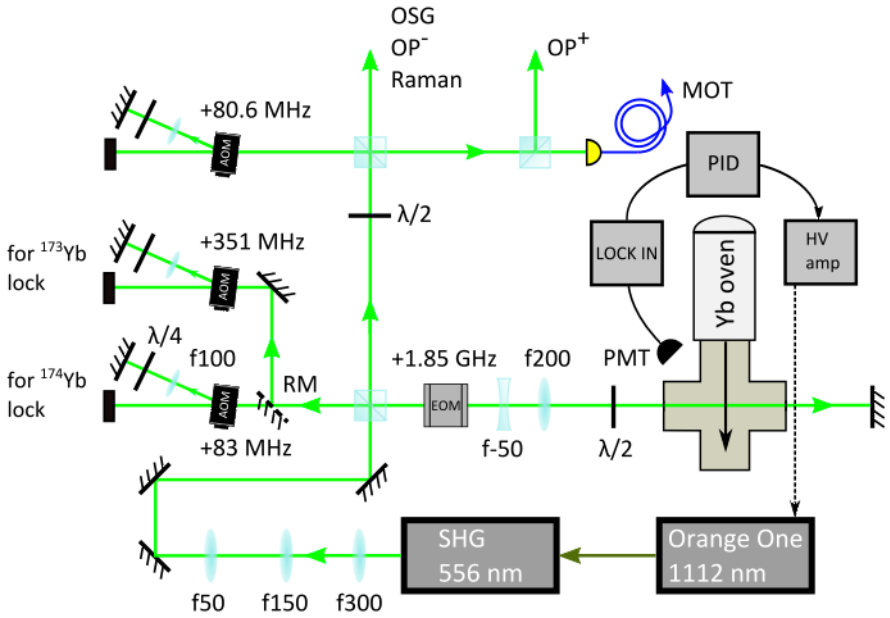

Figure 3.6 – Fluorescence spectroscopy locking scheme for 556 nm. See text for details. Figure courtesy of Marco Mancini.

magnetic field insensitive π-transition ($J = 0, m_J = 0 \rightarrow J' = 1, m'_J = 0$). Furthermore, the natural abundance of ^{174}Yb is approximately twice as large as of ^{173}Yb (see Table 1.1). Therefore, the spectroscopy signal on ^{174}Yb has a much larger signal-to-noise ratio and is better suited for a laser frequency lock, hence, this isotope is always used for the frequency locking regardless of which isotope is used in the experiment. This is realized by the following setup (see Figure 3.6). When the experiment runs with ^{174}Yb the laser branch for the spectroscopy signal first propagates through an acousto-optic modulator (AOM) in double passage increasing the frequency by 166 MHz, thus, the laser itself, when locked, is red-detuned by -166 MHz. When the experiment runs with ^{173}Yb the laser branch for the spectroscopy signal propagates through a different AOM in double passage increasing the frequency by 702 MHz and, in addition, through an electro-optic modulator (EOM) increasing the frequency by another 1.85 GHz, thus, the laser is red-detuned by a total of -2552 MHz. Since the two isotope transitions described above have a frequency difference of $\Delta_{174-173} = 2386$ MHz, the laser is effectively red-detuned with respect to the ^{173}Yb transition by -166 MHz, which is the same detuning as in the case of experimental operation with ^{174}Yb. It is possible to change between the two locking schemes simply by removing or inserting a removable mirror on a magnetic mount (RM in Figure 3.6) and by switching the EOM on or off.

3.2.2 1064 nm Laser System

Laser radiation at 1064 nm is used for three different purposes. It is used for the injection of the in-vacuum Fabry-Perot cavity (see sections 3.1.1 and 3.3.3), for the dipole trap transporting the atoms from the MOT chamber to the science glass cell (see section 3.3.4) and for the crossed dipole trap (see section 3.3.4). The laser source is a Nd:YAG Mephisto MOPA from Coherent with an output power of 42 W and a linewidth below 100 kHz. A scheme of the laser setup can be seen in Figure 3.7(a).

The laser's frequency is stabilized by a frequency lock for the in-vacuum optical cavity (see section 3.1.1) with a standard Pound-Drever-Hall (PDH) locking technique [12] using an EOM at 39 MHz for the frequency modulation. The locking scheme can be seen in Figure 3.7(b). An active filter splits the error signal into high-frequency components, which are sent to a PID that acts on a piezoelectric actuator connected to the Mephisto's seed laser for fast corrections (100 kHz bandwidth), and low-frequency components (<3 Hz), which are sent to a PID that acts on the temperature of the seed laser for slow corrections (1 Hz bandwidth) and a wide range (3 GHz / °C). Furthermore, the power on the photodiode of the PDH signal is actively stabilized using an additional AOM for a stable error signal, which is needed since the power on the in-vacuum cavity is strongly tuned during the experimental cycle. More specifically, the error signal's AC part is used for the PDH frequency lock and the DC part is sent to the AOM in front of the photodiode for the power stabilization. The optical fibers could be damaged by small beam misalignments because of the very high powers involved in this setup. Therefore, all the AOMs used before the coupling into the fibers are operated in a double-frequency mode [40] in order to keep their temperatures stable and avoid thermally-induced misalignments.

3.2.3 759 nm Laser System

In this experimental apparatus the laser radiation at 759 nm has the single purpose of forming the optical lattices in the way described in 1.1.4 (see section 3.3.5 for the implementation in the experimental system). The wavelength of 759 nm was chosen as it is the "magic" wavelength, for which the induced light shifts on the $^1S_0$ and the $^3P_0$ state are exactly equal (see section 1.1.2 and Figure 1.1). The Coherent MBR 110 is a Titanium-Sapphire laser, which emits the desired laser radiation, after it is pumped by a Coherent VERDI 18 at 532 nm. The approximately 3.5 W of 759 nm laser light is split into three different branches in order to produce optical lattices along three different directions, where each branch includes an AOM (for power control) and a fiber. Moreover, the single-mode emission of the MBR is monitored by injecting a small portion of the 759 nm light into a confocal Fabry-Perot cavity.

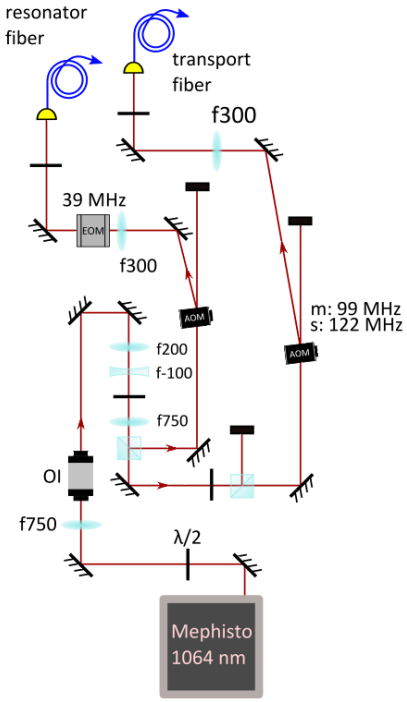

(a) **Main setup**

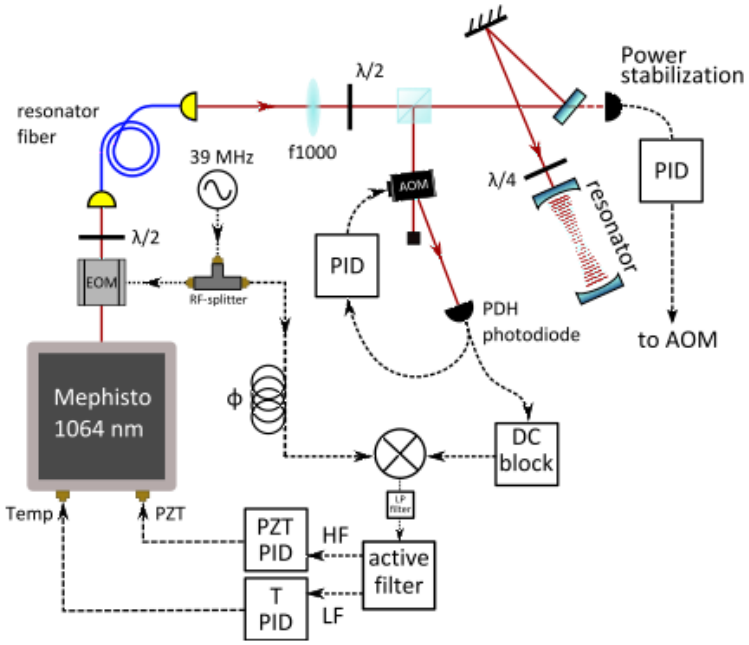

(b) **Pound-Drever-Hall locking setup.**

Figure 3.7 – Laser setup for 1064 nm radiation. See text for details. Figure courtesy of Marco Mancini.

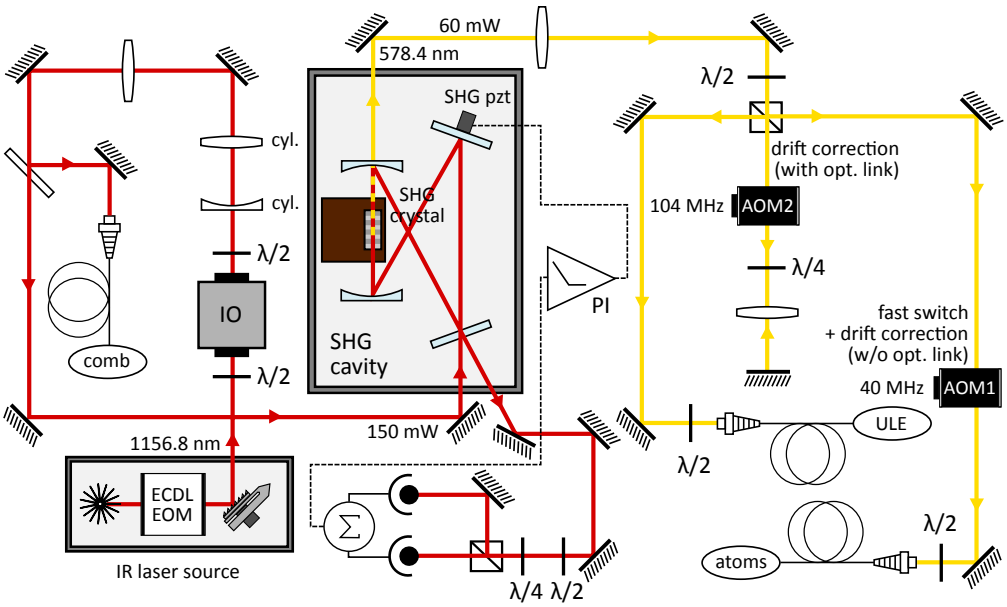

Figure 3.8 – Clock laser setup. See text for details. Figure courtesy of Giacomo Cappellini.

3.2.4 578 nm Laser System: the Clock Laser

Laser radiation at 578 nm is needed to address the $^1S_0 \rightarrow {}^3P_0$ clock transition (see Figure 1.6) for one of the main subjects of this thesis, which is the realization of spin-orbit coupling with an optical clock transition (see chapter 4). For a detailed description of this laser source with its particular challenges see Ref. [22]. In order to address the clock transition with an ultra-narrow linewidth $\Gamma \approx 2\pi \times 10\,\text{mHz}$ the laser source needs to be very stable. A scheme of the laser setup can be seen in Figure 3.8. The first stages of the setup are similar to the ones for the 399 nm and 556 nm lasers (see section 3.2.1). Infrared light at 1156 nm is emitted by a quantum dot laser, which is placed in a 15 cm long external-cavity. For the purpose of high-bandwidth frequency stabilization an intra-cavity EOM is included in the cavity. After SHG in a bow-tie cavity about 50 mW of 578 nm laser light are reached. The cavity length is stabilized by a Hänsch-Couillaud locking technique [58] acting on a piezoelectric actuator mounted on one of the cavity mirrors.

Ultra-low-expansion glass cavity

An ultra-low-expansion glass (ULE) cavity is used as a frequency reference for the infrared 1156 nm laser. The ULE cavity is injected by a small portion of the 578 nm light, which is power stabilized on 60 μW by an AOM in front of it. Because of the precision needed for a frequency reference used for addressing an ultra-narrow clock transition (10^{-14} for a power-broadened

linewidth of a few Hz), the ULE cavity is isolated from noise sources as much as possible. The power stabilization minimizes power-induced fluctuations on the cavity resonance, for example by radiation pressure or coating absorption (photo-thermal effect) [108]. It is surrounded by a thermally-stabilized copper shield and placed in a vacuum chamber (10^{-7} mbar). The ULE cavity, together with an EOM used for the generation of the PDH error signal, are mounted on an anti-vibrating platform for the reduction of seismic noise and placed in a box isolating the system from the lab environment. The PDH signal from the ULE cavity is sent to the intra-cavity EOM (for corrections in the high frequency domain) and to a piezoelectric stack mounted on the grating (for corrections in the low frequency domain) of the infrared laser.

Optical fiber link

The frequency stabilization described so far for the laser source still features a random residual drift of the order of 0.1 Hz/s, which prevents the work with the clock transition on time scales longer than about 20-30 minutes without recalibration. Since typical measurements performed in this thesis take about several hours and already small detunings from resonance have a major impact on the measured data, as for example the loading of the dressed state (see section 4.4.1) is very sensitive to it, a long term reference is needed. For this purpose a connection from the Italian Metrological Institute (INRIM) in Turin to the European Laboratory for Non-linear Spectroscopy (LENS) in Florence via a 642 km long optical fiber link is exploited [28, 83]. A 1542 nm laser, which is stabilized at INRIM onto the primary Cs-fountain atomic clock and injected into the fiber, reaches the LENS laboratory and is used as a reference for a frequency comb. Then the laser source described here is locked on the comb and thus reaches a long-term stability that makes measurements for several hours possible [29].

3.3 Experimental Procedure

In this section the experimental procedure for the preparation of a degenerate ^{173}Yb gas is presented.

3.3.1 Zeeman Slower

As soon as the ytterbium atoms leave the oven they are slowed down by a Zeeman slower which uses the broadest fundamental transition, the $^1S_0 \rightarrow {}^1P_1$ at 399nm. The radiation pressure (see section 1.1.1) induced on the atoms by the Zeeman slower slows the atoms down from about 340 m/s to a few 10 m/s in a distance of 50 cm before the atoms enter the vacuum chamber of the magneto-optical trap (MOT). For this purpose the laser is aligned to propagate in the

opposite direction than the atoms, it is σ^- polarized and red-detuned by $-983\,\mathrm{MHz}$ from the exact hyperfine transition $\mathrm{F} = 5/2 \rightarrow \mathrm{F}' = 7/2$. An inhomogenous magnetic field is then applied to keep the atoms in resonance with the transition exploiting the Doppler-shift due to the velocity of the atoms. There is a residual magnetic field leaking from the Zeeman slower into the MOT chamber which is compensated by magnetic coils dedicated to this purpose, thus, once the atoms enter the MOT chamber they are not in resonance anymore with the detuned light.

3.3.2 Magneto-Optical Trap

For the magneto-optical trap (MOT) three orthogonal laser beams at 556 nm are used, which is the wavelength of the intercombination transition $^1\mathrm{S}_0 \rightarrow {}^3\mathrm{P}_1$. The MOT is operated at the hyperfine transition $\mathrm{F} = 5/2 \rightarrow \mathrm{F}' = 7/2$ in order to avoid optical pumping into dark states. Since this transition is quite narrow ($\Gamma_{556} = 2\pi \times 182\,\mathrm{kHz}$), 18 sidebands are added to the laser beam in order to increase the range of the atoms' velocity classes that can be addressed. These sidebands are all red-detuned with respect to the carrier frequency and separated by 600 kHz to each other. At this stage either 10^8 atoms of the fermionic ^{173}Yb isotope or 10^9 atoms of the bosonic ^{174}Yb isotope can be trapped. After 20 s the number of atoms trapped by this multi-frequency MOT stage is saturated, the sidebands are turned off and the carrier frequency and intensity are optimized for the minimization of the atom cloud's temperature. The temperature reached for the ^{173}Yb isotope is $T \approx 25\,\mu\mathrm{K}$, which is low enough to achieve an efficient transfer from the MOT to the in-vacuum Fabry-Perot cavity.

3.3.3 In-Vacuum Fabry-Perot Cavity

The in-vacuum Fabry-Perot cavity is injected by a laser at 1064 nm which is kept in resonance by a Pound-Drever-Hall locking scheme [12]. A transfer efficiency of about 80 % is reached with a trap depth of $V_0/k_B \approx 800\,\mu\mathrm{K}$ and a beam waist of $w_0 \approx 300\,\mu\mathrm{m}$. The transfer is conducted by compressing the MOT and moving it to the center of the cavity's dipole trap, which is done by using three orthogonal compensation coils to move the position of the point where the quadrupole magnetic field vanishes. After the successful transfer, MOT beams and magnetic fields are switched off and the cavity is used as a first evaporative cooling stage. For this purpose the trap depth is exponentially lowered to $V_0/k_B \approx 60\,\mu\mathrm{K}$ leaving 10^7 atoms at roughly $\mathrm{T} \approx 3\,\mu\mathrm{K}$.

Table 3.1 – Trap frequencies of the crossed dipole trap for each direction and the averaged trap frequency $\bar{f} = (f_x \cdot f_y \cdot f_z)^{1/3}$.

f_x (Hz)	f_y (Hz)	f_z (Hz)	$\bar{f}$ (Hz)
53.8 ± 0.5	99.5 ± 0.5	90.3 ± 0.6	78.4 ± 1.0

3.3.4 Optical Transport and Crossed Dipole Trap

The actual experiments are not conducted directly in the MOT chamber but in a glass cell with high optical access. For the transportation of the atoms a different branch of the 1064 nm laser is used as a dipole trap, the center of which, i.e. the focus of the beam, is moved from the center of the Fabry-Perot cavity to the glass cell using a focusing lens on the air-bearing translation stage AEROTECH ABL 1500b. By moving the focusing lens of the beam, the strong focus ($P = 3.4\,\mathrm{W}, w_0 = 30\,\mu\mathrm{m}, V_0/k_B \approx 90\,\mu\mathrm{K}$) is shifted as well. With an efficiency of about 30 % the atoms are transferred from the in-vacuum cavity to the transport beam by lowering the injection power adiabatically to an idle value[2]. Then, the atoms are transported 26.4 cm in 2.5 s with an efficiency of approximately 66 %.

When the atoms arrive in the glass cell another branch of the 1064 nm laser system is used to form another dipole trap ($P = 3.0\,\mathrm{W}$, $w_0 = 60\mu\mathrm{m}$), which is orthogonal to the transport beam. In this crossed dipole trap consisting of two laser beams in the horizontal plane the final evaporative cooling stage is performed which leads to quantum degeneracy. In this cooling stage an exponential ramp is performed for each dipole beam. For the transport beam the power is lowered from $P_{\mathrm{initial}} = 3.4\,\mathrm{W}$ to $P_{\mathrm{final}} = 35\,\mathrm{mW}$ with a ramp duration of $T_{\mathrm{ramp}} = 3.5\,\mathrm{s}$ and a ramp decay constant of $\tau_{\mathrm{ramp}} = 3\,\mathrm{s}$. For the other beam the parameters are: $P_{\mathrm{initial}} = 3.0\,\mathrm{W}$, $P_{\mathrm{final}} = 1\,\mathrm{W}$, $T_{\mathrm{ramp}} = 6.1\,\mathrm{s}$, $\tau_{\mathrm{ramp}} = 2.95\,\mathrm{s}$. At the end of the evaporation 1.2×10^5 degenerate ^{173}Yb atoms, distributed over all six nuclear spin states, are routinely obtained with a temperature of $T \approx 0.15\,T_{\mathrm{F}}$ ($T_{\mathrm{F}} \approx 200\,\mathrm{nK}$). The measured characterizing trap frequencies of the final crossed dipole trap are shown in Table 3.1.

3.3.5 Optical Lattices

For all experiments described in this thesis the degenerate atoms are loaded in a three-dimensional optical lattice which is created by three orthogonal and retroreflected beams at a wavelength of 759 nm. One of the beams is aligned with the vertical direction and the other two are in the

[2] The power is not lowered to zero in order to be able to keep the laser locked to the cavity for the next experimental cycle. However, it is sufficiently lowered to enable the transport.

Table 3.2 – Lattice beam waists w_0 and trap frequencies $f(s)$ (orthogonal to the corresponding lattice beam direction).

	Lattice 1	Lattice 2	Lattice 3
w_0 (μm)	96.1	111.3	102.3
$f(s)$ (Hz)	$7.1\sqrt{s}$	$6.2\sqrt{s}$	$6.8\sqrt{s}$

horizontal plane as the crossed dipole trap, one of which thereby forms an angle of 35° with the transport beam. The beam powers of the lattices are actively stabilized by standard feedback loops and in Table 3.2 the beam waists are estimated and the measured harmonic trapping frequencies are shown.

3.4 Nuclear Spin Manipulation and Detection

In this section the possibilities for nuclear spin manipulation and detection are presented and explained.

3.4.1 Spin Distribution Detection

A Stern-Gerlach technique is usually used in ultracold gases experiments in order to separate different spin components in space, thus, enabling to distinguish different spin states. Unfortunately, ^{173}Yb is strongly diamagnetic and only possesses a nuclear spin and not an electronic spin in its ground state. Therefore, a standard Stern-Gerlach magnetic field cannot be used for spin separation, however, the *optical Stern-Gerlach effect* [123, 130] can be exploited to image spin distributions.

As already discussed in section 1.1.3 the dipole potential of laser radiation for detunings in the order of the hyperfine splitting depends on the atom's spin orientation m_F. In the specific case of the $^1\mathrm{S}_0\,(F=5/2) \rightarrow {}^3\mathrm{P}_1\,(F'=3/2,5/2,7/2)$ transition, equation (1.14) becomes

$$V_{\mathrm{dipole},m_F} = \frac{3\pi c^2 3\Gamma}{2\omega_0^3}\left(\frac{|\mathscr{C}_{7/2,m_F}(q)|^2}{\delta_{7/2}} + \frac{|\mathscr{C}_{5/2,m_F}(q)|^2}{\delta_{5/2}} + \frac{|\mathscr{C}_{3/2,m_F}(q)|^2}{\delta_{3/2}}\right) I(\vec{r}), \tag{3.1}$$

where $\delta_{F'} = \omega - \omega_{F'}$ are the detunings from the specific hyperfine state. The laser beam is aligned normal to the horizontal plane and is not directly centered on the atomic cloud but

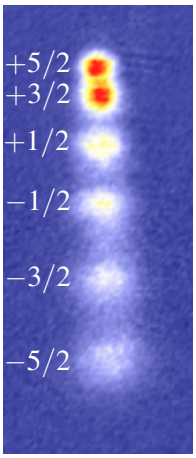

Figure 3.9 – Spin distribution detection. The figure shows a false-color absorption image of a degenerate gas of ^{173}Yb atoms after applying the optical Stern-Gerlach technique. Each gathering of atoms corresponds to a certain nuclear spin state as denoted on the left side. For further details see text.

with a distance in such a way that the atoms experience the maximum intensity gradient. A square pulse of 1.25 ms is used with 10 mW of a σ^- polarized laser beam with a detuning of $\delta_{7/2} = -566\,\text{MHz} \approx -3100\,\Gamma$ and a waist of $w_0 = 60\,\mu$m in order to split the atoms of different m_F states in the horizontal plane after a time of flight (i.e. the time between releasing the atoms from any dipole traps and the absorption imaging) of 4.5 ms. The quantization axis is defined by a bias magnetic field of 2.5 Gauss along the vertical axis. An example image for the detection of the six different spin states for ^{173}Yb can be seen in Figure 3.9.

3.4.2 Spin Distribution Preparation

The nuclear spin components of ^{173}Yb can be individually addressed by the narrow $^1S_0$ (F $= 5/2) \rightarrow {}^3P_1$ $(F' = 7/2)$ transition when a magnetic field is applied which separates the $^3P_1$ $(F' = 7/2)$ states with $\Delta m_F = 1$ by $\Delta_Z = 2\pi \times 595 \cdot B\,\text{kHz/Gauss}$ due to a Zeeman shift. The magnetic field used for this has a value of 23 Gauss resulting in $\Delta_Z = 2\pi \times 13.7\text{MHz} \approx 75\Gamma$. Then, two independent circular polarized beams can be used to address transitions $m_F \rightarrow m_{F'} = m_F \pm 1$ and pump the atoms in the desired hyperfine ground sublevels (see Ref. [105] for details). With this method a gas with basically any number of spin components between one and six can be achieved. However, for the experiments of this thesis only the preparation of a spin-polarized gas with only one spin component is of interest. In the experimental procedure this pumping to certain spin states takes place just after the atoms have been transported to the glass cell and before the evaporative cooling is performed so that the dipole trap is deep enough to contain the

atoms during the pumping processes. In the case of the spin-polarized gas preparation evaporative cooling is performed with a two-spin mixture to enable collisions between the fermions, then an additional blast pulse is executed after the evaporation in order to eliminate atoms in one of the two remaining spin states.

3.4.3 Spin-Selective Imaging

The Raman beams experiment described in this thesis requires the measurement of the atomic momentum distribution of only one spin component, the $m_F = -1/2$ of the $^1S_0$ ground state. The optical Stern-Gerlach (OSG) method cannot be used for this purpose, since the momentum distribution measurement and the OSG technique require different time-of-flight expansion times in the setup, in combination with the fact that the OSG beam may distort the atoms' momentum distribution in the desired direction. Moreover, the 399 nm transition is too broad to allow for spin-selective imaging since for practically reachable magnetic fields all spin states are always in resonance with this transition. Imaging on the 556 nm transition could be considered but the approach described below results in a significantly better signal-to-noise ratio because of a higher photon absorption rate.

Just as for the spin distribution preparation (see section 3.4.2) a combination of pump and blast pulses is used, but now after the actual experiment rather than before and during the first 2.5 ms of time-of-flight expansion at a magnetic field of $B = 15$ Gauss. The sequence of the pulses is as follows: Atoms in the $-5/2$ spin state are blasted away with a resonant pulse on the $^1S_0(F = 5/2, m_F = -5/2) \rightarrow {}^3P_1(F' = 7/2, m_{F'} = -7/2)$ transition. Atoms in the $m_F = +3/2$ spin state are first pumped into the $m_F = +5/2$ spin state and then blasted away with a resonant blast pulse on the $^1S_0(F = 5/2, m_F = +5/2) \rightarrow {}^3P_1(F' = 7/2, m_{F'} = +7/2)$ transition. Since the spin states $m_F = -3/2, +1/2$ are only negligible populated (as it will be clearer in section 5.1), only the $m_F = -1/2$ spin state remains. The proper functionality of this spin-selective imaging is checked in OSG images before each experiment.

4 Spin-Orbit Coupling with an Optical Clock Transition

As mentioned in section 2.1.1 there are basically two different schemes for the implementation of spin-orbit coupling (SOC) in ultracold atomic gases using either two-photon Raman transitions or an optical clock transition. In this chapter experimental results on the novel technique of the latter case are reported. The specific system is described and evidences for the functioning of the method are presented. Furthermore, advantages in comparison to other methods for the implementation of spin-orbit coupling are pointed out.

The first proposal to use the optical clock transition in ytterbium atoms for the production of gauge fields in superlattices was done in Ref. [43], whereas in Ref. [137] it was first proposed that the single-photon coupling can induce a non-negligible SOC, when the two electronic states are treated as the two possible spin projections of an effective spin-$1/2$ system.

4.1 Comparison to Other Techniques

Before the first experimental results are presented a short comparison of the novel technique to other techniques for the implementation of SOC is done in this section.

One of the main advantages of using a single-photon clock transition instead of a two-photon Raman transition is the avoidance of heating due to spontaneous emission from an intermediate state. For example, in experiments with ^{40}K atoms heating rates of about $0.3\,k_B T_F/(50\,\mathrm{ms}) = 6 k_B T_F/s$, where T_F is the Fermi temperature and k_B is the Boltzmann constant, were measured and attributed to the limitations of the Raman technique [25]. With the experimental parameters described in this thesis (intensity of about $1\,\mu\mathrm{W}/(\mathrm{mm}^2)$), other atomic energy levels are so far from resonance that the calculated heating rate due to spontaneous emission is lower than $10^{-9} k_B T_F/s$. Such a rate is ten orders of magnitude smaller than the heating associated with the Raman method and completely negligible. It is not even measurable in the experiment.

On the other hand, the use of a clock transition requires first of all an element, which possesses a clock transition in the optical regime and, furthermore, it requires a highly stabilized laser

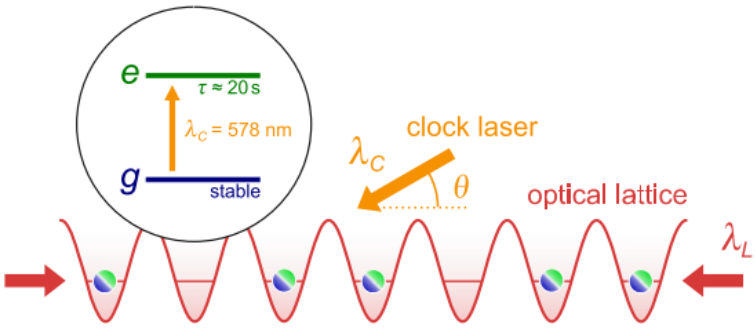

Figure 4.1 – Sketch of the experimental setup. The atoms are confined in one-dimensional tubes with a shallow lattice at the magic wavelength. The clock laser beam intersects the tubes under a certain angle θ. For further details see text.

source (see section 3.2.4) in order to be able to address the very narrow transition. On the contrary, the Raman method can be used in many more elements of the research field of ultracold atomic gases. Even though depending on the element spontaneous emission can be more or less influential.

Furthermore, two promising and quite different techniques for the generation of SOC exist, which both claim to be able to avoid heating from spontaneous emission. Firstly, in Ref. [85] an approach is proposed where Raman transitions are used to couple orbital levels in a double-well potential, which are treated as pseudospin states. Secondly, in Ref. [126] it is proposed to use a periodically driven magnetic field gradient to create spin-dependent tunneling in an optical lattice and additionally use a radio-frequency coupling of the two spin states.

4.2 Characteristic Double-Peak Spectra

The first experimental evidence for the successful implementation of spin-orbit coupling is the observation of characteristic double-peak spectra, which are connected to *Van Hove singularities*. In this section the results on this observation are presented with a detailed description of the experimental setup and procedure.

A scheme of the experimental setup can be seen in Figure 4.1. An ultracold gas of spin-polarized ($m_F = -5/2$) ^{173}Yb fermions is adiabatically loaded into a two lattice system.[1] One lattice in

[1] In principle also a three lattice system with two lattices at high trapping depth would be theoretically possible for the conducted measurements. However, in the experimental implementation the additional lattice has been observed to cause distortions in the spectrum. Most likely because of the additional trapping potential, causing deviations of the spectrum from the plain lattice bands shown in Figure 4.2.

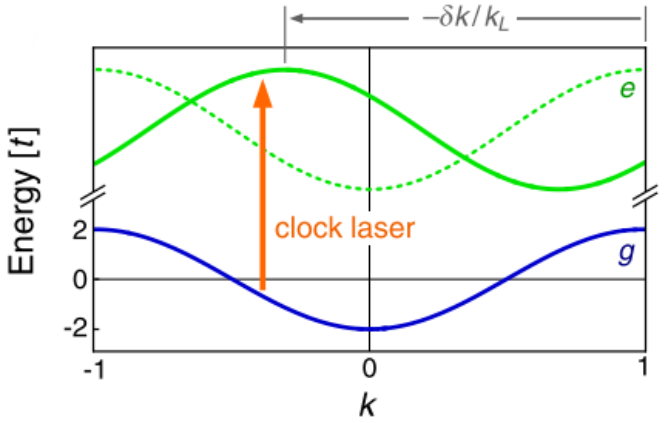

Figure 4.2 – Band structure of the ground and excited state. The blue solid line shows the lattice band of the ground state, whereas the green dotted line shows the lattice band of the excited state in the first Brillouin zone. For reasons of illustration the excited band is shifted by $-\delta k/k_L$ and reflected at the boundaries of the Brillouin zone leading to the solid green line. For the solid lines the clock transitions are vertical in the momentum space picture.

the vertical direction is operated at high trapping depth $s = 30$. It keeps the atoms from falling down and freezes any atomic motion along the vertical direction. This lattice is needed since all other dipole traps are switched off in order to avoid state-dependent light shifts, whereas the light shifts of the lattices are state-independent as the lattices are operated at the magic wavelength (see Figure 1.1). The other lattice in the horizontal plane is at a low trapping depth $3 \leq s \leq 11$ so that tunneling processes along this direction are still possible (see Figure 1.4(a)). The π-polarized clock laser hits the shallow lattice under a certain angle θ and can drive the ${}^1\mathrm{S}_0\ (m_\mathrm{F} = -5/2) \rightarrow {}^3\mathrm{P}_0\ (m'_\mathrm{F} = -5/2)$ transition. For the measurements conducted here $\theta = 0$ and only motion along the shallow lattice direction is of interest. In the general case, a ground state atom with a certain quasimomentum k along the shallow lattice direction, defined in units of k_L in this chapter, is coupled to the excited state with a quasimomentum of $k + \delta k/k_\mathrm{L}$, where $\delta k = k_\mathrm{C} \cos\theta$ is the transferred momentum depending on the angle θ between the clock laser and the shallow lattice. Thus, the clock laser couples

$$|g, k\rangle \rightarrow |e, k + \delta k/k_\mathrm{L}\rangle\,. \tag{4.1}$$

These transitions can be displayed in momentum space for the lowest lattice band of the ground and excited state in a usual manner as vertical transitions when the excited band is shifted exactly by $-\delta k/k_\mathrm{L}$ and reflected at the boundaries of the first Brillouin zone (see Figure 4.2). This shift is performed for a better visualization of the resulting spectra. In Figure 4.2 it can be seen that the energy difference, i.e. the vertical distance, between the two solid bands depends on the

quasimomentum k. Therefore, the spectrum broadens as the band width increases, i.e. as the lattice is lowered. This is the first expected influence of the SOC on the spectrum. The second observable alteration is related to the following. The density of states correlates with the gradient of the energy bands in a way that the density of states diverges at stationary points where the gradient is zero. These divergences are Van Hove singularities and they can be observed as peaks in the spectrum [6]. In the case described here two peaks are expected in the spectrum for the two transition frequencies with the highest combined density of states of the lower and higher band. These peaks are induced by the Van Hove singularities of the individual bands but because of the chosen momentum transfer δk the stationary points of the two bands are not directly coupled by the clock laser. Hence, the highest combined density of states is reached between the individual Van Hove singularities, i.e. for the minimal and maximal energy differences, which are reached in Figure 4.2 at approximately $k \simeq 0.8$ and $k \simeq -0.2$. The exact shape of the spectrum depends on the shift of the excited band and therefore on the transferred momentum δk. In particular the two peaks are expected to have the maximum contrast with respect to the rest of the spectrum for $\delta k = k_{\mathrm{L}}$ since for that case the regions with the highest density of states (the stationary points) of the two bands are directly coupled.

4.2.1 Experimental Observation

The laser used for driving the very narrow clock transition is stabilized by the locking scheme described in section 3.2.4, where in particular it should be noticed that a recently established fiber link infrastructure to the Italian National Institute for Metrological Research (INRiM) [19, 29] is exploited. For the experimental observation of the spectra the clock laser is aligned with the shallow lattice ($\theta = 0$) leading to a momentum transfer of $\delta k = 1.31\, k_L$. The clock laser illuminates the atoms for an interrogation time between 100 ms and 800 ms which is long enough to be in the incoherent regime, where Rabi oscillations can be neglected, which would otherwise influence the spectrum strength as the Rabi frequency Ω_{Rabi} depends on the detuning Δ_{Rabi} from resonance:

$$\Omega_{\mathrm{Rabi}} = \sqrt{\Omega_{\mathrm{Rabi},0} + \Delta_{\mathrm{Rabi}}}, \tag{4.2}$$

where $\Omega_{\mathrm{Rabi},0}$ is the Rabi frequency on resonance.

The experimental results are shown together with the theoretical predictions on the single-particle level in Figure 4.3(b) for different lattice depths s_x starting from the Lamb-Dicke regime to an increasingly shallower lattice from top to bottom. The broadening of the spectrum can be calculated as follows.

The two lattice bands can be described by the two cosine functions [6]

$$-2t\cos(k) \qquad \text{and} \qquad -2t\cos\left(k + \frac{\delta k}{k_L}\right). \tag{4.3}$$

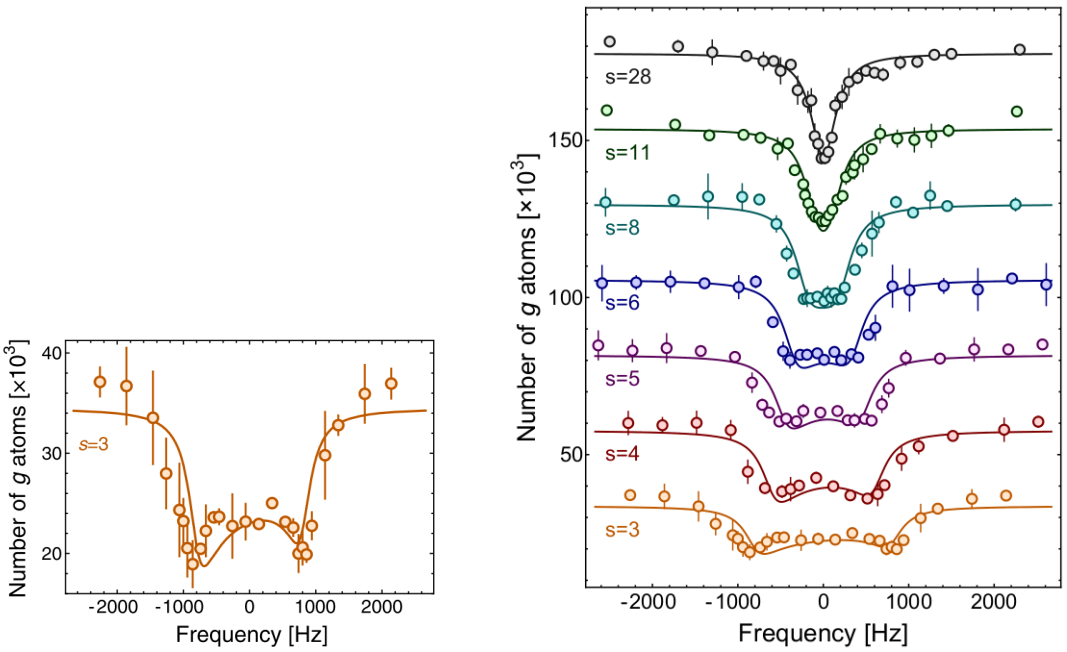

(a) **Single spectrum.** Clock transition spectrum in a lattice with $s = 3$, $t = 2\pi \times 220\,\mathrm{Hz}$ and $\delta k = 1.31 k_L$.

(b) **Spectra in dependence on the lattice depth.** Clock transition spectra for different lattice depth. Data sets with $s \geq 4$ have been offset vertically for the sake of presentation.

Figure 4.3 – Clock transition spectra. The plots show the number of atoms remaining in the ground state after a 800 ms interrogation time. The horizontal axes show the detuning with respect to the center of the spectra. The points are averages over multiple measurements and the error bars are standard deviations. The solid lines are the result of a single-particle theoretical model.

Their energy difference is

$$\Delta E = \omega_0 + 2t\left(\cos(k) - \cos\left(k + \frac{\delta k}{k_L}\right)\right), \tag{4.4}$$

where ω_0 is the resonance frequency in the Lamb-Dicke regime and for the following ω_0 is set to be zero. Using the identity

$$\cos(x) - \cos(y) = -2\sin\left(\frac{x+y}{2}\right) \cdot \sin\left(\frac{x-y}{2}\right) \tag{4.5}$$

ΔE becomes

$$\Delta E = 4t\left(\sin\left(k + \frac{\delta k}{2k_L}\right) \cdot \sin\left(\frac{\delta k}{2k_L}\right)\right). \tag{4.6}$$

The minimum and maximum energy difference ΔE_{min} and ΔE_{max} are then

$$\Delta E_{\text{min}} = -4t\left|\sin\left(\frac{\delta k}{2k_L}\right)\right| \qquad \text{and} \qquad \Delta E_{\text{max}} = 4t\left|\sin\left(\frac{\delta k}{2k_L}\right)\right|. \tag{4.7}$$

Therefore, the total broadening of the spectrum is $8t|\sin(\delta k/(2k_L))|$, which can be seen in Figure 4.3. The spectra for $s \geq 4$ are vertically displaced for the sake of presentation. In order to demonstrate how evident the two emerging peaks are, the strongest signal for $s = 3$ is additionally shown in a separated plot in Figure 4.3(a).

In the experiment the resolution of the two peaks and the spectrum in general is limited to the linewidth of the spectroscopy peak in the Lamb-Dicke regime (see section 1.3) since it reflects how well a precise[2] transition frequency can be resolved. The resolution limit is not determined by the natural linewidth of $\approx 10\,\text{mHz}$ and also the contribution due to the finite coherence time of the laser, which is below 50 Hz, is not the main constraint. Instead, the resolution is mostly limited by a power broadening as the laser is operated at a power of a few 100 nW with a spot size of approximately $(600-800)\,\mu\text{m}$ and the saturation intensity for the transition is $260\,\text{pW/cm}^2$. Therefore, the spectroscopic resolution function can be approximated with a power-broadened Lorentzian line profile with a full width at half maximum of $\approx 340\,\text{Hz}$ derived from a fit to the spectrum at $s = 28$ in Figure 4.3(b). Because of this limited resolution the measured spectrum is the convolution of the theoretical curve (assuming perfect resolution) and the experimental spectroscopic resolution function.

The observed spectroscopy peaks indicate the successful implementation of momentum-transferring transitions and are a first signature of SOC according to Ref. [137].

[2] The Lamb-Dicke regime in the case described here at $s = 28$ features lattice bands of $< 10\,\text{Hz}$, which is flat with respect to the experimental resolution, i.e. the transition frequency is defined much more precise than the resolution limit.

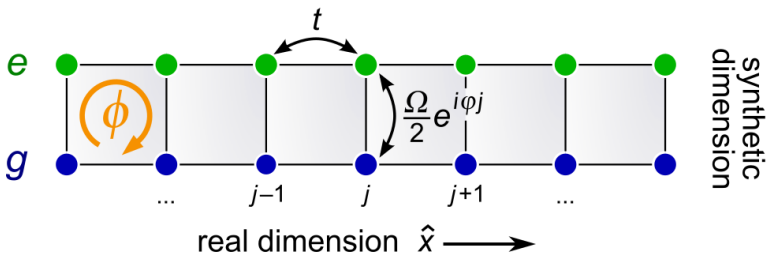

Figure 4.4 – System scheme. Using the synthetic dimensions approach the internal state of the atoms can be treated as a synthetic dimension with the two lattice sites: g and e. The clock transition then describes hopping along this direction with the amplitude $\Omega/2 \cdot \exp(i\phi j)$. The lattice site-dependent phase factor leads to a uniform synthetic magnetic flux ϕ piercing the effective two leg ladder system.

4.3 Synthetic Magnetic Flux

In this section the system used for the generation of SOC is described in more detail and particularly it is explained how the synthetic dimensions approach can be exploited to create a synthetic magnetic field.

The concept of synthetic dimensions (see section 2.2.2) can be exploited to treat the internal state of the atoms, i.e. the $|g\rangle$ and $|e\rangle$ state which can be seen as pseudo-spin states $|\uparrow\rangle$ and $|\downarrow\rangle$, as an extra dimension with only two lattice sites. Within this picture the driving of the clock transition can be seen as a hopping along the synthetic dimension with the complex amplitude $\Omega/2\exp\{i\phi j\}$ which depends on the lattice site j along the real dimension. In total, instead of a one-dimensional system an effective two-dimensional system is realized which looks like a two-leg ladder (see Figure 4.4). The Hamiltonian describing this system can be derived from the general Harper-Hofstadter Hamiltonian (2.11) and is called the Harper-Hofstadter ladder Hamiltonian:

$$H = -\hbar \left(t \sum_{\mathrm{j},\alpha} c^{\dagger}_{j,\alpha} c_{j+1,\alpha} + \frac{\Omega}{2} \sum_{j} e^{i\phi j} c^{\dagger}_{j,e} c_{j,g} \right) + \mathrm{H.c.} \tag{4.8}$$

where t is the tunneling amplitude along the real dimension and $c^{\dagger}_{j,\alpha}$ ($c_{j,\alpha}$) are fermionic creation (annihilation) operators on the site (j,α) in the real (j) and synthetic ($\alpha = e, g$) dimension. The phase ϕ in the complex phase factor $\exp\{i\phi j\}$ of the synthetic tunneling is the *Peierls phase* (see section 2.2.1) which leads to a behavior of the atoms on the two-leg ladder as if an external magnetic field were piercing it. Therefore, in this system the physics of a two-dimensional fermionic gas exposed to a (strong) magnetic field at ultralow temperature can be studied.

As already mentioned in 2.2.2 the synthetic dimensions approach distinguishes it from other

schemes for creating synthetic magnetic fields by the sharp boundaries in the synthetic dimension, which make the observation of chiral edge currents particularly simple (see section 4.4).

4.4 Chiral Currents

In this section the observation of chiral currents is described, which is the second strong evidence for the successful implementation of SOC in the system. This type of proof was already used in a previous work of this laboratory (see Ref. [91]). The occurrence of chiral currents also demonstrates the close relation to non-trivial topological quantum states as the quantum Hall effect and the quantum spin Hall effect (see section 2.3.1).

As described above the dressed states of the combined system consisting of the atoms and the clock laser is described by the Harper-Hofstadter ladder Hamiltonian (4.8). The dispersion relations of the dressed energy bands can be calculated by transforming the Hamiltonian into momentum space and diagonalizing it. The results are shown in Figure 4.5(a) for a transferred momentum $\delta k = 1.31 k_L$ in the limit of zero coupling $\Omega \to 0$ (dotted lines) and for $\Omega = t$ (thick lines) after a gauge transformation. The colors of the thick lines indicate the state composition, with the ground state represented in blue and the excited state represented in green. As it can be seen in Figure 4.5(a), the momentum distributions of the ground state atoms for the case with SOC and without SOC are different. Without SOC the atoms have a symmetric distribution around $k = 0$, whereas with SOC the distribution of the ground state atoms in the lowest dressed band features an asymmetry starting at a certain Fermi energy level, which depends on the coupling strength Ω and the transferred momentum δk. For a fully occupied lowest dressed band and for no population in the higher dressed state it can be seen in the band structure that the momentum distribution of the ground state atoms is centered around a finite momentum $k \neq 0$. This means that on the average the atoms move towards a preferred direction. For the excited state atoms the behavior is exactly the opposite, which can be understood in terms of the symmetry of the SOC. The result of this momentum distribution in the picture of the two-leg ladder is that the atoms on the lower leg (ground state) move in one direction, whereas the atoms on the upper leg (excited state) move in the opposite direction. This behavior is illustrated in Figure 4.5(b) and describes currents of atoms moving in the two-dimensional system in a chiral way. This is the reason why the presence of SOC in the described system is expected to feature chiral currents in contrast to the case without SOC.

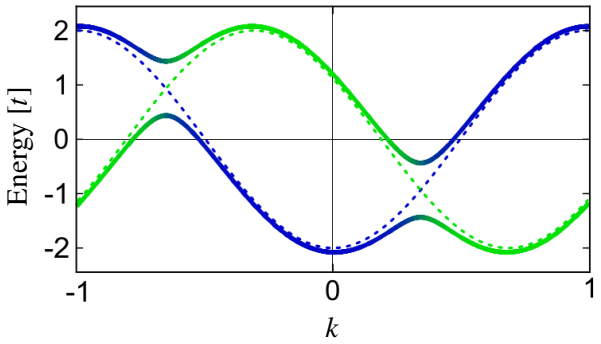

(a) **Band structure of the dressed system.** The plot shows the lattice bands of the bare system (dashed lines) and of the dressed system (solid lines) after a gauge transformation (equation (2.3)). The colors indicate the state decomposition, with the ground state represented in blue and the excited state represented in green. Experimental parameters: $t = 2\pi \times 138\,\mathrm{Hz}$, $\Omega = 2\pi \times 590\,\mathrm{Hz}$.

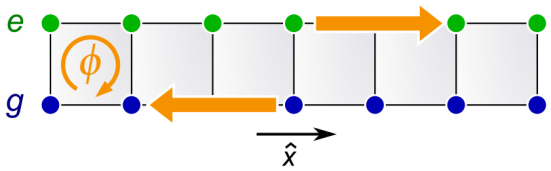

(b) **Chiral currents in the two-leg ladder.** The figure shows an illustration of the chiral currents corresponding to Figure 4.5(a). As the arrows indicate, atoms on the lower leg move on the average in negative $\hat{x}$ direction, whereas atoms on the upper leg move in the opposite direction.

Figure 4.5 – Prediction of chiral currents. The two figures illustrate why chiral currents are expected to occur in the spin-orbit coupled system and how they can be imagined in the two-leg ladder.

4.4.1 Measurement Procedure and Experimental Observation

The description of the measurement procedure in this section begins at the point where a spin-polarized, degenerate Fermi gas is trapped in the science glass cell. The scheme for reaching this stage of the experimental cycle is described in chapter 3.

One-Dimensional Tubes

The Fermi gas is adiabatically loaded into one-dimensional tubes along one lattice direction which will be in general referred to as the x direction. This is achieved by an exponential ramp on the intensity of the three lattice beams. The lattices in the y and z direction are ramped up to an intensity corresponding to $s_y \approx s_z \approx 20$ and the lattice along x to $s_x = 6$, which is deep enough to validate the tight-binding approximation (see section 1.3.1) but sufficiently low to allow tunneling processes. Therefore, atoms are only allowed to tunnel along x and can be treated as trapped in one-dimensional tubes.

As soon as the ramps on the lattices are completed, the crossed dipole trap, which was holding the atoms so far, consisting of the transport beam and the dipole trap beam (see section 3.3.4), is adiabatically turned off with a linear ramp. Otherwise, during the measurements the crossed dipole trap would influence the resonance frequency of the clock transition and atoms would see different confining potentials depending on their state. Moreover, confinement potentials are avoided as much as possible as they limit the number of lattice sites reachable by hopping. The lattice beams are strong enough to trap the atoms without the assistance of the dipole trap and do not influence the measurements like the crossed dipole trap would, since the lattices are operated at the magic wavelength (see section 1.1.2).

Adjustment of the Rabi Frequency

The chiral currents signal depends on how strong the ground and excited state of the clock transition are coupled. The physically relevant quantity for this is the Rabi frequency Ω_{Rabi} (see equation (1.34)), which is directly measurable by acquiring the population of ground state atoms after various interrogation times with the clock laser. A typical example of such a measurement is shown in Figure 4.6. Before each chiral currents measurement, firstly, Ω_{Rabi} is determined by the best fit of a cosine function to the data points and, secondly, the frequency is accordingly adjusted. The adjustment is performed by a correction of the clock laser power P_{clock}, which is possible because of the following relation between the two quantities:

$$\Omega_{\mathrm{Rabi}} \propto \sqrt{P_{\mathrm{clock}}}, \tag{4.9}$$

where equation 1.34 has been used.

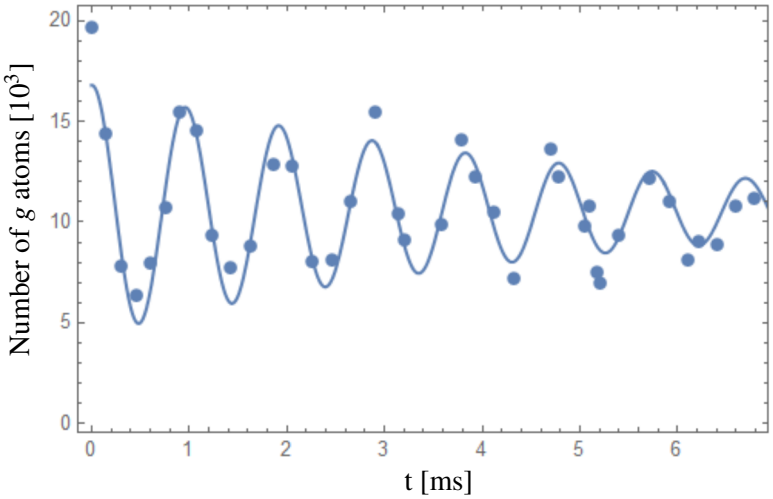

Figure 4.6 – Rabi frequency measurement. The figure shows a typical Rabi frequency measurement of the clock transition.

Loading of the Dressed States

The atoms in the one-dimensional tubes are adiabatically loaded into the lowest dressed state of the final system, which includes the permanent presence of the clock beam. This is achieved by a ramp on the detuning Δ_{ramp} of the form

$$\Delta_{\text{ramp}} = \Delta_0 \left(1 - \frac{1 - \exp^{-t/\tau}}{1 - \exp - T/\tau} \right), \tag{4.10}$$

which is very similar to an exponential ramp but ensures that at the end of the ramp ($t = T$) $\Delta_{\text{ramp}} = 0$. A typical set of parameters are: initial detuning $\Delta_0 = 2\pi \times 8\,\text{kHz}$, duration of the ramp $T = 15\,\text{ms}$ and $\tau = 4.5\,\text{ms}$.[3] During this ramp the atoms are always kept in the instantaneous eigenstate of the system with the lowest energy which is the lowest dressed state.

The successful loading of the dressed state is always experimentally verified before the actual measurement is performed. This is done in terms of an observation of the ground state population which must be around half the population observed in the initially prepared spin-polarized gas and which must be stable in time. The stability in time of the ground state population is required in order to make sure that the loading procedure leads to an eigenstate of the Hamiltonian. The time stability is investigated by keeping the clock beam on at resonance for various times after the ramp is completed. Furthermore, it is verified that the full population can be transferred back

[3] These values can slightly differ from measurement to measurement depending on the best results of the verification procedure of the successful loading of the dressed state described below.

to the ground state with a loading ramp and an unloading ramp directly performed after one another. An example for such a verification can be seen in Figure 4.7, where the three different cases are displayed: population of ground state atoms without loading the dressed state, with the loading of the dressed state and with the loading followed by an immediate unloading of the dressed state with the reverse frequency ramp. This proves that the system is still coherent after the loading and that the missing atoms in the ground state population is not a loss of atoms but indeed caused by the successful loading of the dressed state. Unfortunately, with the current setup of the experiment it is not possible to image the excited state, however, there are plans to include an imaging system for the $^3P_0$ state in the near future. Since there is no closed transition present for the excited state, in order to be able to image it, two additional laser sources would be needed to repump the atoms into the ground state before the actual imaging. For further details on this subject see Ref. [39]. The observation of both states would be an even clearer evidence for the successful loading of the dressed state.

Band-Mapping and Imaging

When the loading into the lowest dressed state is completed, a band-mapping procedure starts, where the atoms are adiabatically (i.e. conservation of the quasimomentum) unloaded from the three-dimensional lattice and the quasimomentum of a particle in a Bloch state is converted into a kinetic momentum in free space [50, 72, 77]. After a time of flight (TOF) of 23 ms the ground state atoms are imaged with an absorption spectroscopy using the $^1S_0 \rightarrow {}^1P_1$ transition at 399 nm, where the position of the atoms resembles their initial momentum, thus, the images show the momentum space distribution of the atoms (see Figure 4.9 for an example).

With this procedure the atoms of all the one-dimensional tubes are detected together in absorption spectroscopy, this means that it is not possible to distinguish between different tubes. Therefore, in the theoretical calculations the total spectroscopy signal, consisting of all occupied tubes, needs to be accounted for. The number of tubes containing the same number of particles can be assumed to be constant up to the highest number of particles, which is reached in the central tube. This statement can be verified by the following consideration.

When temperature effects are neglected, the single tubes are filled with particles up to the Fermi energy. The trapping potential V determines how many particles can populate a tube until the Fermi energy is reached. For example, 10 particles can populate a tube with $V < V_1$ and only 9 particles can populate a tube with $V_1 < V < V_2$. The potential difference between two adjacent potential boundaries $V_{\alpha+1} - V_\alpha$, where $\alpha \in \mathbb{N}$, can be denoted as ΔV and has a fixed value. The question is, how many tubes hold the same number of particles, i.e. how many tubes are localized in the area between two adjacent potential boundaries. The trapping potential is assumed to be well approximated by a harmonic potential within the area, where the dipole potential is strong enough to prevent the atoms from falling down. In addition, the trapping potential is assumed to

(a) **Without loading of the dressed state.** Number of ground state atoms $\approx 14,200$

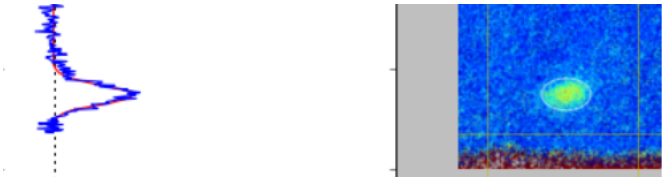

(b) **After loading of the dressed state.** Number of ground state atoms $\approx 8,200$

(c) **After loading and unloading of the dressed state.** Number of ground state atoms $\approx 15,900$

Figure 4.7 – Coherence check for the dressed state. The figures show a typical representation of the experimental verification method used to determine, whether the coherence of the system is preserved when the dressed state of the system is adiabatically loaded. The right part of the figures shows the false-color absorption images after a time of flight of 23 ms. The left part of the figures shows the integrated signal along the horizontal direction of the images on the right. The higher the peak the more atoms are present. The number of atoms is determined by finding the best fit of the atom distribution function to the integrated signal with the atom number as a fit parameter.

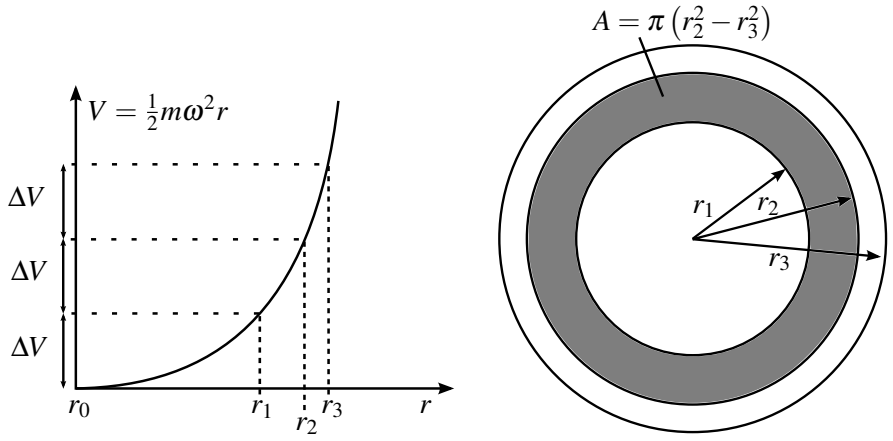

(a) **Harmonic potential.** The harmonic potential is divided into zones with the same potential difference ΔV.

(b) **Area calculation.** The figure illustrates the area calculation of the different zones with constant ΔV as done in equation (4.12).

Figure 4.8 – Calculation illustration. The figures show an illustration of the considerations leading to a constant number of tubes with the same number of particles up to the highest number of particles reached in the central tube.

be symmetric with respect to rotation around the x-axis. Hence, radii r_α in the plane orthogonal to x can be defined as corresponding to the boundary potentials V_α and two adjacent radii fulfill the relation

$$\frac{1}{2}m\omega^2\left(r_{j+1}^2 - r_j^2\right) = \Delta V = \text{constant}, \tag{4.11}$$

where m is the mass of a particle and ω its oscillation frequency in the harmonic potential (see Figure 4.8(a)). The area enclosed by these two adjacent radii is (see Figure 4.8(b))

$$A = \pi\left(r_{j+1}^2 - r_j^2\right) = 2\pi \cdot \frac{\text{constant}}{m\omega^2} = \text{constant}. \tag{4.12}$$

The area for all tubes with the same number of particles is constant regardless of the number of particles and the spacing between the tubes is determined by the transverse lattices and, thus, also constant. Therefore, the number of tubes with the same number of particles is constant up to the highest number of particles reached in the central tube.

Experimental Observation

For the experimental observation of the chiral currents TOF images of the ground state atoms for a fully occupied lowest dressed band and no population in the higher dressed band are analyzed.

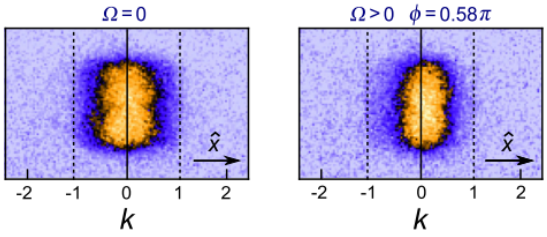

(a) **TOF images.** The figure shows false-color absorption images after a TOF of 23 ms.

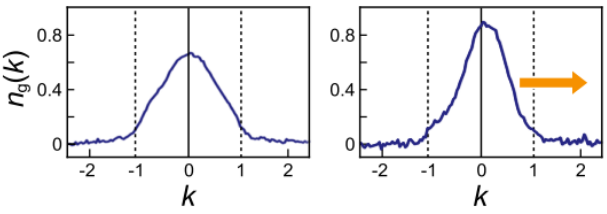

(b) **Momentum distribution function.** $n_g(k)$ is renormalized to $\int n_g(k)\,\mathrm{dk} = 1$ after the TOF images have been integrated along the vertical direction.

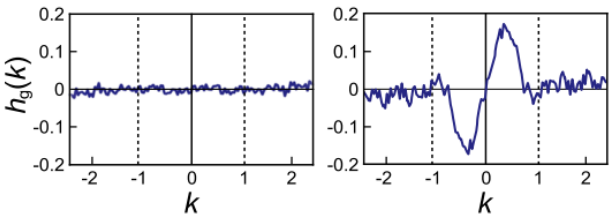

(c) **Asymmetry function.** The asymmetry function defined as $h_g(k) = n_g(k) - n_g(-k)$ shows the most evident signal for the horizontal displacement of the atoms in momentum space, i.e. for the chiral currents.

Figure 4.9 – Chiral currents detection. The six figures illustrate the experimental detection of chiral currents. While the figures on the left show the case without SOC ($\Omega = 0$), the figures on the right show a case example with SOC: $\Omega = 2\pi \times 590\,\mathrm{Hz}$, $\phi = 0.58\pi$. The left figures serve as a reference to determine the center of the first Brillouin zone at $k = 0$, whereas the right figures show a chiral current signal manifested in an asymmetry of the atoms' momentum distribution and in a displacement of the atoms' center of mass along the $\hat{x}$ direction. The chiral current signal becomes more and more evident from the top figures to the bottom figures.

Several images are taken for each measurement and the signal is averaged to a single image. Reference images without the presence of the clock laser ($\Omega = 0$) are taken in order to determine the center of the Brillouin zone at $k = 0$. This reference case is shown in the three subfigures of the left column in Figure 4.9, whereas an example measurement with the clock laser present ($\Omega = 2\pi \times 590\,\mathrm{Hz}$) and a magnetic flux of $\phi = 0.58\pi$ is shown in the three subfigures of the right column. The first top figures show the averaged TOF images, the middle figures show the momentum distribution $n_g(k)$ of the ground state atoms, which is normalized to $\int n_g(k)\,\mathrm{dk} = 1$ after integration along the vertical direction and the bottom figures show the asymmetry function defined as $h_g(k) = n_g(k) - n_g(-k)$. As mentioned above k is defined in units of k_L. From top to bottom the discrepancies between the two columns become clearer, i.e. in the bottom row the displacement of the ground state atoms momentum distribution to the right side is the most evident. This means, that the atoms are not centered around $k = 0$ but around a positive momentum $k > 0$, thus, on the average the ground state atoms move towards positive $\hat{x}$ direction. Hence, the system with SOC features chiral currents (assuming the opposite behavior for the excited state atoms, which as mentioned above cannot be imaged due to technical reasons).

4.4.2 Higher Dressed State

A further evidence for the correct interpretation of the experimental results is the loading of the higher dressed state, which in case of a correct theoretical understanding of the experimental system should feature a complementary momentum distribution with respect to the lowest dressed state's distribution. This can be seen in the band structure of the dressed bands in Figure 4.5(a), where the blue part of the higher dressed state fills exactly the momentum space of the first Brillouin zone, which is not covered by the blue part of the lowest dressed band.

The higher dressed state can be loaded, when the frequency ramp on the clock laser (see equation (4.10)) is inverted in the sense that the sign of the initial detuning is reversed ($\Delta_0 \to -\Delta_0$) so that in the picture of the Bloch's sphere the Bloch vector initially points in the opposite direction than for the lower dressed state. However, it is not sufficient to only perform this inversion since there is a blue sideband present in the spectrum corresponding to a transition from the lowest lattice band of the electronic ground state $|g_0\rangle$ to the first excited lattice band of the electronic excited state $|e_1\rangle$ and the distance of this blue sideband to the actual resonance for typical measurement parameters is lower than the initial detuning for the dressed state loading procedure. This is not a problem for the loading of the lowest dressed state since $|g_1\rangle$ is not initially populated (which is tested in TOF images, where only the first Brillouin zone is occupied) and therefore a $|g_1\rangle \to |e_0\rangle$ transition cannot occur. This problem is solved by increasing the lattice depth of the shallow lattice to $s_x = 20$ when the loading of the lattices is performed. Then at the same time the dressed state is loaded and the lattice is decreased to $s_x = 6$ using the same ramp parameters.

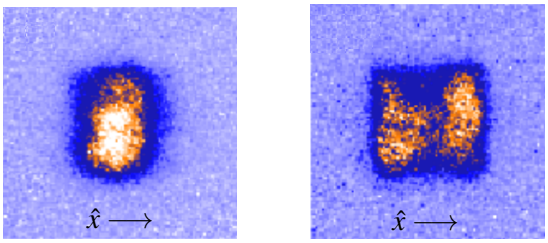

(a) **Lowest dressed state** (b) **Higher dressed state**

Figure 4.10 – TOF images of the dressed states. The figures show the false-color absorption images of the two dressed states after a TOF of 23 ms.

At high lattice the blue sideband has a sufficiently large distance to the resonance in order not to interfere with the higher dressed state loading.

The averaged TOF image of the higher dressed state together with an averaged TOF image of the lowest dressed state for the same experimental parameters is shown in Figure 4.10. The complementary population of the first Brillouin zone can be recognized. Hence, this supports the correct understanding and interpretation of the experimental system.

4.5 Tunability of the Magnetic Flux

Even more interesting than the pure occurrence and observation of chiral currents associated with a certain magnetic flux in the system, is the fact that the magnetic flux is tunable and that it is, thus, possible to probe the chiral currents as a function of the magnetic flux.

It is possible to conduct chiral current measurements for different values of the magnetic flux

$$\phi = \pi \frac{\delta k}{k_\mathrm{L}} = \pi \frac{k_\mathrm{C}}{k_\mathrm{L}} \cos\theta \tag{4.13}$$

by changing the angle θ between the clock laser and the shallow lattice. Therefore, a system with a fully tunable flux in the regime $-1.31\pi \leq \phi \leq 1.31\pi$ is realized. The sign of ϕ is only a matter of definition and the limit of $|\phi| \leq 1.31\pi$ is given by the maximum of the transferred momentum in the current setup $\delta k_\mathrm{max} = k_\mathrm{C} = 1.31 k_L$. Theoretically this limit could even be expanded by changing the effective lattice spacing d by changing the angle between the shallow lattice and the other two lattices. However, when the periodicity of the Harper-Hofstadter ladder Hamiltonian (4.8) $H(\phi) = H(\phi + 2\pi)$ is taken into account the whole range of $0 \leq \phi \leq 2\pi$ is already accessible.

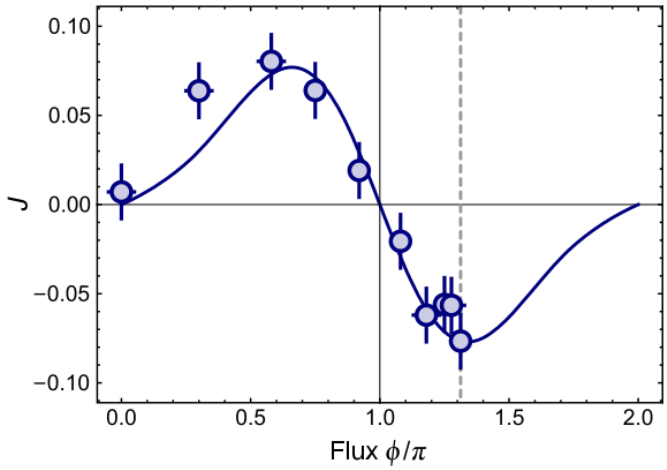

(a) **Chiral currents in a lattice.**

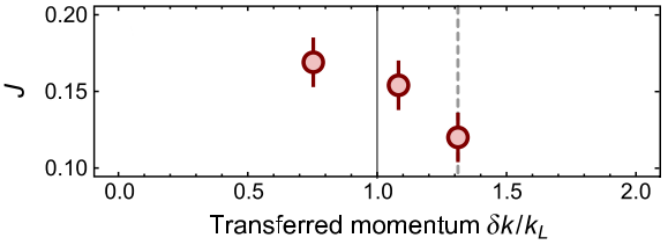

(b) **Chiral currents in free space.**

Figure 4.11 – Chiral currents as a function of the magnetic flux. The plots show the chiral currents function $J = \int_0^1 h_g(k)\,\mathrm{dk}$ as a function of the magnetic flux ϕ in a lattice (upper figure) and of the corresponding transferred momentum $\delta k/k_L$ in free space (lower figure). The horizontal scales of the two plots coincide as $\phi/\pi = \delta k/k_L$ (see equation (4.13)). The data points are partially averages over several single measurements and the error bars are the standard deviation calculated of five individual measurements for $\phi = 1.31\pi$. The solid line in the upper figure is a theoretical calculation on the single-particle level (see section 4.5.2).

In order to be able to probe the chiral currents as a function of the magnetic flux, the ability to quantify the chiral currents is needed. For this purpose, the chiral currents function J is defined as

$$J = \int_0^1 \mathrm{d}k\, h_g(k). \tag{4.14}$$

The function can evaluate the strength and direction of the currents. The results for the measurements of J as a function of the flux ϕ can be seen in Figure 4.11(a). They show a very good agreement with a theoretical calculation on a single-particle level based on the exact diagonalization of a system of fermions in the two-leg ladder. In particular, the inversion of the currents for $\phi > \pi$ is notable and can be qualitatively understood by the symmetry of the system imposed by the boundaries of the first Brillouin zone (see Figure 4.5(a)). As a proof that this symmetry feature is imposed by the lattice, measurements without the lattice along the one-dimensional tubes were conducted for a transferred momentum δk corresponding to $\phi < \pi$ and $\phi > \pi$ (it is not possible to define a flux for a system without a lattice). The relation between flux and transfered momentum is expressed in equation (4.13), in particular, $\phi = \pi$ equals $\delta k = k_L$. In free space J does not show a change in sign as shown in Figure 4.11(b). The successful reproduction of the fundamental symmetry of the system supports the interpretation described in this thesis of the observed physics. Furthermore, in order to check that the measurement procedure works as expected it was verified that the measured J is the same for an exact opposite alignment of the clock laser beam.

For the alteration of the magnetic flux, it is necessary to change the laser alignment. Therefore, in comparison to the use of two Raman beams, the technique described in this thesis for generating SOC with an optical clock transition has the major advantage, that an alignment of a single beam is much simpler than an alignment of two beams. This fact makes the measurement described in this section experimentally accessible in the first place. Moreover, it is emphasized that such an additional degree of freedom in the adjustment possibilities of quantum system properties is highly valuable in the context of using ultracold atomic gases for quantum simulation.

4.5.1 Experimental Observation

In order to be able to compare the measurements at different flux the Rabi frequency for each alignment is measured and the power of the clock laser is adjusted accordingly (see also 4.4.1). An example for such a measurement can be seen in Figure 4.6. Five different alignments of the clock laser beam are realized leading to ten data points as for each alignment both of the two lattice beams in the horizontal plane can be successively used as the shallow lattice, whereas the vertical lattice always needs to be at high trapping depth in order to overcome the gravitational force on the atoms. The data points are partially averages over several single measurements and the vertical error bars are the standard deviation calculated of five individual measurements for

$\phi = 1.31\pi$, whereas the horizontal error bars are an estimation of the uncertainty on the measured angle θ. Since there is no physical reason for the error on J to depend on ϕ (or δk respectively), it is assumed that the error for $\phi = 1.31\pi$ resembles the error for all measurements.

4.5.2 Theoretical Model

For the theoretical model a single-particle two-leg ladder system of fermions with two lattice sites in one direction and 50 lattice sites in the other direction is considered. The number of sites along the real direction is larger than the number of sites which are effectively populated because the harmonic confinement[4] is taken into account. Moreover, it is considered that the TOF images are a summation over many inhomogeneously filled one-dimensional tubes as described in 4.4.1 and that therefore the measured chiral currents are an average over these tubes. For the calculations shown in Figure 4.11(a) the Harper-Hofstadter ladder Hamiltonian (4.8) is exactly diagonalized and a finite temperature is included, the value of which is fitted to the experimental data leading to $T = 0.6\hbar t/k_B$. The shape of the theoretical curve is robust against fine tuning of the underlying parameters and that in particular the inversion of the flux at $\phi = \pi$ and the symmetric behavior with respect to that point is determined by the fundamental symmetries of the system dictated by the lattice.

4.6 Summary

In this chapter a novel technique for the implementation of spin-orbit coupling in ultracold atomic gases was described and experimental results were reported. In this framework, several evidences for the functioning of the method were presented, such as the observation of characteristic double-peak spectra, which are connected to Van Hove singularities, and direct measurements of chiral edge currents. Furthermore, various experimental results support that the interpretation of the observed physics is correct: The higher dressed state's momentum distribution is complementary to the distribution of the lowest dressed state as theoretically expected and fundamental symmetries of the system dictated by the lattice could be reproduced and it could be shown that they are indeed caused by the lattice.

It was mentioned that the presented method avoids the necessity of an intermediate state far from resonance, which can induce heating and loss of coherence, and it was emphasized that the method features an unprecedented tunability of the magnetic flux, which has a high application potential in quantum simulation. Altogether, the results in this chapter offer new possibilities for

[4] The harmonic confinement is only considered for the direction along the many lattice sites as it is the case in the experimental setup.

the investigation of topological quantum phases with ultracold quantum gases. Perspectives for the method presented in this chapter are presented in 5.6 in combination with perspectives for the results in chapter 5.

5 Groundwork for the Investigation of Interaction Effects

In this chapter groundwork is conducted on how interactions between particles influence chiral currents. For this purpose, two-photon Raman transitions are used to couple different spin states of the ground state manifold. This approach was already characterized and investigated in detail in this laboratory (see Ref. [91, 93]). In principle the methods described in the following could also be implemented with the clock transition but the Raman approach is preferred because of the more extensive experiences with it.

For the investigation of interaction effects in ultracold Fermi gases, the Pauli exclusion principle needs to be considered, which forbids interactions between indistinguishable fermions. In particular, for interactions between different internal states, which are in principle distinguishable, the preparation of the state mixture needs to be taken into account. When the gas is originally prepared in a single state and then excited by a uniform coherent laser, the atoms evolve indistinguishable and the two-atom correlation function at zero distance remains to be zero, i.e. no interactions occur [20]. In this thesis it is assumed that the Raman transition does not leave the fermions indistinguishable because of the atoms' kinetic energy term in the lattice, which causes a momentum dependent detuning and leads to different time evolutions of the internal state of each fermion. Therefore, the fermions become distinguishable. However, in strongly interacting phases as Mott-like phases the adiabatic state preparation is more challenging and is an important, yet unresolved issue, which needs further investigation but which is not subject of this thesis and, thus, not further discussed.

5.1 Setup of the Experiment

The experimental setup for the Raman transitions is described in detail in Ref. [93]. In this section only the most relevant facts and parameters are listed.

Two Raman beams, with σ^+ and σ^- polarization components, are used to couple the $-5/2$ and the $-1/2$ nuclear spin states of the ground state manifold $^1S_0$ with a two-photon Raman transition (see Figure 5.1). The Raman beams are detuned from the ($^3P_1$, $F' = 7/2$) state by

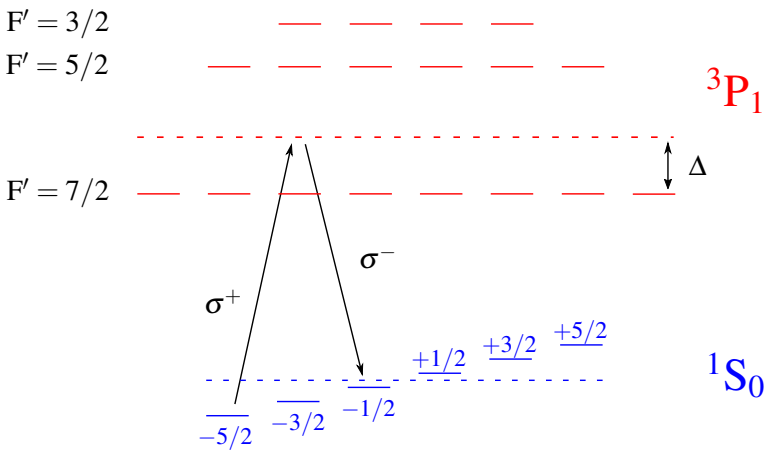

Figure 5.1 – Two-photon Raman transition scheme. Two Raman beams, with σ^+ and σ^- polarization components, are used to couple the $-5/2$ and the $-1/2$ nuclear spin state of the ground state manifold $^1S_0$ with a two-photon Raman transition. The Raman beams are detuned from the ($^3P_1$, $F' = 7/2$) state by $\Delta = 2\pi \times 1.876\,\text{GHz}$. Furthermore, a magnetic field of $B = 153\,\text{Gauss}$ is applied leading to a Zeeman shift of $\Delta_Z = 2\pi \times 32\,\text{kHz}$ for $\Delta m = 1$ in the $^1S_0$ state.

$\Delta = 2\pi \times 1.876\,\text{GHz}$. Furthermore, a magnetic field of $B = 153\,\text{Gauss}$ is applied leading to a Zeeman shift of $\Delta_Z = 2\pi \times 32\,\text{kHz}$ for $\Delta m = 1$ in the $^1S_0$ manifold. The Raman beams induce a spin state-dependent light shift (see section 1.1.3), which pushes the $+3/2$ spin state out of the Raman resonance. Otherwise three different spin states would be coupled leading to a more complex system, which is undesired in the experiments described in this chapter but was previously realized and analyzed in this laboratory (see Ref. [91, 93]). The angle between the beams is about 19° and the angle between the direction of the transfered momentum and the horizontal lattices are 35° and 55° , which leads to possible magnetic fluxes of $\phi = \{0.26\pi, 0.37\pi\}$ but only the higher flux of $\phi = 0.37\pi$ is used in the measurements described in this chapter.

5.2 Measurement Procedure

Since each measurement in this chapter is based on the detection of chiral currents, this section is used to describe the main measurement procedure for their observation and variations are explained directly in the respective sections. The occurrence of chiral currents for the Raman method has the same origin as for the clock transition method, which is described in section 4.4, since the theoretical description is independent of the experimental implementation (see section 2.1.1). In addition, the measurement procedure is very similar to the one with the optical clock

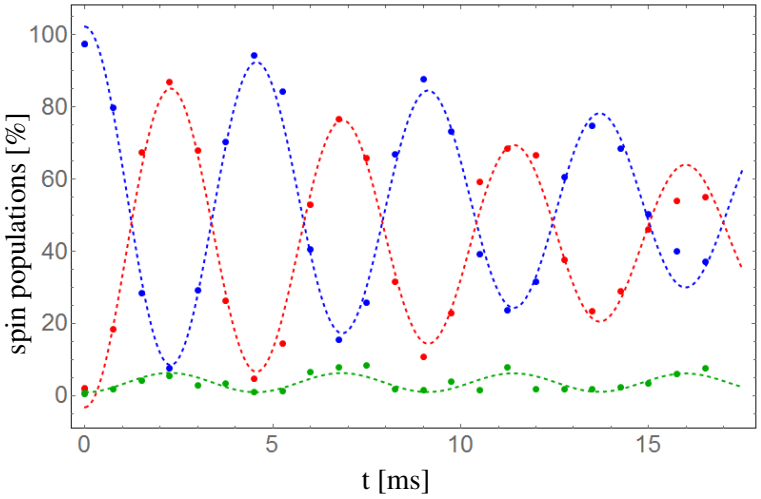

Figure 5.2 – Rabi frequency measurement. The figure shows a typical Rabi frequency measurement of the Raman transitions. The colors denote the different spin states: $-5/2$ (blue), $-1/2$ (red) and $+3/2$ (green). The dotted lines are fitted cosine functions used to extract the Rabi frequency.

transition (see section 4.4.1). Hence, only alterations are pointed out. Again, the description begins at the point where a spin-polarized, degenerate Fermi gas is trapped in the science glass cell. The scheme for reaching this stage of the experimental cycle is described in chapter 3.

One-dimensional tubes with $s_y \approx s_z \approx 30$ and $4 \leq s_x \leq 12$ are accomplished in the same way as in the last chapter and again the shallow lattice is flat enough to allow tunneling but deep enough to be in the tight-binding regime. Moreover, the measurements with the Raman beams have also the necessity of adjusting the Rabi frequency by beam power corrections and again the Rabi frequency is determined by the best fit to a Rabi oscillation measurement as shown in Figure 5.2.

Loading of the Dressed States

The procedure for the loading of the dressed states is quite different for the Raman method in comparison to the clock transition approach since the coupled states are different.

The dressed state is loaded with the same ramp (equation (4.10)) but in this case on the detuning of the second Raman beam instead of the clock laser's detuning. A typical set of parameters is: $\Delta_0 = 5.2\,\mathrm{kHz}$, $T = 5\,\mathrm{ms}$, $\tau = 1.2\,\mathrm{ms}$ for $s_x = 6$ and each Raman beam with a power of $30\,\mu\mathrm{W}$. However, the specific ramp parameters depend on Ω_{Rabi} since the loading needs to be slow in comparison to $1/\Omega_{\mathrm{Rabi}}$ and a higher Ω_{Rabi} results in a larger linewidth, which makes an

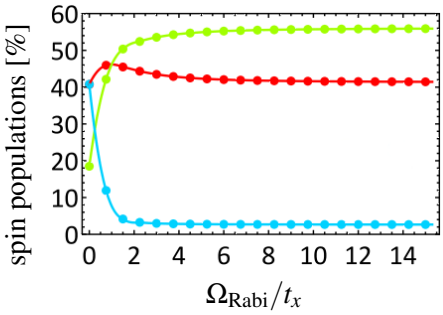

Figure 5.3 – Theoretical spin composition. The plot shows the characteristic spin compositions of the lowest dressed state in dependence on $\Omega_{\mathrm{Rabi}}/t_x$ for a fully populated lowest dressed band in the first Brillouin zone neglecting the harmonic confinement. The colors denote the different spin states: $-5/2$ (red), $-1/2$ (green) and $+3/2$ (blue). Adapted from Ref. [93].

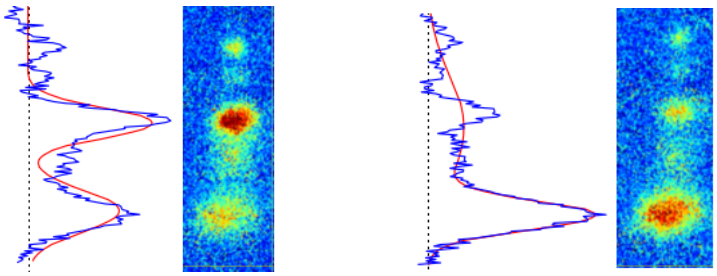

(a) **After loading of the dressed state.**

(b) **After loading and unloading of the dressed state.**

Figure 5.4 – Coherence check for the dressed state. The figures illustrate the coherence verification procedure for the loading of the dressed state (see text). They show false-color absorption images of the atoms' spin compositions on the right side and the corresponding signals, integrated along the horizontal direction, on the left side, respectively. The three most evident gatherings of atoms in both images correspond from top to bottom to atoms in the $+3/2$, $-1/2$ and $-5/2$ spin state. The fitted red curves in the integrated signals are of no interest for the coherence verification and can be ignored. The used parameters are: $\Omega_{\mathrm{Rabi}}/t_x = 3.7$, $\Delta_0 = 5.2\,\mathrm{kHz}$, $T = 5\,\mathrm{ms}$, $\tau = 1.2\,\mathrm{ms}$ for $s_x = 6$ and each Raman beam with a power of $30\,\mu\mathrm{W}$.

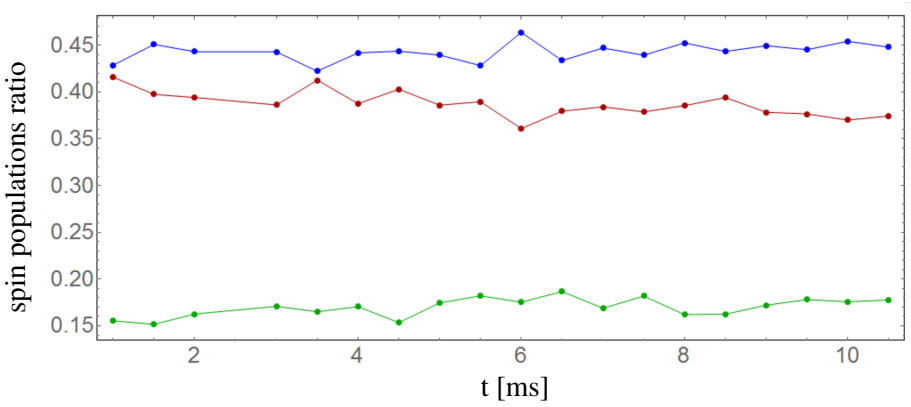

Figure 5.5 – Time stability check for the dressed state. The figure illustrates the time stability verification of the spin state composition after the dressed state loading (see text). The normalized population ratio of each spin component is displayed as a function of the holding time t with the Raman beams at resonance after the loading ramp is completed. The blue line corresponds to the relative population of the $-1/2$, the red line to the $-5/2$ and the green line to the $+3/2$ spin state. The parameters are: $\Omega_{\text{Rabi}}/t_x = 3.7$, $\Delta_0 = 5.2\,\text{kHz}$, $T = 40\,\text{ms}$, $\tau = 16\,\text{ms}$ for $s_x = 6$ and each Raman beam with a power of $30\,\mu\text{W}$.

adjustment of Δ_0 necessary. In this chapter the ratio Ω_{Rabi}/t_x is usually fixed. Therefore, the required ramp parameters change, when t_x, determined by the chosen s_x, changes.

The successful loading of the dressed state is always experimentally verified before the actual measurement is performed. The dressed state has a characteristic composition of the different spin components depending on the ratio Ω_{Rabi}/t_x as shown in Figure 5.3 for a fully populated lowest dressed band in the first Brillouin zone neglecting the harmonic confinement. In order to make sure that the atoms are indeed in the dressed state, it needs to be confirmed that coherence is not lost during the ramp and that the characteristic spin composition is stable in time, i.e. the system is in an eigenstate. The coherence is tested by performing the same ramp in the opposite direction and checking if the initial spin distribution (all atoms are in the $-5/2$ spin state) can be restored which must be the case in the coherent regime. A representative image of the spin composition of the dressed state after the loading and after the unloading with the inverse ramp can be seen in Figure 5.4. The time stability of the composition is investigated by keeping the Raman beams on at resonance for various times after the ramp is completed. In the case of the true dressed state the spin distribution does not oscillate, since the system is in an eigenstate. In Figure 5.5 an example of such a verification measurement is shown, in which the population of the $+3/2$ spin state is slightly increased in comparison to the theoretical calculations in Figure 5.3. This is mainly caused by imperfections in the Raman beams' polarizations, which increase the coupling strength to this spin state. Nonetheless, the time stability of the

Table 5.1 – Experimental access of relevant parameters. The table shows the relevant parameters for chiral currents in the system and how these parameters can be altered experimentally. The listed parameters are: the Raman coupling strength Ω_{Rabi}, the tunneling energy along the tubes t_x, the lattice depth along the tubes s_x, the power of the Raman beams P_{Raman}, the interaction energy U_{int}, the trap frequency along the tubes f_x, the transverse lattice depths s_y and s_z, the filling factor of the tubes ν and the total number of atoms N_{atom}. Issues may occur for parameters, which cannot be tuned individually (as marked in red).

Relevant parameters	Experimental access
U_{int}/t_x	$s_x \xrightarrow{changes} U_{\text{int}}$ and $\boldsymbol{t_x}$
Ω_{Rabi}/t_x	$s_x \xrightarrow{changes} t_x$, $P_{\text{Raman}} \xrightarrow{changes} \Omega_{\text{Rabi}}$
f_x/t_x	$s_x \xrightarrow{changes} t_x$, $s_y = s_z \xrightarrow{changes} f_x$ and $\boldsymbol{U}_{\text{int}}$
ν	s_x and $N_{\text{atom}} \xrightarrow{change} \nu$

populations demonstrates that the system is in an eigenstate.

Band-Mapping and Imaging

As described in section 3.4.3 it is possible to only image atoms of a single spin state, which is required for the observation of the chiral currents as each of the two coupled spin states features a current but the total current of both states is zero. Therefore, the TOF images only consist of a single spin component, which is chosen to be the -1/2 state. Despite the spin selective imaging sequence, the band-mapping and imaging is proceeded in the same way as for the clock transition technique and also in this case contributions from different tubes cannot be distinguished.

5.3 Experimental Access

The aim of the experiments conducted in this chapter is to investigate the behavior of chiral currents in dependence on particle interactions with respect to the tunneling energy scale, hence, the parameter of interest is U_{int}/t_x. The best way to investigate the effect of interactions (relative to the tunneling), would be to perform exactly the same measurements for different values of U_{int} without changing t_x since many other important energy-scale ratios of the system depend on the tunneling. The tunability of system parameters is one of the great advantages of quantum simulation with ultracold atomic gases and a lot of important parameters can be more or less tuned at will and independently of others. However, ytterbium as all other alkali-earth metals

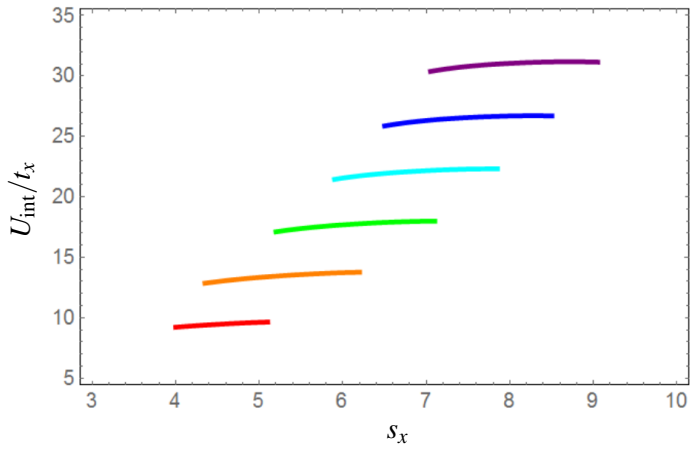

Figure 5.6 – Possible interaction ranges for constant trap frequency. The figure illustrates the possible ranges of U_{int}/t_x for a constant ratio of f_x/t_x. The colored lines refer to different ratios f_x/t_x from 0.3 (bottom red line) to 0.8 (top purple line). Even though along the lines s_x is changed, which alters t_x, the ratios are kept constant by adjusting $s_y = s_z$ accordingly. The horizontal width of the lines refer to a reasonable range of transverse lattice depths $15 < s_y = s_z < 40$ which is experimentally accessible and which keeps a low tunneling rate between the tubes. Figure courtesy of Leonardo Fallani.

or alkali-earth-like metals does not possess a magnetic Feshbach resonance since it does not have an electronic spin in its ground state.[1] Therefore, in this specific case the experimentally accessible quantity, which influences U_{int} is the lattice depth s_x, which changes not only the interaction but also the tunneling energy (see Figure 1.4). This means, the ratio U_{int}/t_x can be varied but the change in the tunneling energy also alters other relevant parameters and ratios of the system. In the best-case scenario these changes can be compensated by other experimentally accessible quantities or can at least be theoretically compensated in an exact analysis after the measurements. An overview about relevant quantities and experimentally accessible parameters related to this issue are listed in Table 5.1. In the following this issue is discussed.

Firstly, the tunneling changes the ratio Ω_{Rabi}/t_x, which can be easily compensated by changing the power of the Raman beams P_{Raman}, which directly controls Ω_{Rabi} since

$$\Omega_{\text{Rabi}} = \frac{\Omega_1 \Omega_2}{2\Delta} \propto E_{01} E_{02} \propto \sqrt{I_1 I_2} \propto \sqrt{P_1 P_2} = P_{\text{Raman}}, \tag{5.1}$$

where $I_\alpha \propto |E_{0\alpha}|^2$, $P_\alpha \propto I_\alpha$, $P_{\text{Raman}} := P_1 = P_2$ and the equations 1.43 and 1.34 were exploited. Secondly, the tunneling changes the ratio f_x/t_x. The trap frequency along the tubes f_x is experimentally accessible via the transverse lattice depths s_y and s_z (see Table 3.2). However, the

[1] The possibility of using the recently discovered orbital Feshbach resonance in combination with the clock transition is discussed in section 5.6.

transverse lattice depths not only alter f_x but also U_{int} in such a way that when it is tried to keep a steady ratio f_x/t_x while changing s_x, the accessible ranges for the ratio of interest, U_{int}/t_x, are negligible small. This is illustrated in Figure 5.6, where possible ranges for U_{int}/t_x are shown while keeping f_x/t_x constant. The colored lines refer to different ratios f_x/t_x from 0.3 (bottom red line) to 0.8 (top purple line). Even though along the lines s_x is changed, which alters t_x, the ratios f_x/t_x are kept constant by adjusting $s_y = s_z$ accordingly. The horizontal width of the lines refer to a reasonable range of transverse lattice depths $15 < s_y = s_z < 40$ which is experimentally accessible and which keeps a low tunneling rate between the tubes. Unfortunately, the ratio U_{int}/t_x is approximately constant within each line. In fact, increasing s_x, and thus decreasing t_x, means decreasing $s_y = s_z$ in order to decrease f_x, and this implies a decrease in U_{int}. Hence, it is not possible to explore large ranges of U_{int}/t_x while keeping the same value of f_x/t_x. The filling factor of the tubes ν is not related to the issue of direct experimental access to U_{int} but brings another degree of freedom for a possible analysis of the system, i.e. it can be used to gather further experimentally tested information (see section 5.5.2).

To summarize, the experimental access to the tuning of the desired quantity U_{int} is not directly given and, thus, compromises in the investigation of interaction effects have to be made by performing several indirect measurements.

5.4 Theoretical Predictions

A theoretical model is used to make predictions on the behavior of the chiral currents. Because of the issues with the experimental access to the interaction strength U_{int} discussed above in section 5.3, predictions need to be made for possible indirect measurements, which are discussed in this section. The theoretical calculations are conducted by the group of Rosario Fazio at the Scuola Normale Superiore di Pisa and related work can be found in Ref. [7, 8]. Their simulations showed that chiral currents can be strongly enhanced by repulsive atom-atom interactions for the filling factors considered in this chapter, i.e. with negligible population of the higher dressed band. The influence of a harmonic trapping confinement and finite-temperature effects were not considered.

For the predictions of this chapter density-matrix renormalization group simulations are used, disregarding temperature effects. Firstly, chiral currents are calculated in a single tube J_n, where n denotes the number of particles in the tube, as a function of the maximum filling factor ν_{max}, reached in the center of the tube, for $f_x = 55\,\mathrm{Hz}$ (corresponding to $s_y = s_z = 30$) and $\Omega_{\mathrm{Rabi}}/t_x = 4$. The filling factor along the tube is inhomogeneous because of the confining potential of the trap and the highest value is reached in the center of the tube, which is determined by the center of the harmonic confinement, i.e. where the confining potential has its minimum. The results

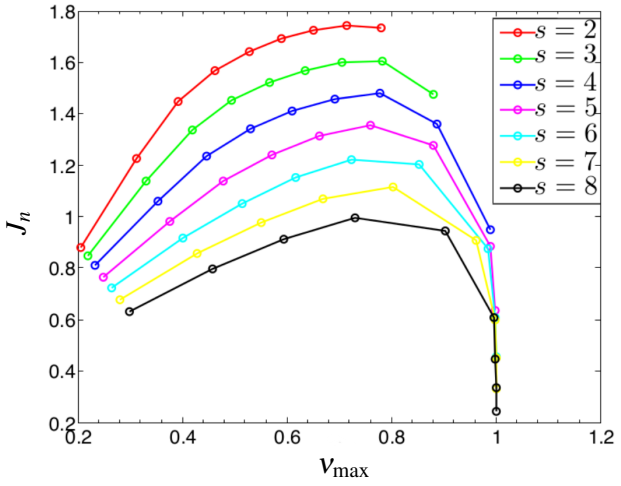

(a) **Single tube currents.** The chiral currents in a single tube J_n are shown as a function of the maximum filling factor $\nu_{\max}$, reached in the center of the tube, for $f_x = 55\,\mathrm{Hz}$ (corresponding to $s_y = s_z = 30$) and $\Omega_{\mathrm{Rabi}}/t_x = 4$, both fixed for all calculations. Each curve and color corresponds to a certain lattice depth s as denoted in the legend, which determines t_x and U_{int}, together with $s_y = s_z = 30$. The dots correspond to different numbers of particles in the tube starting from 2 particles on the left side adding two particles for the next dot and so on for up to 18 particles on the right side, i.e. from left to right: 2,4,6,8,...,18 particles.

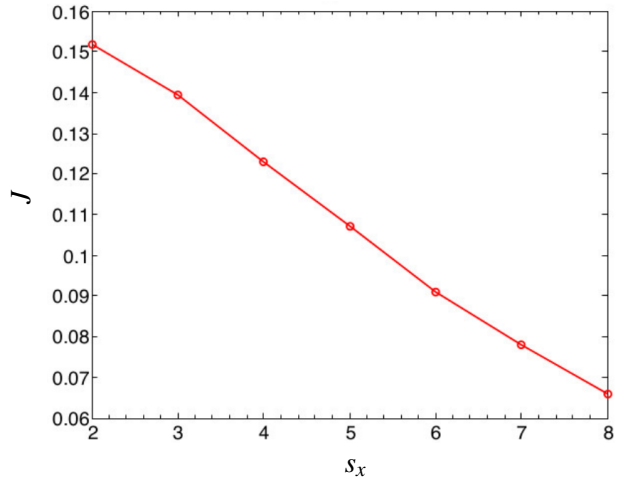

(b) **Total currents.** The figure shows the total chiral currents J as a function of the lattice depth s_x, where J is an average of J_n over all occupied tubes and was calculated using equation (5.2).

Figure 5.7 – **Theoretical predictions.** The figures show two different calculations conducted in order to derive theoretical predictions for possible measurements. Parameters are: $f_x = 55\,\mathrm{Hz}$ and $\Omega_{\mathrm{Rabi}}/t_x = 4$. Figure courtesies of Simone Barbarino.

are displayed in Figure 5.7(a), in which several experimentally reachable lattice depths (namely $s_x = \{2,3,4,5,6,7,8\}$) are considered. The lattice depth determines t_x and U_{int}, together with $s_y = s_z = 30$. The coordinate system is chosen in such a way, that the currents are positive. The dots correspond to different numbers of particles in the tube starting from 2 particles on the left side adding two particles for the next dot and so on for up to 18 particles on the right side, i.e. from left to right: 2,4,6,8,...,18 particles. The number of atoms are not directly associated with a certain $\nu_{\max}$ but the relation depends on s_x. For all lattice depths shown, the currents peak at an intermediate maximum filling ($\nu_{\max} \approx 0.75$) and for $\nu_{\max} = 1$ a *Mott insulator* phase (see Ref. [51]) forms at least in the center of the tube, which suppresses the chiral currents and inhibits any larger $\nu_{\max}$. Moreover, the different lines corresponding to different lattice depths never cross, which means that for a single tube the currents always decrease for a deeper lattice. If this is true for every single tube, then, it is also true for an average over all occupied tubes leading to the behavior of the total chiral currents J as a function of the lattice depth as shown in Figure 5.7(b). Following the considerations in section 4.4.1, the number of tubes with the same number of particles is constant up to the highest number of particles $N_{\max}$, so that the total chiral currents become

$$J = \frac{2}{N_{\max}(N_{\max}+1)} \sum_{n=1}^{N_{\max}} J_n, \tag{5.2}$$

where $N_{\max} = 18$ is the estimated number of particles in the central tube for the experimental parameters of the laboratory.

In the experiment only the total chiral currents can be measured. Hence, the results in Figure 5.7(a) cannot directly be experimentally tested, whereas the results in Figure 5.7(b) can be and are tested in the following section 5.5.1. Furthermore, predictions for the influences of the number of atoms and the trap frequency are made. Even though the calculations in Figure 5.7(a) are performed for a single tube the qualitative behavior of the currents as a function of the maximum filling is the same for the total chiral currents, when equation (5.2) is considered. The filling factor depends monotonically on the total number of particles, which means that again, when the currents are plotted as a function of the number of particles instead of as a function of the maximum filling, the qualitative behavior of the lines is not altered. This means, that in a measurement of the total chiral currents as a function of the number of atoms first an increasing behavior and then a decreasing behavior is expected.

A higher trap frequency increases the effective filling since less lattice sites can be populated by the atoms. Hence, again a monotonically dependence is given and a qualitative behavior as the one seen by the single tube currents in Figure 5.7(a) is expected, when the total currents are plotted as a function of the trap frequency.

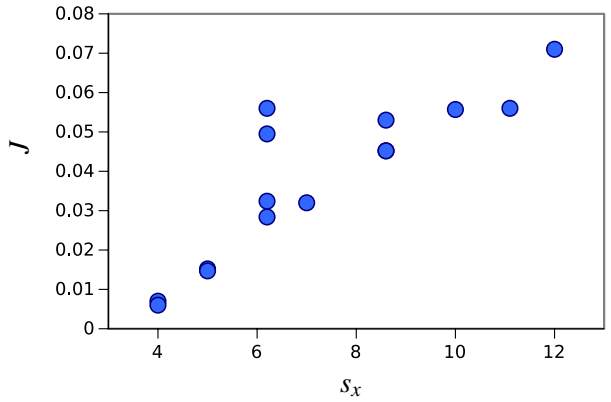

Figure 5.8 – Chiral currents dependence on the lattice depth. The figure shows J as a function of s_x. $\Omega_{\text{Rabi}}/t_x = 3.7$.

5.5 Experimental Results

In this section all the experimental results are reported, compared to the theoretical predictions in section 5.4 and conclusions are made. The synthetic magnetic flux $\phi = 0.37\pi$ is dictated by the beam geometry (see section 5.1) and fixed. Moreover, if not specified differently, the ratio $\Omega_{\text{Rabi}}/t_x = 3.7$ is fixed as well.

5.5.1 Lattice Depth Dependence

The measurement, which comes the closest to a direct analysis of interaction effects, is a measurement of chiral currents for different lattice depth s_x. As discussed in section 5.3 s_x influences both quantities U_{int} and t_x. The results on this measurement are reported and discussed in this section.

$\Omega_R/t_x = 3.7$ can be fixed by adjusting P_{Raman} (see section 5.3), while the ratios U_{int}/t_x and f_x/t_x are varied. The measured currents are shown in Figure 5.8 as a function of the lattice depth s_x. The data shows a clear enhancement of the chiral currents for increasing lattice depth and, thus, it shows a qualitative behavior exactly opposed to the theoretical prediction (see Figure 5.7(b)). In Figure 5.9(a) and Figure 5.9(b) the data of Figure 5.8 is displayed as a function of U_{int}/t_x and as a function of f_x/t_x respectively to illustrate that the observed behavior could be caused by interaction effects (see Figure 5.9(a)), by confinement effects (see Figure 5.9(b)) or by a combination of both. Figure 5.9(a) and Figure 5.9(b) demonstrate that both the ratios U_{int}/t_x and f_x/t_x vary significantly, hence, it is not possible to determine from these experimental data alone whether the observed dependency of J is caused by the interactions or by the confinement. In

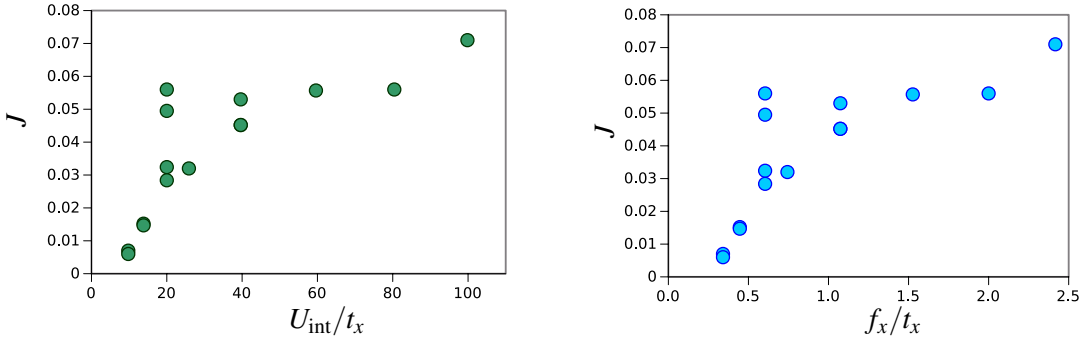

(a) **Currents as a function of interactions.** In this illustration trap frequency effects are ignored.

(b) **Currents as a function of trap confinement.** In this illustration interaction effects are ignored.

Figure 5.9 – Chiral currents dependencies. The figures show the same data of Figure 5.8 as a function of U_{int}/t_x and as a function of f_x/t_x respectively. $\Omega_{\mathrm{Rabi}}/t_x = 3.7$.

addition, the origin of the discrepancy between experiment and theory is unclear and needs to be further investigated. For this purpose, the theoretical model is further tested for its predictions of other possible experiments in the following sections. Moreover, the influence of the ratio f_x/t_x needs to be studied in order to be able to identify the genuine interaction effects.

5.5.2 Dependence on the Number of Atoms

In this section a measurement is described, which can be used to better understand the theoretical model and which can give some knowledge about the behavior of chiral currents in general. In this measurement only the number of atoms N_{atom} is changed, while all other parameters are kept constant.

Since the number of atoms can be determined in the TOF images taken for the measurement of the chiral currents, it is possible to organize the data with a postselection. Two measurements for $s_x = 7$ and $s_x = 11$, where $\Omega_{\mathrm{Rabi}}/t_x = 3.7$ respectively, are performed for various number of particles, where it is verified that population in the second Brillouin zone or higher is negligible, i.e. only the lowest lattice band is considerably occupied. The TOF images are then organized in six different N_{atom} bins (in 10^3): 1.5 - 3, 3 - 4, 4 - 5, 5 - 6, 6 - 7 and 7 - 9. The results of the chiral currents as a function of the number of atoms can be seen in Figure 5.10, where the two data sets are displayed after the currents have been normalized to the highest measured value. The two measurements have a good agreement and show a decrease in the currents with increasing number of atoms. This observation would agree with the theoretical calculations, if even for the lowest number of atoms the maximum filling were above approximately 0.75 (see Figure 5.7(a))

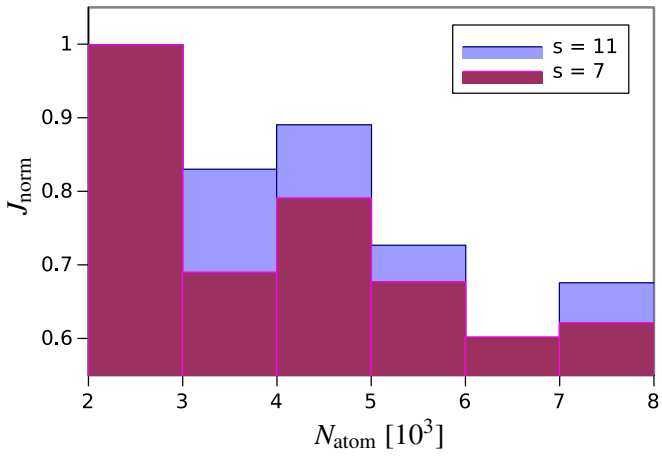

Figure 5.10 – Chiral currents dependence on the number of atoms. The figure shows the chiral currents as a function of the number of atoms N_{atom} for $s_x = 7$ and $s_x = 11$, where the currents are normalized to the highest measured value respectively and are therefore denoted as J_{norm}. The data is organized in six different N_{atom} bins (in 10^3): 1.5 - 3, 3 - 4, 4 - 5, 5 - 6, 6 - 7 and 7 - 9, where it was experimentally verified that population in higher lattice bands is negligible. $\Omega_{\mathrm{Rabi}}/t_x = 3.7$.

in the central one-dimensional tube, which features the highest ν_{max}. If ν_{max} were less than 0.75, a second discrepancy between experiment and theory would be revealed.

Another observation is that two small cuts seem to be present in the decreasing behavior for the two bins, $(3\text{ - }4)\cdot 10^3$ and $(6\text{ - }7)\cdot 10^3$. These cuts appear to be fluctuations in the measurements, firstly, because the accuracy of the measurements is in the same order of magnitude and, secondly, because they almost completely disappear, when the boundaries of all the bins are shifted by $0.5\cdot 10^3$. Nonetheless, it might be interesting to investigate this behavior further with more data sets.

To conclude, with the experimental data of this section alone it is impossible to determine whether the experimentally observed behavior of J in dependence on the number of atoms agrees with the theoretical calculations in section 5.4. In order to be able to derive such a statement, an independent information about the maximum filling in the central tube is necessary. One approach in this matter could be to determine ν_{max} by performing additional tests, for example, to use a theoretical model in order to estimate the number of atoms in the central tube from the total number of atoms (considering experimental parameters like the transverse confinement) and then determine the maximum filling according to the calculation in Figure 5.7(a).

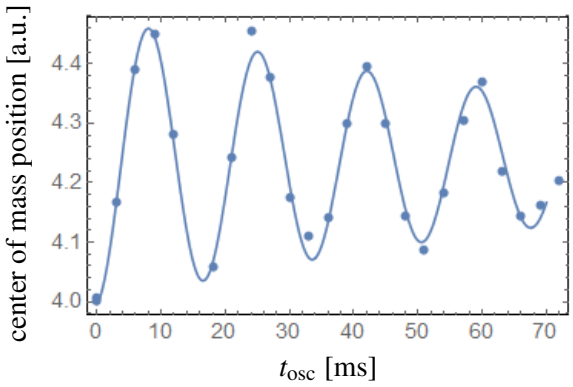

Figure 5.11 – Example trap frequency measurement. The atoms' center of mass position is shown in arbitrary units as a function of the oscillation time. The dots correspond to single position measurements, while the line shows a fitted cosine function to the data, which is used to extract the oscillation frequency, i.e. the trap frequency f_x.

5.5.3 Trap Frequency Effects

As mentioned in section 5.5.1 the effect of the increasing chiral currents with increasing lattice depth might be either dominated by increasing interaction strength U_{int}/t_x or by the increasing trap confinement along the tubes characterized by the trap frequency f_x/t_x. As discussed above it is not possible to only change the ratio U_{int}/t_x and observe the pure effect of interactions. However, it is possible to only modify the trap frequency and leave U_{int}/t_x unchanged by using the dipole trap of the transport beam (see section 3.3.4) which is usually completely switched off before the loading of the dressed state. A measurement is conducted in order to explore the confinement influence on the currents.

The trap frequency can be directly determined for each measurement by displacing the atom cloud with the dipole trap orthogonal to the transport beam (which can be adjusted by the use of a mirror mounted on a piezoelectric stack) and letting the atoms oscillate around the trap center along the tubes without the shallow lattice. The position of the atoms is recorded for various oscillation times t_{osc} and after enough data points are taken the evolution is fitted with a cosine function to determine the oscillation frequency, which is the trap frequency f_x. An example measurement for the case without additional confinement is shown in Figure 5.11. The contribution of the weak confinement caused by the focus of the shallow lattice can be neglected and is not considered in the measurements of the trap frequencies.

The chiral currents are measured as a function of the trap frequency f_x along the tubes for

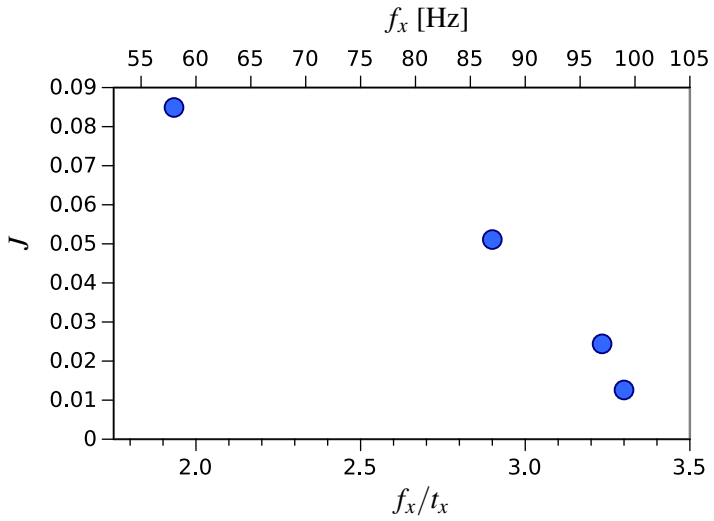

Figure 5.12 – Chiral currents dependence on the trap frequency. J is shown for $s_x = 11$ ($t_x = 2\pi \times 30\,\mathrm{Hz}$) and $\Omega_{\mathrm{Rabi}}/t_x = 3.7$ as a function of f_x and f_x/t_x. The trap frequency f_x is changed independently from the other parameters by using an additional confining beam (in contrast to the measurements displayed in Figure 5.9(b)).

$s_x = 11$ (high current signal) and $\Omega_{\mathrm{Rabi}}/t_x = 3.7$ starting at the lowest possible trap frequency caused exclusively by the transverse lattices. The trap frequency is increased by not completely switching off the transport beam for the measurement but keeping it at a finite value. The results in Figure 5.12 show that the currents decrease with increasing trap frequency, which is the opposite behavior as observed in Figure 5.9(b). Even though the parameter ranges coincide only in a small region of $f_x/t_x = [1.93, 2.42]$, this result suggests that the behavior seen in Figure 5.8 is due to interactions or at least due to a combination of interactions and confinement. However, since the issue of opposite behaviors in theory and experiment remains for the dependence of the chiral currents J on the lattice depth s_x, this result is classified as preliminary and should only be further evaluated, when all inconsistencies are resolved, in order to reduce the possibility of misunderstandings and false interpretations of the underlying physics.

5.5.4 Chiral Currents Lifetime

In order to increase the amount of information about the experiment, the time stability of the currents is investigated in this section. Strong decays could be a sign of deficiencies in the experimental approach.

The chiral currents are probed with different holding times t_{hold} after the loading of the dressed

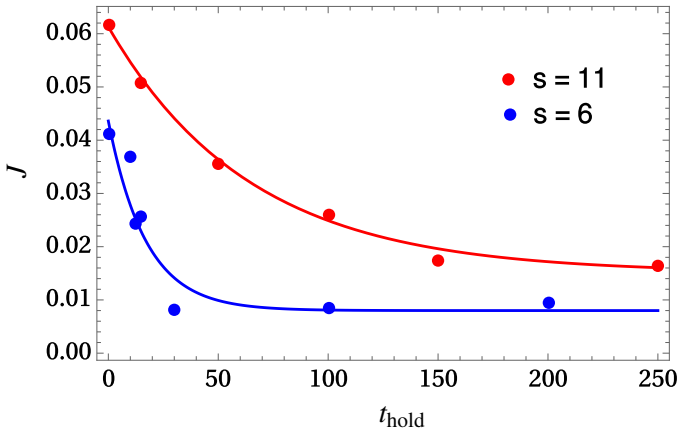

Figure 5.13 – Chiral currents lifetime. The figure shows two different lifetime measurements of the chiral currents for $s_x = 6$ (blue) and $s_x = 11$ (red), where for both measurments $\Omega_{\mathrm{Rabi}}/t_x = 3.7$. The displayed lines are fit curves to the two data sets of the form: $A + B \cdot \exp(-t_{\mathrm{hold}}/\tau_{s_x})$, which lead to the decay constants $\tau_6 = (17.1 \pm 5.8)\,\mathrm{ms}$ and $\tau_{11} = (64.5 \pm 7.5)\,\mathrm{ms}$.

state is completed, i.e. the system is given a various time to evolve before the imaging procedure starts. The results are shown in Figure 5.13. This lifetime measurement has been performed for $s_x = 6$ (orange) and $s_x = 11$ (blue) with fitted (an exponential decay is assumed) lifetimes $\tau_6 = (17.1 \pm 5.8)\,\mathrm{ms}$ and $\tau_{11} = (64.5 \pm 7.5)\,\mathrm{ms}$ respectively. For both measurements $\Omega_{\mathrm{Rabi}}/t_x = 3.7$. The given uncertainties are the standard errors of the fit functions and do not consider uncertainties on the single data points. Therefore, the genuine uncertainty is expected to be larger but not calculated since it is not of particular interest at this stage of the experiment. The measured lifetimes suggest that they are either approximately equal to twice the tunneling time $2/t_x$ or to half the Raman coupling time $1/(2 \cdot \Omega_{\mathrm{Rabi}})$, both cases would result in $\tau_6 = 20\,\mathrm{ms}$ and $\tau_{11} = 67\,\mathrm{ms}$. At the chosen detuning of $\Delta = 2\pi \times 1.876\,\mathrm{GHz}$ the spontaneous scattering rate of the Raman transition is only in the order of $10^{-3} \cdot \Omega_{\mathrm{Rabi}}$ [93] and, thus, it cannot be the main cause for the observed decay.

Another observation on these decays is that the signal does not go to zero but ceases to a finite value depending on the lattice depth, which is also not expected by the theoretical model. If the decay were caused by a loss of coherence, then after an infinite amount of time, the chiral currents should completely disappear: $J \xrightarrow{t_{\mathrm{hold}} \to \infty} 0$.

The encountered issues described in this section are observed in very preliminary measurements on the chiral currents lifetime. They could be caused by technical deficiencies and further investigations are necessary in order to draw any conclusions. This matter is further discussed in the following section and some investigations are described.

5.5.5 Issues Investigation

The experimental data of all measurements raises two issues, which might be related or not. Firstly, the theoretical prediction and the experimental observation of chiral currents in dependence on the lattice depth show the opposite qualitative behavior. Secondly, the lifetime of the chiral currents is much smaller than expected and the currents cease to a finite value instead of going to zero. The two issues are investigated in this section, possible explanations are discussed and suggestions for further studies are made.

The observed decays could explain the discrepancy between theoretical predictions and the experimental observations, if the measured signal at $t_{\mathrm{hold}} = 0$ is not identical with zero evolving time, i.e. if the currents already started to decay before the loading procedure of the dressed state is completed. An extrapolation of the decay lines to negative holding times leads to the value of $t_{\mathrm{hold}} \approx -25\,\mathrm{ms}$ at which the fitted chiral currents behavior for the two lattice depths is inversed and matches the theoretical predictions in Figure 5.7(b). This simple estimation is supposed to give a very rough approximation of the time when the decay may start, it ignores the possibility that the starting time of the decays may as well depend on the lattice depth. A decay start at $-25\,\mathrm{ms}$ would be theoretically possible since the dressed state loading times for acquiring the two data sets of the lifetime measurement were at least 40 ms. Therefore, in order to experimentally test this scenario, the dressed state loading time has been shortened as much as possible up to the point where the loading time is about 5 ms which is strongly below 25 ms (see for example Figure 5.4 with $T = 5\,\mathrm{ms}$). However, the results show the same J within experimental accuracy. Hence, the discrepancy between the trend of the experimental and theoretical data cannot be simply explained in terms of finite J lifetime.

Because of the finite value, the decay ceases to, the possibility of an insufficiently adiabatic loading is investigated, i.e. maybe an excited dressed state is loaded, which features higher chiral currents and then decays into the genuine ground state with a lower but stable chiral current signal (the finite value after the decay). However, theoretical simulations show that the loading procedure is robust against small perturbations and only small oscillations on the measured currents can be expected, which even in worst case scenarios cannot explain the observed decay. Moreover, even if the final value of the currents were the signal of the genuine ground state, the discrepancies between the theoretical model and the experimental observations on the behavior in dependence on the lattice depth cannot be solved as the lower lattice still shows a smaller signal than the higher lattice case.

Another possible explanation for the occurrence of the decays is that the Raman beams also couple the two-leg ladder to another spin state, the +3/2 state, which might not be sufficiently detuned and thus the coherence of the two-leg ladder system could be destroyed. A measurement for the investigation of this possible phenomenon is conducted in the following way. The third

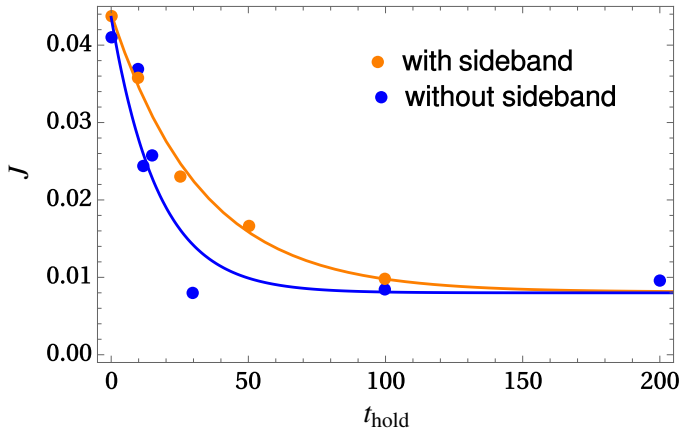

Figure 5.14 – Lifetime comparison. Lifetime measurements are plotted for the original case without a sideband (blue) and for the case of an additional sideband (orange), where $s_x = 6$ and $\Omega_{\mathrm{Rabi}}/t_x = 3.7$ for both cases. The displayed lines are fit curves as defined in Figure 5.13, which lead to $\tau_6 = (17.1 \pm 5.8)\,\mathrm{ms}$ for the original case and $\tau_6 = (32.6 \pm 6.1)\,\mathrm{ms}$ for the case with the sideband. If the point at $t_{\mathrm{hold}} = 30\,\mathrm{ms}$ is neglected, the lifetime without the sideband becomes $\tau_6 = (20.9 \pm 7.4)\,\mathrm{ms}$.

spin state is further pushed away from resonance by an additional light shift implemented with an additional sideband in one of the Raman beams. The sideband is far detuned from any other transitions and only contributes to the light shift caused by the two Raman beams (see section 1.1.3). It is experimentally verified that the $+3/2$ spin state is further detuned and that the system is still coherent by checking the Raman Rabi oscillations. Two independent measurements are performed for this configuration with the sideband and averaged for $s_x = 6$ and $\Omega_{\mathrm{Rabi}}/t_x = 3.7$. The fitted lifetime is $\tau_6 = (32.6 \pm 6.1)\,\mathrm{ms}$ and a direct comparison of this measurement with the sideband and the original measurement without the sideband are shown in Figure 5.14. As above the given uncertainties here are the standard errors of the fit functions and do not consider uncertainties on the single data points. Even though the lifetime is slightly increased with the sideband, it seems to be within experimental accuracy, which can be demonstrated by the fact that the fitted lifetime without the sideband increases to $\tau_6 = (20.9 \pm 7.4)\,\mathrm{ms}$ if only the point at $t_{\mathrm{hold}} = 30\,\mathrm{ms}$ is neglected. Therefore, it is concluded that a possible coupling to the +3/2 spin state is not the main cause for the decay of the chiral currents.

The most recent idea for a possible explanation of the discrepancy between theory and experiment is, that the system's temperature could depend on s_x, i.e. for a shallower lattice the temperature might be higher than for a deeper lattice and the increased temperature could decrease the chiral currents. So far, the theoretical calculations have all been performed at zero temperature. For the investigation of this possible temperature dependence, simulations are currently performed at the Scuola Normale Superiore di Pisa.

To conclude, the Raman transition technique with ytterbium atoms yields two issues, which need to be investigated further in order to derive reliable statements on the role of interactions in spin-orbit coupled systems. The investigations may result in a better understanding of this yet insufficiently studied research field. However, the lack of direct experimental access to pure interaction tuning in combination with non-negligible confinement effects reveals the limitations of the scheme presented in this chapter for the analysis of interaction effects and for this specific purpose other schemes should be taken into consideration (see the perspectives in section 5.6).

5.6 Summary and Perspectives

The aim of the experiment described in this chapter was to study interaction effects in a spin-orbit coupled system. For this purpose, a scheme of two-photon Raman transitions with ytterbium atoms was used. Challenges of the experimental access were discussed, theoretical predictions described and experimental results presented.

Moreover, a discrepancy between theory and experiment was observed together with unexpected short lifetimes. These issues were discussed, possible explanations were investigated and suggestions for further studies were made.

Altogether, the results of this chapter provide insight in the dependence of chiral currents on various system parameters, reveal experimental limitations, show first indications of interaction effects and can be used as a solid groundwork for further investigations on many-body effects in spin-orbit coupled systems.

5.6.1 Perspectives

In this section a few schemes for possible future experiments are shortly discussed demonstrating the potential of the results presented in chapter 4 and 5. There are many proposals for promising experiments with ytterbium atoms and the synthetic dimensions approach in general, such as the four-dimensional quantum Hall effect using a synthetic dimension additional to three real dimensions [111] or exploiting the two available synthetic dimensions for a vast amount of different connection possibilities leading to non-trivial topologies [15]. Here only two ideas for strongly related subjects to the presented work are discussed.

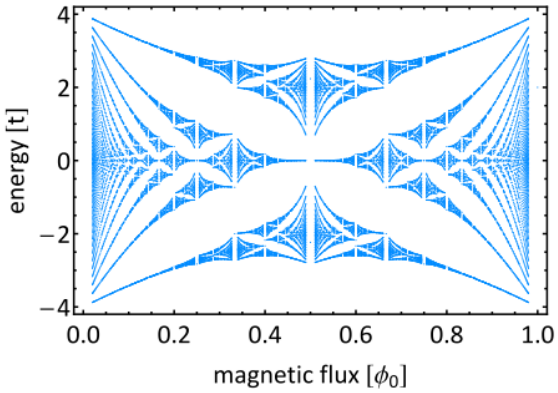

Figure 5.15 – Hofstadter's butterfly. The figure shows the fractal structure of the single particle energy spectrum as a function of the magnetic flux for electrons known as the Hofstadter's butterfly. Figure courtesy of Marco Mancini.

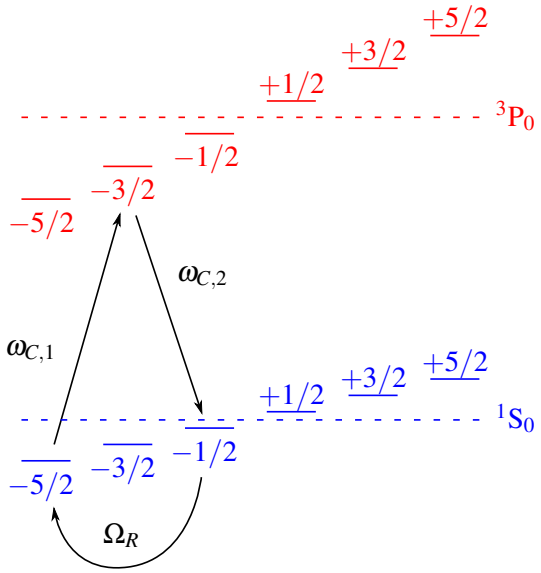

Figure 5.16 – Periodic boundary conditions. The figure shows a scheme for a possible realization of periodic boundary conditions in the synthetic dimension. $\omega_{C,1}$ and $\omega_{C,2}$ denote clock transitions, whereas Ω_R denotes a Raman transition. For further details see text.

Periodic Boundary Conditions

In the schemes discussed in this thesis the synthetic dimension only consists of two lattice sites, whereas in related work previously conducted in the laboratory also three lattice sites in the synthetic dimension where realized [91]. For three lattice sites periodic boundary conditions could be accomplished, when the first and last lattice site are directly coupled with a momentum transfer from the third site to the first, which must have the same direction as the momentum transfer from the first to the second and from the second to the third. The achievement of periodic boundary conditions could lead to the observation of the famous *Hofstadter's Butterfly*, which shows the fractal structure of the single particle energy spectrum as a function of the magnetic flux for electrons (see Figure 5.15). It occurs for the Harper-Hofstadter Hamiltonian (2.11) with periodic boundary conditions. Two possible ways for the implementation of periodically coupled states are described here. The first only relies on Raman transitions, whereas the second exploits a combination of Raman and clock transitions.

For the pure Raman scheme two $\sigma^+ + \pi$ transitions could be used for the already achieved coupling of three spin states. In addition, a $\sigma^- + \sigma^+$ transition for the coupling from the third state back to the first state would close the boundaries in the synthetic dimension (see also [93]). Individual control over the single Raman transitions and the avoidance of unwanted state couplings could be accomplished by the use of state-dependent light shifts (see section 1.1.3).

In the approach combining Raman and clock transitions the coupling scheme could be as shown in Figure 5.16. Firstly, the $|g, m_F = -5/2\rangle$ state is coupled to the $|e, m_{F'} = -3/2\rangle$ state via a σ^+ clock transition. Secondly, the excited state is coupled to the $|g, m_F = -1/2\rangle$ state using a σ^- clock transition and thirdly, the transition $|g, m_F = -1/2\rangle \rightarrow |g, m_F = -5/2\rangle$ is a standard Raman transition. As mentioned above the transferred momentum for all three processes must have the same direction. For the experimental realization it should be mentioned, that the two clock transitions can be distinguished from another in order to avoid unwanted transitions by exploiting the differences in the Zeeman shifts for the $^3P_0$ state and the $^1S_0$ state. Moreover, the Raman beams can be tuned out of resonance with respect to a possible Raman transition between the $-1/2$ and the $+3/2$ spin states of the $^1S_0$ manifold by using spin state-dependent light shifts (see section 1.1.3).

Orbital Feshbach Resonances

Because of the problems encountered by the tunability of interactions using the lattice depth, it is only natural to think about other possibilities for tuning interactions. Unfortunately, as in all other alkali-earth metals or alkali-earth-like metals ytterbium's ground state $^1S_0$ does not possess an electronic spin, therefore, the well-studied phenomenon of magnetic Feshbach resonances in

alkali atoms cannot be utilized. One possible substitution could be the use of an *optical* Feshbach resonance but this technique suffers from spontaneous emissions and, thus, is associated with high losses [26]. However, recently another type of Feshbach resonance was discovered, the *orbital* Feshbach resonance (OrbFR) [63, 103]. The OrbFR exploits the also just recently observed spin-exchange interaction [21, 118] between ytterbium's $^1S_0$ and $^3P_0$ state. This method requires the clock laser to drive the transition between these states. As a result of the OrbFR the interactions in the system are tunable via a magnetic field as it is the case for magnetic Feshbach resonances.

The OrbFR could be exploited in several ways. Firstly, the OrbFR could be used to investigate the role of interactions in a system with spin-orbit coupling. Secondly, the fractional quantum Hall state could be emulated [7, 30, 54, 109, 124, 129], which is a very promising research topic since the fractional quantum Hall state is not fully understood theoretically and is expected to feature non-Abelian anyonic excitations. The synthetic dimensions approach would be particularly well suited because of the featured long range interactions in the synthetic dimension [30]. Thirdly, the use of an OrbFR enables the implementation of intrinsic attractive interactions, which completes the requirements for the formation of a novel topological superfluid state with Majorana zero modes. According to Ref. [115] such a topological state would form in a one-dimensional Fermi gas with Rashba-like spin-orbit coupling, a Zeeman field and attractive interactions in a harmonic trap. Fourthly, the OrbFR may be used in combination with the tunability of the spin-orbit coupling provided by the clock transition technique for the investigation of an exotic BCS-BEC crossover [120, 135, 136]. Instead of altering the particles' scattering length, in this crossover the scattering length would be set to a certain value, for example a negative value on the BCS side, and then the SOC would be tuned in order to induce the formation of two-body bound-states. Aside from the technical challenges for improving the SOC tunability further, an additional requirement of a truly non-Abelian gauge potential must be met. As mentioned in section 2.1.1 the generated gauge potential already possesses a non-Abelian nature but it would be needed in at least two dimensions in order to show non-Abelian behavior (see Ref. [48]).

Conclusion and Outlook

This thesis presents on the one hand a novel technique for the implementation of spin-orbit coupling and on the other hand groundwork results for the investigation of the role of interactions in fermionic spin-orbit coupled systems made by ultracold atoms.

It was evidenced that the novel technique can be used for the implementation of spin-orbit coupling by observing characteristic double-peak spectra, which are connected to Van Hove singularities, and by a direct measurement of chiral edge currents. The two single phenomenons would not occur in the system of this thesis without spin-orbit coupling. The existence of chiral currents emphasizes the strong connection to non-trivial topological quantum states such as the quantum Hall and the quantum spin Hall state. Furthermore, it was shown that the technique leads to the generation of a synthetic magnetic flux in the "synthetic dimensions" picture, whose unprecedented tunability was demonstrated by a probing of the chiral currents for various flux values. These results could also verify fundamental symmetries, which together with the observation of the higher dressed state's momentum distribution strongly support the correct interpretation and understanding of the observed physics.

In a second series of measurements, two-photon Raman transitions were used for groundwork studies of the role of interactions varied by the depth of the underlying lattice potential. Challenges of the experimental access were discussed, theoretical predictions described and experimental results presented. A discrepancy between theory and experiment was observed together with unexpected short lifetimes. These two issues were discussed, possible explanations were investigated and suggestions for further studies were made. The results provide insight in the dependence of chiral currents on various system parameters, reveal experimental limitations, show first indications of interaction effects and can be used as a solid groundwork for further investigations on many-body effects in spin-orbit coupled systems.

The results of this thesis offer new possibilities for the investigation of topological states of matter with ultracold atomic gases. The synthetic dimensions approach could be used for the investigation of a four-dimensional quantum Hall effect using a synthetic dimension additional to three real dimensions [111] or for a vast amount of different connection possibilities leading to non-trivial topologies [15], when the two available synthetic dimensions are exploited. Two ideas for strongly related subjects to the presented work were discussed. Firstly, it was presented

how periodic boundary conditions in the synthetic dimension could be realized, which could lead to the observation of Hofstadter's butterfly, and, secondly, an alternative scheme for the investigation of interaction effects by the use of the recently discovered orbital Feshbach resonance in ytterbium was presented. The latter could be exploited for the emulation of the fractional quantum Hall state [7, 30, 54, 109, 124, 129], for the formation of a novel topological superfluid state with Majorana zero modes [115] and for the investigation of an exotic BCS-BEC crossover [120, 135, 136], when combined with the tunability of the spin-orbit coupling provided by the clock transition technique.

Acknowledgments

First of all, I would like to express my gratitude to Prof. Klaus Sengstock, Prof. Massimo Inguscio and Prof. Leonardo Fallani for not only giving me the opportunity of but also for supporting me in conducting my master thesis project in Firenze. Thank you very much, Prof. Klaus Sengstock, for all your arrangements.

For fruitful discussions on work related topics and for entertaining and very fascinating discussions on cultural topics I would like to thank Dr. Giacomo Cappellini, Lorenzo Livi, Dr. Marco Mancini and Lorenzo Franchi. Furthermore, I am grateful to all other members of the ytterbium group I met, namely the current members: Prof. Massimo Inguscio, Prof. Leonardo Fallani and Dr. Jacopo Catani and the former members: Dr. Carlo Sias and Dr. Guido Pagano. You all welcomed me remarkably friendly in the lab and on all private occasions. You made me feel included right away.

Grazie mille, Prof. Massimo Inguscio, for welcoming me personally in Firenze and for taking interest in my well-being during my stay.

Thank you very much, Prof. Leonardo Fallani, for accepting me as a member of your group. Thank you for always taking the time to answer my questions and to discuss my ideas. As all other members of the group I benefited a lot from your extraordinary leadership skills.

A presto!

Bibliography

[1] Nobelprize.org. [cited on pages 2, 29, and 31]

[2] M. Aidelsburger, M. Atala, S. Nascimbène, S. Trotzky, Y.-a. Chen, and I. Bloch. Experimental Realization of Strong Effective Magnetic Fields in an Optical Lattice. *Physical Review Letters*, 107(25):1–5, 2011. [cited on page 27]

[3] M. H. Anderson, J. R. Ensher, M. R. Matthews, C. E. Wieman, and E. A. Cornell. Observation of Bose-Einstein Condensation in a Dilute Atomic Vapor. *Science*, 269(5221):198–201, jul 1995. [cited on page 1]

[4] P. W. Anderson. *Basic Notions of Condensed Matter Physics*. Westview Press, 1997. [cited on page 29]

[5] Ennio Arimondo, Donatella Ciampini, André Eckardt, Martin Holthaus, and Oliver Morsch. Kilohertz-Driven Bose–Einstein Condensates in Optical Lattices. In *Advances in Atomic, Molecular and Optical Physics*, volume 61, pages 515–547. 2012. [cited on page 27]

[6] Neil W. Ashcroft and N. David Mermin. *Solid State Physics*. Saunders College, 1976. [cited on pages 11 and 52]

[7] Simone Barbarino, Luca Taddia, Davide Rossini, Rosario Fazio, and Leonardo Mazza. Magnetic crystals and helical liquids in alkaline-earth fermionic gases. *Nat. Commun.*, 6:1–9, 2015. [cited on pages 31, 78, 92, and 94]

[8] Simone Barbarino, Luca Taddia, Davide Rossini, Leonardo Mazza, and Rosario Fazio. Synthetic gauge fields in synthetic dimensions: Interactions and chiral edge modes. *New Journal of Physics*, 18(3):0, 2016. [cited on page 78]

[9] M Bartenstein, A Altmeyer, S Riedl, S Jochim, C Chin, J Hecker Denschlag, and R Grimm. Crossover from a molecular Bose-Einstein condensate to a degenerate Fermi gas. *Physical Review Letters*, 92(12):120401–1, 2004. [cited on page 1]

[10] W. Beugeling, N. Goldman, and C. Morais Smith. Topological phases in a two-dimensional lattice: Magnetic field versus spin-orbit coupling. *Physical Review B - Condensed Matter and Materials Physics*, 86(7):1–18, 2012. [cited on page 28]

[11] Ulf Bissbort, Sören Götze, Yongqiang Li, Jannes Heinze, Jasper S Krauser, Malte Weinberg, Christoph Becker, Klaus Sengstock, and Walter Hofstetter. Detecting the Amplitude Mode of Strongly Interacting Lattice Bosons by Bragg Scattering. *Physical Review Letters*, 106(20):205303, may 2011. [cited on page 1]

[12] E D Black. An introduction to Pound–Drever–Hall laser frequency stabilization. *American Journal of Physics*, 69(1):79, 2001. [cited on pages 40 and 44]

[13] Immanuel Bloch, Jean Dalibard, and Wilhelm Zwerger. Many-body physics with ultracold gases. *Reviews of Modern Physics*, 80(3):885–964, jul 2008. [cited on page 25]

[14] O. Boada, A. Celi, J. I. Latorre, and M. Lewenstein. Quantum simulation of an extra dimension. *Physical Review Letters*, 108(13):2–7, 2012. [cited on page 27]

[15] Octavi Boada, Alessio Celi, Javier Rodriguez-Laguna, José I Latorre, and Maciej Lewenstein. Quantum simulation of non-trivial topology. *New Journal of Physics*, 17(4):45007, 2015. [cited on pages 89 and 93]

[16] T Bourdel, L Khaykovich, J Cubizolles, J Zhang, F Chevy, M Teichmann, L Tarruell, S J J M F Kokkelmans, and C Salomon. Experimental study of the BEC-BCS crossover region in lithium 6. *Physical Review Letters*, 93(5):3–6, 2004. [cited on page 1]

[17] Michele Burrello and Andrea Trombettoni. Non-abelian anyons from degenerate landau levels of ultracold atoms in artificial gauge potentials. *Physical Review Letters*, 105(12), 2010. [cited on page 28]

[18] Yu a Bychkov and E I Rashba. Oscillatory effects and the magnetic susceptibility of carriers in inversion layers. *Journal of Physics C: Solid State Physics*, 17(33):6039–6045, 1984. [cited on page 21]

[19] D Calonico, E K Bertacco, C E Calosso, C Clivati, G A Costanzo, M Frittelli, A Godone, A Mura, N Poli, D V Sutyrin, G Tino, M E Zucco, and F Levi. High-accuracy coherent optical frequency transfer over a doubled 642-km fiber link. *Applied Physics B: Lasers and Optics*, 117(3):979–986, 2014. [cited on page 52]

[20] G K Campbell, M M Boyd, J W Thomsen, M J Martin, S Blatt, M D Swallows, T L Nicholson, T Fortier, C W Oates, S A Diddams, N D Lemke, P Naidon, P Julienne, J Ye, and A D Ludlow. Probing Interactions Between Ultracold Fermions. *Science*, 324(5925):360–363, 2009. [cited on page 71]

[21] G. Cappellini, M. Mancini, G. Pagano, P. Lombardi, L. Livi, M. Siciliani De Cumis, P. Cancio, M. Pizzocaro, D. Calonico, F. Levi, C. Sias, J. Catani, M. Inguscio, and L. Fallani. Direct observation of coherent interorbital spin-exchange dynamics. *Physical Review Letters*, 113(12):1–5, 2014. [cited on pages 10 and 92]

[22] Giacomo Cappellini. *Two-orbital quantum physics in Yb Fermi gases exploiting the 1S0 3P0 clock transition*. PhD thesis, 2015. [cited on pages 33 and 42]

[23] A. Celi, P. Massignan, J. Ruseckas, N. Goldman, I. B. Spielman, G. Juzeliunas, and M. Lewenstein. Synthetic gauge fields in synthetic dimensions. *Physical Review Letters*, 112(4):1–6, 2014. [cited on page 26]

[24] Lawrence W Cheuk, Matthew A Nichols, Melih Okan, Thomas Gersdorf, Vinay V Ramasesh, Waseem S Bakr, Thomas Lompe, and Martin W Zwierlein. Quantum-gas microscope for fermionic atoms. *Physical Review Letters*, 114(19):1–5, 2015. [cited on page 36]

[25] Lawrence W Cheuk, Ariel T Sommer, Zoran Hadzibabic, Tarik Yefsah, Waseem S Bakr, and Martin W Zwierlein. Spin-injection spectroscopy of a spin-orbit coupled Fermi gas. *Physical Review Letters*, 109(9):1–5, 2012. [cited on pages 1 and 49]

[26] Cheng Chin, Rudolf Grimm, Paul Julienne, and Eite Tiesinga. Feshbach resonances in ultracold gases. *Reviews of Modern Physics*, 82(2):1225–1286, apr 2010. [cited on pages 1 and 92]

[27] P. Cladé, C. Ryu, A. Ramanathan, K. Helmerson, and W. Phillips. Observation of a 2D Bose Gas: From Thermal to Quasicondensate to Superfluid. *Physical Review Letters*, 102(17):170401, apr 2009. [cited on page 10]

[28] Cecilia Clivati. *Realization of a phase-coherent optical fiber link for the comparison of remote atomic clocks*. PhD thesis, 2014. [cited on page 43]

[29] Cecilia Clivati, Giacomo Cappellini, Lorenzo F. Livi, Francesco Poggiali, Mario Siciliani de Cumis, Marco Mancini, Guido Pagano, Matteo Frittelli, Alberto Mura, Giovanni A Costanzo, Filippo Levi, Davide Calonico, Leonardo Fallani, Jacopo Catani, and Massimo Inguscio. Measuring absolute frequencies beyond the GPS limit via long-haul optical frequency dissemination. *Optics Express*, 24(11):11865, may 2016. [cited on pages 43 and 52]

[30] Eyal Cornfeld and Eran Sela. Chiral currents in one-dimensional fractional quantum Hall states. *Physical Review B*, 92(11):115446, sep 2015. [cited on pages 2, 31, 92, and 94]

[31] Jean Dalibard, Fabrice Gerbier, Gediminas Juzeliunas, and Patrik Öhberg. Colloquium: Artificial gauge potentials for neutral atoms. *Reviews of Modern Physics*, 83(4):1523–1543, 2011. [cited on pages 2 and 25]

[32] K. B. Davis, M. O. Mewes, M. R. Andrews, N. J. Van Druten, D. S. Durfee, D. M. Kurn, and W. Ketterle. Bose-Einstein condensation in a gas of sodium atoms. *Physical Review Letters*, 75(22):3969–3973, 1995. [cited on page 1]

[33] B. DeMarco and D. S. Jin. Onset of Fermi Degeneracy in a Trapped Atomic Gas. *Science*, 285(5434):1703–1706, 1999. [cited on page 1]

[34] A. Eckardt, Philipp Hauke, P. Soltan-Panahi, C. Becker, K. Sengstock, and Maciej Lewenstein. Frustrated quantum antiferromagnetism with ultracold bosons in a triangular lattice. *EPL (Europhysics Letters)*, 89(1):10010, jan 2010. [cited on page 27]

[35] André Eckardt, Christoph Weiss, and Martin Holthaus. Superfluid-insulator transition in a periodically driven optical lattice. *Physical Review Letters*, 95(26), 2005. [cited on page 27]

[36] Manuel Endres, Takeshi Fukuhara, David Pekker, Marc Cheneau, Peter Schauβ, Christian Gross, Eugene Demler, Stefan Kuhr, and Immanuel Bloch. The 'Higgs' amplitude mode at the two-dimensional superfluid/Mott insulator transition. *Nature*, 487(7408):454–458, jul 2012. [cited on page 1]

[37] Richard P. Feynman. Simulating physics with computers. *International Journal of Theoretical Physics*, 21(6-7):467–488, jun 1982. [cited on page 1]

[38] Matthew P A Fisher, Peter B. Weichman, G. Grinstein, and Daniel S. Fisher. Boson localization and the superfluid-insulator transition. *Physical Review B*, 40(1):546–570, 1989. [cited on page 1]

[39] Lorenzo Franchi. *Control of ultracold fermions with an optical clock transition: spin-orbit coupling and synthetic dimensions*. PhD thesis, 2016. [cited on page 60]

[40] B. Fröhlich, T. Lahaye, B. Kaltenhäuser, H. Kübler, S. Müller, T. Koch, M. Fattori, and T. Pfau. Two-frequency acousto-optic modulator driver to improve the beam pointing stability during intensity ramps. *Review of Scientific Instruments*, 78(4), 2007. [cited on page 40]

[41] Zhengkun Fu, Lianghui Huang, Zengming Meng, Pengjun Wang, Long Zhang, Shizhong Zhang, Hui Zhai, Peng Zhang, and Jing Zhang. Production of Feshbach molecules induced by spin–orbit coupling in Fermi gases. *Nature Physics*, 10(2):110–115, dec 2013. [cited on page 1]

[42] V Galitski and I B Spielman. Spin-orbit coupling in quantum gases. *Nature*, 494(7435):49–54, 2013. [cited on pages 2 and 22]

[43] Fabrice Gerbier and Jean Dalibard. Gauge fields for ultracold atoms in optical superlattices. *New Journal of Physics*, 12, 2010. [cited on pages 23, 25, and 49]

[44] N. Goldman, W. Beugeling, and C. Morais Smith. Topological phase transitions between chiral and helical spin textures in a lattice with spin-orbit coupling and a magnetic field. *EPL (Europhysics Letters)*, 97(2):23003, 2012. [cited on page 28]

[45] N. Goldman, J. C. Budich, and P. Zoller. Topological quantum matter with ultracold gases in optical lattices. *Nature Physics*, 12(7):639–645, 2016. [cited on page 2]

[46] N. Goldman and J. Dalibard. Periodically driven quantum systems: Effective Hamiltonians and engineered gauge fields, 2014. [cited on page 28]

[47] N. Goldman and P. Gaspard. Quantum Hall-like effect for cold atoms in non-Abelian gauge potentials. *Europhysics Letters*, 78:60001, 2007. [cited on page 28]

[48] N Goldman, G Juzeliunas, P Öhberg, and I B Spielman. Light-induced gauge fields for ultracold atoms. *Reports on Progress in Physics*, 77(12):126401, dec 2014. [cited on pages 2, 24, 25, 28, and 92]

[49] A Görlitz, J M Vogels, A E Leanhardt, C Raman, T L Gustavson, J R Abo-Shaeer, A P Chikkatur, S Gupta, S Inouye, T Rosenband, and W Ketterle. Realization of Bose-Einstein Condensates in Lower Dimensions. *Physical Review Letters*, 87(13):130402, sep 2001. [cited on page 1]

[50] Markus Greiner, Immanuel Bloch, Olaf Mandel, Theodor W. Hänsch, and Tilman Esslinger. Exploring Phase Coherence in a 2D Lattice of Bose-Einstein Condensates. *Physical Review Letters*, 87(16):160405, oct 2001. [cited on page 60]

[51] Markus Greiner, Olaf Mandel, Tilman Esslinger, Theodor W. Hänsch, and Immanuel Bloch. Quantum phase transition from a superfluid to a Mott insulator in a gas of ultracold atoms. *Nature*, 415(6867):39–44, 2002. [cited on pages 1 and 80]

[52] Markus Greiner, Cindy A Regal, and Deborah S Jin. Emergence of a molecular Bose–Einstein condensate from a Fermi gas. *Nature*, 426(6966):537–540, 2003. [cited on page 1]

[53] Rudolf Grimm, Matthias Weidemüller, and Yurii B Ovchinnikov. Optical dipole traps for neutral atoms. feb 1999. [cited on page 7]

[54] Fabian Grusdt and Michael Höning. Realization of fractional Chern insulators in the thin-torus limit with ultracold bosons. *Physical Review A*, 90(5):053623, nov 2014. [cited on pages 31, 92, and 94]

[55] T L Gustavson, A P Chikkatur, A E Leanhardt, A. Görlitz, S Gupta, D E Pritchard, and W Ketterle. Transport of Bose-Einstein condensates with optical tweezers. *Physical Review Letters*, 88(2):204011–204014, 2002. [cited on page 36]

[56] F. D M Haldane. Model for a quantum hall effect without landau levels: Condensed-matter realization of the "parity anomaly". *Physical Review Letters*, 61(18):2015–2018, 1988. [cited on pages 28 and 31]

[57] Elmar Haller, James Hudson, Andrew Kelly, Dylan A Cotta, Bruno Peaudecerf, Graham D Bruce, and Stefan Kuhr. Single-atom imaging of fermions in a quantum-gas microscope. *Nature Physics*, 11(9):738–742, jul 2015. [cited on page 36]

[58] T W Hänsch and B Couillaud. Laser frequency stabilization by polarization spectroscopy of a reference cavity. *Optics Communications*, 35(3):441–444, 1980. [cited on pages 36, 38, and 42]

[59] M Z Hasan and C L Kane. Colloquium: Topological insulators. *Reviews of Modern Physics*, 82(4):3045–3067, 2010. [cited on pages 1 and 31]

[60] Andreas Hemmerich. Effective time-independent description of optical lattices with periodic driving. *Physical Review A*, 81(6):063626, jun 2010. [cited on page 27]

[61] J Higbie and D M Stamper-Kurn. Periodically dressed Bose-Einstein condensate: a superfluid with an anisotropic and variable critical velocity. *Physical review letters*, 88(9):090401, 2002. [cited on page 23]

[62] N Hinkley, J A Sherman, N B Phillips, M Schioppo, N D Lemke, K Beloy, M Pizzocaro, C W Oates, and A D Ludlow. An Atomic Clock with 10–18 Instability. *Science*, 341(6151):1215–1218, 2013. [cited on page 19]

[63] M Höfer, L Riegger, F Scazza, C Hofrichter, D R Fernandes, M M Parish, J Levinsen, I Bloch, and S Fölling. Observation of an Orbital Interaction-Induced Feshbach Resonance in Yb 173. *Physical Review Letters*, 115(26), 2015. [cited on page 92]

[64] C. W. Hoyt, Z. W. Barber, C. W. Oates, T. M. Fortier, S. A. Diddams, and L. Hollberg. Observation and absolute frequency measurements of the S01-P03 optical clock transition in neutral ytterbium. *Physical Review Letters*, 95(8), 2005. [cited on page 19]

[65] J. Hubbard. Electron Correlations in Narrow Energy Bands. *Proceedings of the Royal Society A: Mathematical, Physical and Engineering Sciences*, 276(1365):238–257, nov 1963. [cited on page 14]

[66] Massimo Inguscio and Leonardo Fallani. *Atomic Physics: Precise Measurements and Ultracold Matter*. 2013. [cited on page 10]

[67] D Jaksch, C Bruder, J I Cirac, C W Gardiner, and P Zoller. Cold bosonic atoms in optical lattices. *Physical Review Letters*, 81(15):3108–3111, 1998. [cited on page 1]

[68] D. Jaksch and P. Zoller. Creation of effective magnetic fields in optical lattices: The Hofstadter butterfly for cold neutral atoms. *New Journal of Physics*, 5, 2003. [cited on page 25]

[69] Gregor Jotzu, Michael Messer, Rémi Desbuquois, Martin Lebrat, Thomas Uehlinger, Daniel Greif, and Tilman Esslinger. Experimental realization of the topological Haldane model with ultracold fermions. *Nature*, 515(7526):237–240, nov 2014. [cited on page 28]

[70] C L Kane and E J Mele. Quantum Spin Hall Effect in Graphene. *Physical Review Letters*, 95(22):226801, nov 2005. [cited on page 28]

[71] C. L. Kane and E. J. Mele. Z2 topological order and the quantum spin hall effect. *Physical Review Letters*, 95(14), 2005. [cited on page 28]

[72] A. Kastberg, W. D. Phillips, S. L. Rolston, R. J. C. Spreeuw, and P. S. Jessen. Adiabatic Cooling of Cesium to 700 nK in an Optical Lattice. *Physical Review Letters*, 74(9):1542–1545, feb 1995. [cited on page 60]

[73] J Kinast, S L Hemmer, M E Gehm, A Turlapov, and J E Thomas. Evidence for Superfluidity in a Resonantly Interacting Fermi Gas. *Physical Review Letters*, 92(15):150402, apr 2004. [cited on page 1]

[74] Masaaki Kitagawa, Katsunari Enomoto, Kentaro Kasa, Yoshiro Takahashi, Roman Ciuryło, Pascal Naidon, and Paul S. Julienne. Two-color photoassociation spectroscopy of ytterbium atoms and the precise determinations of s -wave scattering lengths. *Physical Review A - Atomic, Molecular, and Optical Physics*, 77(1):1–8, 2008. [cited on page 19]

[75] Takuya Kitagawa, Erez Berg, Mark Rudner, and Eugene Demler. Topological characterization of periodically driven quantum systems. *Physical Review B*, 82(23):235114, dec 2010. [cited on page 28]

[76] K. v. Klitzing, G. Dorda, and M. Pepper. New Method for High-Accuracy Determination of the Fine-Structure Constant Based on Quantized Hall Resistance. *Physical Review Letters*, 45(6):494–497, aug 1980. [cited on page 29]

[77] Michael Köhl, Henning Moritz, Thilo Stöferle, Kenneth Günter, and Tilman Esslinger. Fermionic Atoms in a Three Dimensional Optical Lattice: Observing Fermi Surfaces, Dynamics, and Interactions. *Physical Review Letters*, 94(8):080403, mar 2005. [cited on page 60]

[78] A. R. Kolovsky. Creating artificial magnetic fields for cold atoms by photon-assisted tunneling. *EPL (Europhysics Letters)*, 93(2):20003, jan 2011. [cited on page 27]

[79] Markus König, Hartmut Buhmann, Laurens W. Molenkamp, Taylor Hughes, Chao-Xing Liu, Xiao-Liang Qi, and Shou-Cheng Zhang. The Quantum Spin Hall Effect: Theory and Experiment. *Journal of the Physical Society of Japan*, 77(3):031007, mar 2008. [cited on page 31]

[80] Lev Davidovich Landau and E. M. Lifshitz. *Statistical Physics*. Pergamon Press, Oxford, 1980. [cited on page 29]

[81] R. B. Laughlin. Quantized Hall conductivity in two dimensions, 1981. [cited on page 29]

[82] L J LeBlanc, M. C. Beeler, K. Jiménez-García, A. R. Perry, S. Sugawa, R. A. Williams, and I. B. Spielman. Direct observation of zitterbewegung in a Bose–Einstein condensate. *New Journal of Physics*, 15(7):073011, jul 2013. [cited on page 1]

[83] F. Levi, D. Calonico, A. Mura, M. Frittelli, C.E. Calosso, M. Zucco, C. Clivati, G. A. Costanzo, R. Ambrosini, G. Galzerano, P. De Natale, D. Mazzotti, N. Poli D V Sutyrin, and G. M. Tino. LIFT-the Italian link for time and frequency. In *2013 Joint European Frequency and Time Forum & International Frequency Control Symposium (EFTF/IFC)*, pages 477–480. IEEE, jul 2013. [cited on page 43]

[84] Maciej Lewenstein, Anna Sanpera, Veronica Ahufinger, Bogdan Damski, Aditi Sen(De), and Ujjwal Sen. Ultracold atomic gases in optical lattices: mimicking condensed matter physics and beyond. *Advances in Physics*, 56(2):243–379, mar 2007. [cited on page 25]

[85] Junru Li, Wujie Huang, Boris Shteynas, Sean Burchesky, Furkan Cagri Top, Edward Su, Jeongwon Lee, Alan O. Jamison, and Wolfgang Ketterle. Spin-Orbit Coupling and Spin Textures in Optical Superlattices. *1606.03514*, (1):1–11, 2016. [cited on page 50]

[86] Y-J. Lin, R L Compton, K. Jiménez-García, W D Phillips, J V Porto, and I B Spielman. A synthetic electric force acting on neutral atoms. *Nature Physics*, 7(7):531–534, mar 2011. [cited on page 1]

[87] Y-J Lin, R L Compton, K Jiménez-García, J V Porto, and I B Spielman. Synthetic magnetic fields for ultracold neutral atoms. *Nature*, 462(7273):628–32, 2009.

[88] Y. J. Lin, R. L. Compton, A. R. Perry, W. D. Phillips, J. V. Porto, and I. B. Spielman. Bose-Einstein condensate in a uniform light-induced vector potential. *Physical Review Letters*, 102(13):3–6, 2009. [cited on page 1]

[89] Y.-J. Lin, K. Jiménez-García, and I. B. Spielman. Spin–orbit-coupled Bose–Einstein condensates. *Nature*, 471(7336):83–86, 2011. [cited on pages 1 and 23]

[90] Xiong-Jun Liu, Mario F. Borunda, Xin Liu, and Jairo Sinova. Effect of Induced Spin-Orbit Coupling for Atoms via Laser Fields. *Physical Review Letters*, 102(4):046402, jan 2009. [cited on page 23]

[91] M Mancini, G Pagano, G Cappellini, L Livi, M Rider, J Catani, C Sias, P Zoller, M Inguscio, M Dalmonte, and L Fallani. Observation of chiral edge states with neutral fermions in synthetic Hall ribbons. *Science*, 349(6255):1510–1513, sep 2015. [cited on pages 56, 71, 72, and 91]

[92] Marco Mancini. Realizzazione sperimentale di un gas quantistico degenere di atomi di Itterbio. 2012. [cited on page 38]

[93] Marco Mancini. *Quantum Simulation with Ytterbium Atoms in Synthetic Dimensions*. PhD thesis, 2015. [cited on pages 33, 71, 72, 74, 86, and 91]

[94] Paolo Maraner and Jiannis K. Pachos. Yang-Mills gauge theories from simple fermionic lattice models. *Physics Letters, Section A: General, Atomic and Solid State Physics*, 373(30):2542–2545, 2009. [cited on page 28]

[95] Nicola Marzari, Arash A. Mostofi, Jonathan R. Yates, Ivo Souza, and David Vanderbilt. Maximally localized Wannier functions: Theory and applications. *Reviews of Modern Physics*, 84(4):1419–1475, oct 2012. [cited on page 13]

[96] Hirokazu Miyake, Georgios A. Siviloglou, Colin J. Kennedy, William Cody Burton, and Wolfgang Ketterle. Realizing the Harper Hamiltonian with Laser-Assisted Tunneling in Optical Lattices. *Physical Review Letters*, 111(18):185302, oct 2013. [cited on page 27]

[97] Joel E Moore. The birth of topological insulators. *Nature*, 464(7286):194–8, 2010. [cited on page 31]

[98] Erich J. Mueller. Artificial electromagnetism for neutral atoms: Escher staircase and Laughlin liquids. *Physical Review A - Atomic, Molecular, and Optical Physics*, 70(4), 2004. [cited on page 25]

[99] Chetan Nayak, Steven H Simon, Ady Stern, Michael Freedman, and Sankar Das Sarma. Non-Abelian anyons and topological quantum computation. *Reviews of Modern Physics*, 80(3):1083–1159, sep 2008. [cited on pages 2 and 29]

[100] T. News Staff. BREAKTHROUGH OF THE YEAR: The Runners-Up. *Science*, 318(5858):1844a–1849a, dec 2007. [cited on page 31]

[101] G. Nienhuis, P. van der Straten, and S-Q. Shang. Operator description of laser cooling below the Doppler limit. *Physical Review A*, 44(1):462–474, jul 1991. [cited on page 6]

[102] K. Osterloh, M. Baig, L. Santos, P. Zoller, and M. Lewenstein. Cold atoms in non-abelian gauge potentials: From the hofstadter "moth" to lattice gauge theory. *Physical Review Letters*, 95(1), 2005. [cited on pages 25 and 28]

[103] G. Pagano, M. Mancini, G. Cappellini, L. Livi, C. Sias, J. Catani, M. Inguscio, and L. Fallani. Strongly Interacting Gas of Two-Electron Fermions at an Orbital Feshbach Resonance. *Physical Review Letters*, 115(26):1–5, 2015. [cited on page 92]

[104] Guido Pagano. *Raffreddamento e Intrappolamento di atomi di Itterbio*. PhD thesis, 2011. [cited on page 38]

[105] Guido Pagano. *Many-body physics with Ytterbium Fermi gases in optical lattices: from one-dimensional systems to orbital magnetism*. PhD thesis, 2015. [cited on pages 33, 34, 35, 36, and 47]

[106] Guido Pagano, Marco Mancini, Giacomo Cappellini, Pietro Lombardi, Florian Schäfer, Hui Hu, Xia-ji Liu, Jacopo Catani, Carlo Sias, Massimo Inguscio, and Leonardo Fallani. A one-dimensional liquid of fermions with tunable spin. *Nature Physics*, 10(3):198–201, feb 2014. [cited on page 10]

[107] R. Peierls. Zur Theorie des Diamagnetismus von Leitungselektronen. *Zeitschrift f??r Physik*, 80(11-12):763–791, 1933. [cited on page 25]

[108] Ekkehard Peik, Tobias Schneider, and Christian Tamm. Laser frequency stabilization to a single ion. *Journal of Physics B: Atomic, Molecular and Optical Physics*, 39(1):145–158, jan 2006. [cited on pages 36 and 43]

[109] Alexandru Petrescu and Karyn Le Hur. Chiral Mott insulators, Meissner effect, and Laughlin states in quantum ladders. *Physical Review B*, 91(5):054520, feb 2015. [cited on pages 31, 92, and 94]

[110] Sergey G. Porsev and Andrei Derevianko. Hyperfine quenching of the metastable3P0,2 states in divalent atoms. *Physical Review A - Atomic, Molecular, and Optical Physics*, 69(4):042506–1, 2004. [cited on page 23]

[111] H. M. Price, O. Zilberberg, T. Ozawa, I. Carusotto, and N. Goldman. Four-Dimensional Quantum Hall Effect with Ultracold Atoms. *Physical Review Letters*, 115(19):1–6, 2015. [cited on pages 89 and 93]

[112] Xiao-liang Qi and Shou-cheng Zhang. The quantum spin Hall effect and topological insulators. *Physics Today*, 63(1):33–38, jan 2010. [cited on page 31]

[113] Xiao Liang Qi and Shou Cheng Zhang. Topological insulators and superconductors. *Reviews of Modern Physics*, 83(4), 2011. [cited on pages 1 and 30]

[114] Chunlei Qu, Chris Hamner, Ming Gong, Chuanwei Zhang, and Peter Engels. Observation of Zitterbewegung in a spin-orbit-coupled Bose-Einstein condensate. *Physical Review A*, 88(2):021604, aug 2013. [cited on page 1]

[115] Jonathan Ruhman, Erez Berg, and Ehud Altman. Topological States in a One-Dimensional Fermi Gas with Attractive Interaction. *Physical Review Letters*, 114(10):100401, mar 2015. [cited on pages 2, 92, and 94]

[116] Janne Ruostekoski, Gerald V Dunne, and Juha Javanainen. Particle Number Fractionalization of an Atomic Fermi-Dirac Gas in an Optical Lattice. *Physical Review Letters*, 88(18):180401, 2002. [cited on page 25]

[117] Indubala I. Satija, Daniel C. Dakin, J. Y. Vaishnav, and Charles W. Clark. Physics of a two-dimensional electron gas with cold atoms in non-Abelian gauge potentials. *Physical Review A - Atomic, Molecular, and Optical Physics*, 77(4), 2008. [cited on page 28]

[118] F Scazza, C Hofrichter, M Höfer, P. C. De Groot, I. Bloch, and S. Fölling. Observation of two-orbital spin-exchange interactions with ultracold SU(N)-symmetric fermions. *Nature Physics*, 10(10):779–784, 2014. [cited on page 92]

[119] Stefan Schmid, Gregor Thalhammer, Klaus Winkler, Florian Lang, and Johannes Hecker Denschlag. Long distance transport of ultracold atoms using a 1D optical lattice. *New Journal of Physics*, 8, 2006. [cited on page 36]

[120] Vijay B Shenoy and Jayantha P Vyasanakere. Fermions in synthetic non-Abelian gauge potentials: rashbon condensates to novel Hamiltonians. *Journal of Physics B: Atomic, Molecular and Optical Physics*, 46(13):134009, jul 2013. [cited on pages 2, 92, and 94]

[121] Jacob F Sherson, Christof Weitenberg, Manuel Endres, Marc Cheneau, Immanuel Bloch, and Stefan Kuhr. Single-atom-resolved fluorescence imaging of an atomic Mott insulator. *Nature*, 467(7311):68–72, 2010. [cited on page 36]

[122] Daniel Adam Steck. Quantum and Atom Optics Textbook. *Book*, page 932, 2007. [cited on pages 5, 6, 8, 9, 14, and 23]

[123] Simon Stellmer, Rudolf Grimm, and Florian Schreck. Production of quantum-degenerate strontium gases. *Physical Review A - Atomic, Molecular, and Optical Physics*, 87(1):1–16, 2013. [cited on page 46]

[124] Marcello Calvanese Strinati, Eyal Cornfeld, Davide Rossini, Simone Barbarino, Marcello Dalmonte, Rosario Fazio, Eran Sela, and Leonardo Mazza. Laughlin-like states in bosonic and fermionic atomic synthetic ladders. *arXiv preprint*, pages 1–16, 2016. [cited on pages 31, 92, and 94]

[125] J. Struck, C. Ölschläger, M. Weinberg, P. Hauke, J. Simonet, A. Eckardt, M. Lewenstein, K. Sengstock, and P. Windpassinger. Tunable Gauge Potential for Neutral and Spinless Particles in Driven Optical Lattices. *Physical Review Letters*, 108(22):225304, may 2012. [cited on page 27]

[126] J Struck, J Simonet, and K Sengstock. Spin-orbit coupling in periodically driven optical lattices. *Physical Review A*, 90(3):31601, sep 2014. [cited on page 50]

[127] J. Struck, M. Weinberg, C. Ölschläger, P. Windpassinger, J. Simonet, K. Sengstock, R. Höppner, P. Hauke, a. Eckardt, M. Lewenstein, and L. Mathey. Engineering Ising-XY spin-models in a triangular lattice using tunable artificial gauge fields. *Nature Physics*, 9(September):738–743, 2013. [cited on pages 10 and 27]

[128] Julian Struck, C. Olschlager, R. Le Targat, Parvis Soltan-Panahi, André Eckardt, Maciej Lewenstein, Patrick Windpassinger, and Klaus Sengstock. Quantum Simulation of Frustrated Classical Magnetism in Triangular Optical Lattices. *Science*, 333(6045):996–999, aug 2011. [cited on page 27]

[129] Luca Taddia, Eyal Cornfeld, Davide Rossini, Leonardo Mazza, Eran Sela, and Rosario Fazio. Topological fractional pumping with alkaline-earth(-like) ultracold atoms. *arXiv preprint*, pages 1–10, jul 2016. [cited on pages 31, 92, and 94]

[130] Shintaro Taie, Yosuke Takasu, Seiji Sugawa, Rekishu Yamazaki, Takuya Tsujimoto, Ryo Murakami, and Yoshiro Takahashi. Realization of a SU(2)??SU(6) system of fermions in a cold atomic gas. *Physical Review Letters*, 105(19):1–4, 2010. [cited on page 46]

[131] Leticia Tarruell, Daniel Greif, Thomas Uehlinger, Gregor Jotzu, and Tilman Esslinger. Creating, moving and merging Dirac points with a Fermi gas in a tunable honeycomb lattice. *Nature*, 483(7389):302–305, 2012. [cited on page 10]

[132] D. Thouless, M. Kohmoto, M. Nightingale, and M. den Nijs. Quantized Hall Conductance in a Two-Dimensional Periodic Potential, 1982. [cited on page 29]

[133] David J. Thouless. *Topological quantum numbers in nonrelativistic physics*. World Scientific, 1998. [cited on page 29]

[134] M. A H Vozmediano, M. I. Katsnelson, and F. Guinea. Gauge fields in graphene, 2010. [cited on page 28]

[135] Jayantha P. Vyasanakere and Vijay B. Shenoy. Bound states of two spin-12 fermions in a synthetic non-Abelian gauge field. *Physical Review B - Condensed Matter and Materials Physics*, 83(9), 2011. [cited on pages 2, 92, and 94]

[136] Jayantha P. Vyasanakere, Shizhong Zhang, and Vijay B. Shenoy. BCS-BEC crossover induced by a synthetic non-Abelian gauge field. *Physical Review B - Condensed Matter and Materials Physics*, 84(1):1–11, 2011. [cited on pages 2, 92, and 94]

[137] Michael L. Wall, Andrew P. Koller, Shuming Li, Xibo Zhang, Nigel R. Cooper, Jun Ye, and Ana Maria Rey. Synthetic Spin-Orbit Coupling in an Optical Lattice Clock. *Physical Review Letters*, 116(3):1–6, 2016. [cited on pages 49 and 54]

[138] Pengjun Wang, Zeng-Qiang Yu, Zhengkun Fu, Jiao Miao, Lianghui Huang, Shijie Chai, Hui Zhai, and Jing Zhang. Spin-Orbit Coupled Degenerate Fermi Gases. *Physical Review Letters*, 109(9):095301, aug 2012. [cited on page 1]

[139] Frank Wilczek and A. Zee. Appearance of Gauge Structure in Simple Dynamical Systems. *Physical Review Letters*, 52(24):2111–2114, jun 1984. [cited on page 1]

[140] Atsushi Yamaguchi. *Metastable State of Ultracold and Quantum Degenerate Ytterbium Atoms: High-Resolution Spectroscopy and Cold Collisions*. PhD thesis, 2008. [cited on page 18]

[141] Hui Zhai. Spin-Orbit Coupled Quantum Gases. *International Journal of Modern Physics B*, 26(01):1230001, 2012. [cited on pages 2 and 24]

[142] Hui Zhai. Degenerate quantum gases with spin–orbit coupling: a review. *Reports on Progress in Physics*, 78(2):026001, feb 2015. [cited on page 2]

[143] Jin-Yi Zhang, Si-Cong Ji, Zhu Chen, Long Zhang, Zhi-Dong Du, Bo Yan, Ge-Sheng Pan, Bo Zhao, You-Jin Deng, Hui Zhai, Shuai Chen, and Jian-Wei Pan. Collective Dipole Oscillations of a Spin-Orbit Coupled Bose-Einstein Condensate. *Physical Review Letters*, 109(11):115301, sep 2012. [cited on page 1]

[144] Long Zhang, Jin-Yi Zhang, Si-Cong Ji, Zhi-Dong Du, Hui Zhai, Youjin Deng, Shuai Chen, Peng Zhang, and Jian-Wei Pan. Stability of excited dressed states with spin-orbit coupling. *Physical Review A*, 87(1):011601, jan 2013. [cited on page 1]

[145] S C Zhang. The Chern-Simons-Landau-Ginzburg Theory Of The Fractional Quantum Hall-Effect. *International Journal of Modern Physics B*, 6(1):25–58, 1992. [cited on page 29]

[146] M W Zwierlein, C A Stan, C H Schunck, S M F Raupach, A J Kerman, and W Ketterle. Condensation of pairs of fermionic atoms near a Feshbach resonance. *Physical Review Letters*, 92(12):120403–1, 2004. [cited on page 1]